Doctoral Dissertation

博士論文

Studies on organelle dynamics during spermiogenesis in *Marchantia polymorpha*

（ゼニゴケ精子変態過程におけるオルガネラ動態の研究）

A Dissertation Submitted for the Degree of Doctor of Philosophy
December 2020

令和 2 年 12 月博士（理学）申請

Department of Biological Sciences, Graduate School of Science,
The University of Tokyo

東京大学大学院理学系研究科

生物科学専攻

Takuya Norizuki

法月　拓也

TABLE OF CONTENTS

ABSTRACT

Sexual reproduction is a fundamental event in many eukaryotes, whose processes have been diversified during evolution. In land plants, while male gametes of angiosperms and some gymnosperms are immotile and delivered to female gametes through pollen tubes, other plants utilize motile flagellated male gametes called spermatozoids. During spermiogenesis, a process of transformation from immotile spermatids to motile spermatozoids, dynamic and complex reorganization of organelles take place. Although this process has been intensively examined by transmission electron microscopy, organelle dynamics during spermiogenesis and molecular mechanisms of spermiogenesis remain obscure. To understand how each organelle is reorganized during spermiogenesis, I took advantage of the liverwort *Marchantia polymorpha*, because genetic and cell biological techniques are applicable to this model plant that produce spermatozoids. Firstly, I generated transgenic plants expressing fluorescent protein-tagged organelle markers and observed reorganization of each organelle by confocal microscopy. I found that the shape and number of each organelle change drastically during spermiogenesis, and each of organelles and organelle proteins are deformed and/or removed at different stages during spermiogenesis. I also found through detailed observation of mitochondria that mitochondrial fission frequently occurs at an early stage of spermiogenesis and most of resultant mitochondria are removed. Furthermore, I found that the posterior mitochondrion is generated by fission of the anterior mitochondrion. I then attempted to reveal how cytoplasmic components is removed during spermiogenesis, especially focusing on autophagy, a system for degradation of cytoplasmic components in the vacuole, because autophagic activity is highly elevated during spermiogenesis in *M. polymorpha*. Reverse genetic analyses using autophagy-defective mutants demonstrated

that autophagy is responsible for degradation of various organelles during spermiogenesis. I also found that mitochondria are selectively degraded by autophagy at an early stage of spermiogenesis and later autophagic degradation of the cytosol and other organelles such as peroxisomes take place. I further found that some organelle proteins are degraded in the vacuole in an autophagy-independent manner. These results indicated that each cytoplasmic component is degraded in the vacuole in a distinctive and cell-autonomous manner during spermiogenesis in *M. polymorpha*, different from metazoan spermiogenesis in which unnecessary cytoplasmic components are removed by the phagocytic activity of neighboring cells.

ACKNOWLEDMENTS

I appreciate the feedback for this thesis offered by Dr. Yamato Yoshida, Dr. Hisayoshi Nozaki, and Dr. Naoki Irie (The University of Tokyo). I thank Dr. Takayuki Kohchi and Dr. Ryuichi Nishihama (Kyoto University), Dr. Shin-ichi Arimura (The University of Tokyo), Dr. Shoji Mano, Dr. Kazuo Ebine, Dr. Takehiko Kanazawa, and Dr. Naoki Minamino (National Institute for Basic Biology) for kindly sharing materials. I thank Model Plant Research Facility (National Institute for Basic Biology) for provision and maintenance of the spaces for cultivating the plants. I thank Dr. Hirokazu Tsukaya (The University of Tokyo) for valuable suggestions and instructions. I appreciate the help from all members in division of Cellular Dynamics (National Institute for Basic Biology). I especially thank Dr. Takashi Ueda, Dr. Takehiko Kanazawa, and Dr. Naoki Minamino (National Institute for Basic Biology) for their supports and insightful discussion throughout my study.

ABBRIVIATIONS

AM: anterior mitochondrion

ATG: autophagy-related

BSA: bovine serum albumin

CDS: coding sequence

CRISPR: clustered regularly interspaced short palindromic repeat

DAPI: 4′,6-diamidino-2-phenylindole

DIC: differential interference contrast

DMSO: dimethyl sulfoxide

dsDNA: double stranded DNA

ER: endoplasmic reticulum

ESCRT: endosomal sorting complex required for transport

GOMED: Golgi membrane-associated degradation

gRNA: guide RNA

HA: human influenza hemagglutinin

HPT: hygromycin phosphotransferase

mCitrine: monomeric Citrine

mGFP: monomeric green fluorescent protein

MLS: multi-layered structure

mRFP: monomeric red fluorescent protein

mTurquoise2: monomeric Turquoise2

PAM: protospacer adjacent motif

PCR: polymerase chain reaction

PFA: paraformaldehyde

PGM: phosphoglucomutase

PI3K: phosphatidylinositol 3-kinase

PI3P: phosphatidylinositol 3-phosphate

PM: posterior mitochondrion

PO: propylene oxide

SNARE: soluble *N*-ethylmaleimide-sensitive factor attachment protein receptor

ST: sialyltransferase

SP: signal peptide

T-DNA: transfer DNA

TEM: transmission electron microscopy

UTR: untranslated region

WT: wild type/wild-type

GENERAL INTRODUCTION

Sexual reproduction is a widely observed style of reproduction, in which haploid gametes fuse with each other to generate diploid zygotes. In most multicellular organisms, two gametes are different in size and shape, and many of them utilize oogamy, in which smaller male gametes (sperm) are motile and larger female gametes (egg) are immotile. Sperms exhibit dramatic divergence in the morphology, motility, and organelle composition, which is believed to reflect adaptation to their specific fertilization environments (Pitnick et al. 2009). In the lineage of Viridiplantae, oogamy has been independently evolved from the metazoan lineage (Mori et al. 2015). As a result, sperms in Viridiplantae possess distinct features from metazoan spermatozoa. In land plants, male gametes in angiosperms and some gymnosperms are immotile without flagella, and delivered to the egg via pollen tubes during fertilization. On the other hand, bryophytes, lycophytes, monilophytes, and some gymnosperms such as Ginkgo utilize motile male gametes, called spermatozoids, with two or more flagella during sexual reproduction. Spermatogenesis in most land plants utilizing spermatozoids includes several steps: proliferation of spermatogenous cells through repetitive mitosis, which is followed by mitosis of spermatid mother cells to produce spermatids, and spermiogenesis in which immotile spermatids are transformed into motile spermatozoids. During spermiogenesis dynamic and complex reorganization of intracellular components including organelles takes place (reviewed by Renzaglia and Garbary [2001]). Although this process has been intensively observed by transmission electron microscopy (TEM), detailed information on reorganization of various organelles during spermiogenesis and its molecular mechanisms remain limited, partly because of lack of appropriate tools for analyzing organelle reorganization.

In this study, I used the liverwort *Marchantia polymorpha* as a model to study organelle remodeling during spermiogenesis, because the genetic and cell biological techniques have been well developed for this plant (Ishizaki et al. 2016). *M. polymorpha* is a dioecious species having male and female organs on different thalli and propagates through asexual and sexual reproduction (**Figure 1A**). In sexual reproduction, antheridia are produced on the antheridiophore of male thalli. In an antheridium, spermatogenous cells repeatedly divide to form numerous spermatid mother cells. Two spermatids are generated by the diagonal cell division of a spermatid mother cell, which differentiate into spermatozoids via spermiogenesis (Shimamura 2016; **Figure 1B**). During spermiogenesis, reorganization of various intracellular components takes place: *de novo* synthesis of the locomotory apparatus, chromatin condensation, nuclear shaping, decrease in the number of mitochondria, and removal of a major part of cytoplasmic components from spermatids. Mature spermatozoids possess two flagella, a helical nucleus, two mitochondria and a plastid, and little amount of the cytoplasm remains in their cell body. Spermatozoids move in water to the egg in the archegonium to accomplish fertilization (Shimamura 2016; **Figure 1**).

I tried to reveal how dynamic and complex reorganization of various organelles during spermiogenesis in *M. polymorpha*. In **Chapter 1**, I observed processes of organelle reorganization during spermiogenesis, such as dynamic changes in the shape and number of organelles by confocal microscopy in transgenic plants expressing various organelle markers. I found that the shape and number of various organelles drastically change during spermiogenesis, with removal of most organelles and the cytosol from spermatids. I also found through detailed observation of mitochondria that mitochondrial fission takes place to generate two mitochondria in mature spermatozoids. In **Chapter 2**, I attempted

to reveal how each organelle is removed during spermiogenesis, especially focusing on autophagy, a system for degradation of cytoplasmic components in the vacuole, because autophagy is suggested to be highly activated during spermiogenesis by previous TEM observation. I discovered that autophagy is required for degradation of various cytoplasmic components. Intriguingly, mitochondrial degradation by autophagy precedes autophagic degradation of other cytoplasmic components such as peroxisomes and the cytosol during spermiogenesis. Furthermore, I found that some organelle markers are transported into the vacuole in an autophagy-independent manner. These finding demonstrate that each cytoplasmic component is degraded in the vacuole in a distinct and cell-autonomous manner during spermiogenesis in *M. polymorpha*, different from the metazoan system, in which cytoplasmic components are removed by the phagocytic activity of neighboring cells.

FIGURE

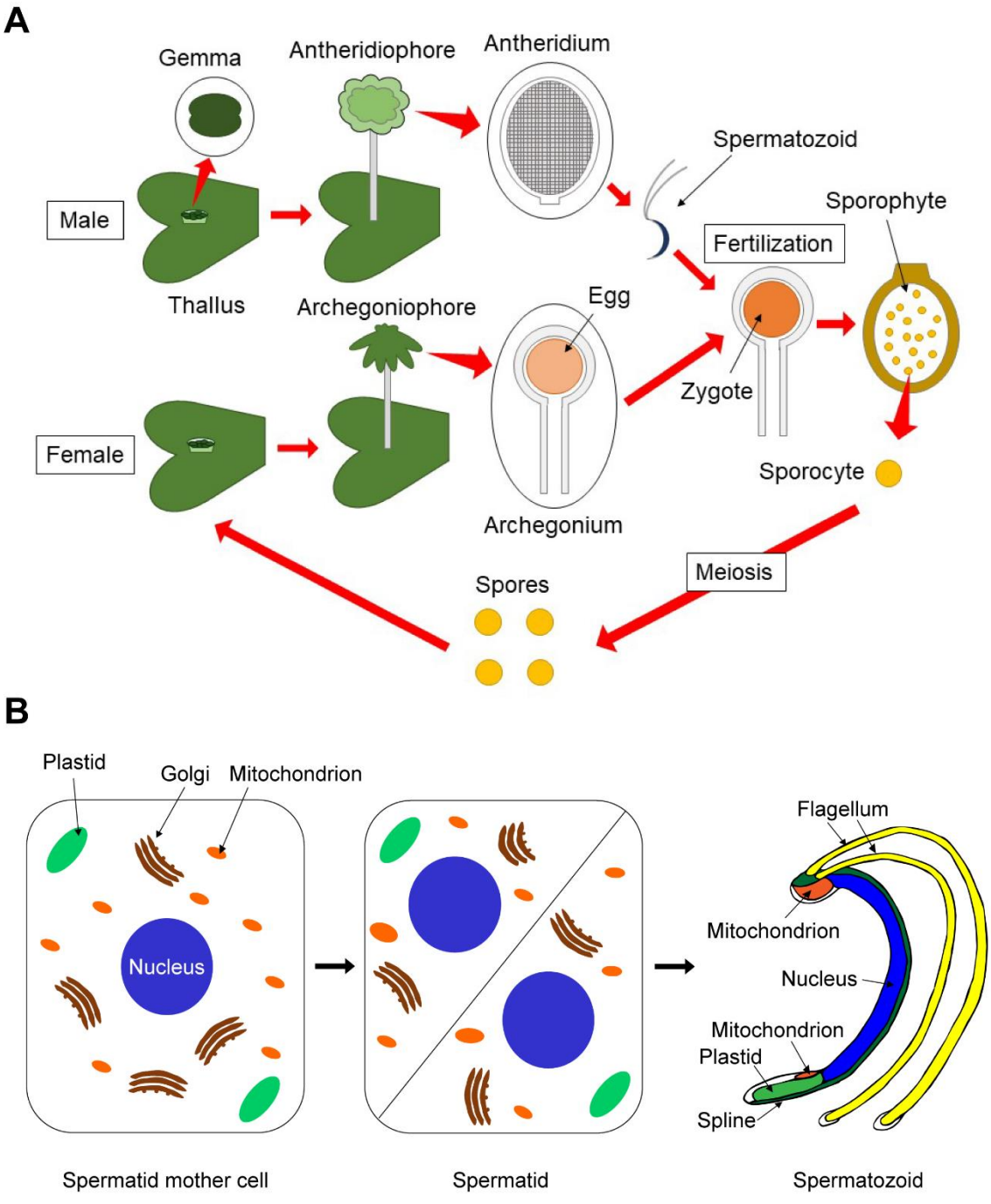

Figure 1. Life cycle of *M. polymorpha*

(**A**) Life cycle of *M. polymorpha*. In asexual reproduction, thalli can reproduce through

the production of gemmae. In sexual reproduction, antheridia and archegonia are produced on the antheridiophore of the male thallus and on the archegoniophore of the female thallus, respectively. Each antheridium produces numerous spermatozoids, and spermatozoids reach the egg in the archegonium to fertilize it. After fertilization, the zygote develops into the sporophyte in the archegonium. The sporocyte undergoes meiosis to produce four spores, and numerous spores are discharged from the sporophyte. Spores germinate and develop into thalli. (**B**) Schematic models of spermatogenesis. A spermatid mother cell undergoes diagonal cell division to generate two immotile spermatids, which differentiate into motile spermatozoids via spermiogenesis. The images are illustrated based on figures in Shimamura (2016).

MATELIALS AND METHODS

Identification of ATG genes in M. polymorpha

Amino acid sequences of Mp*ATG* genes were obtained from *M. polymorpha* genome version 5.1 (Montgomery et al. 2020) in MarpolBase (http://marchantia.info/) using *ATG* genes of *Arabidopsis thaliana* as queries (Li et al. 2014; Shemi et al. 2015; Liu et al. 2018). For *ATG29* and *ATG31*, whose homologs have not been identified in *A. thaliana* thus far, *ATG* genes in *Saccharomyces cerevisiae* were used as queries. A domain search was performed using SMART (http://smart.embl-heidelberg.de/) (Letunic et al. 2015; Letunic and Bork 2018). I followed the nomenclature by Bowman et al. (2016) for names of genes, proteins, and mutants of *M. polymorpha*.

Vector Construction

The coding sequence (CDS) and genomic sequence of genes in *M. polymorpha* were amplified by polymerase chain reaction (PCR) from cDNA or genomic DNA prepared from thalli of the *M. polymorpha* accession Takaragaike-1 (Tak-1, male) (Ishizaki et al. 2008). The primer sequences used in this study are listed in **Table 1**.

For the construction of pENTR *Mito*, cDNA for amino-terminal 64 amino acids of the gamma subunit of F1ATPase in *M. polymorpha* (Mp7g04400.1) was amplified and subcloned into pENTR/D-TOPO (Thermo Fisher Scientific, Waltham, Massachusetts, USA) according to the manufacturer's instructions.

For the construction of pENTR $_{pro}$Mp*SYP2*:*Mito*, the 5′ sequence [promoter + 5′ untranslated region (UTR)] of Mp*SYP2* (Kanazawa et al. 2016) was inserted into the *Not*I site of pENTR *Mito* using the In-Fusion HD Cloning System (Clontech, Shiga, Japan).

For the construction of pENTR Mp*PGM1*, the CDS for Mp*PGM1* (Mp4g13750.1) was

amplified and subcloned into pENTR/D-TOPO.

For the construction of pENTR Mp*PGM1-mTurquoise2* (*monomeric Turquoise2*), the CDS for *mTurquoise2* was inserted into the *Asc*I site of pENTR Mp*PGM1* vector using the In-Fusion HD Cloning System.

For the construction of pENTR *SP* (*signal peptide*)-*mTurquoise2-HDEL*, DNA fragment including pENTR backbone, SP, and HDEL sequence was amplified from pENTR *SP-mRFP* (*monomeric red fluorescent protein*)-*HDEL* (Kanazawa et al. 2020). This fragment was fused with the CDS for *mTurquoise2* using the In-Fusion HD Cloning System to generate pENTR *SP-mTurquoise2-HDEL*.

For the construction of pENTR *mTurquoise2*-Mp*SEC20*, pENTR *mTurquoise2*-Mp*SEC22*, pENTR *mTurquoise2*-Mp*GOS11*, and pENTR *mTurquoise2*-Mp*SFT1*, the CDS for *mTurquoise2* was inserted into the *Not*I site of pENTR Mp*SEC20*, pENTR Mp*SEC22*, pENTR Mp*GOS11*, and pENTR Mp*SFT1* (Kanazawa et al. 2016) using the In-Fusion HD Cloning System.

For the construction of pENTR:*ST* (*sialyltransferase*)-*mTurquoise2*, the sequence for the transmembrane domain of rat ST was amplified from pENTR *ST-Venus* (Kanazawa et al. 2016) and subcloned into pENTR/D-TOPO. The CDS for *mTurquoise2* was inserted into the *Asc*I site of pENTR *ST* using the In-Fusion HD Cloning System.

For the construction of pENTR *mTurquoise2-PTS1*, pENTR backbone and the CDS for *mTurquoise2* containing the PTS1 sequence (Mano et al. 1999) at the 5′ end were amplified using pENTR and the CDS for *mTurquoise2*, respectively, and were fused using the In-Fusion HD Cloning System.

For the construction of pENTR *mRFP*- or *mTurquoise2*-Mp*DRP3l*$^{WT\text{ or }K75A}$, I introduced a point mutation (75th Lys to Ala) by PCR using pENTR Mp*DRP3l* (Nagaoka et al. 2017)

to generate pENTR Mp*DRP3l*^{K75A}. The CDS for *mRFP* or *mTurquoise2* was inserted into the *Not*I site of pENTR Mp*DRP3l*$^{WT\text{ or }K75A}$ using the In-Fusion HD Cloning System.

For the construction of pENTR $_{pro}$Mp*DRP3*:*3×HA*-Mp*DRP3l*, the 3.4 kb 5′ sequence (promoter + 5′ UTR) of Mp*DRP3* was amplified by PCR and was inserted into the *Not*I site of pENTR *3×HA* (*human influenza hemagglutinin*) (Minamino et al. unpublished) using the In-Fusion HD Cloning System (pENTR $_{pro}$Mp*DRP3*:*3×HA*). The CDS for Mp*DRP3l* was amplified from pENTR Mp*DRP3l* (Nagaoka et al. 2017) and inserted into the *Asc*I site of pENTR $_{pro}$Mp*DRP3*:*3×HA* using the In-Fusion HD Cloning System.

For the construction of pENTR $_{pro}$Mp*ATG8a*:*mCitrine* (*monomeric Citrine*)-Mp*ATG8a*, genomic sequences of Mp*ATG8a* (Mp1g21590.1) comprising the protein-coding regions and 3′ flanking sequences (2.0 kb) were amplified with the *Sma*I site followed by a flexible linker sequence (Gly–Gly–Ser–Gly) attached at the 5′ end and subcloned into the pENTR vector. Then, cDNA for *mCitrine* containing the *Sma*I site at the 5′ end was inserted into the *Sma*I site of pENTR vectors containing Mp*ATG8a* using the In-Fusion HD Cloning System. The 5.0 kb 5′ sequence (promoter + 5′ UTR) of Mp*ATG8a* was then amplified and inserted into the *Sma*I site of pENTR *mCitrine*-Mp*ATG8a*.

For the construction of pENTR $_{pro}$Mp*ATG8a*:*HA*-Mp*ATG8a*, *HA*-Mp*ATG8a* was amplified from the $_{pro}$Mp*ATG8a*:*mCitrine*-Mp*ATG8a* vector and subcloned into pENTR/D-TOPO. The 5.0 kb 5′ sequence (promoter + 5′ UTR) of Mp*ATG8a* was then amplified from the $_{pro}$Mp*ATG8a*:*mCitrine*-Mp*ATG8a* vector and inserted into the *Not*I site of pENTR *HA*-Mp*ATG8a* using the In-Fusion HD Cloning System.

For the construction of pENTR $_{pro}$Mp*ATG5*:Mp*ATG5*^{res}, the CDS for Mp*ATG5* was amplified and subcloned into pENTR/D-TOPO. A point mutation (AGACCT to AGGCCA in ^{111}Lys-^{112}Pro) was introduced into pENTR Mp*ATG5* by PCR. The 5.0 kb 5′

sequence (promoter + 5′ UTR) of Mp*ATG5* was amplified and inserted into the *Not*I site of this vector using the In-Fusion HD Cloning System.

For the construction of pENTR $_{pro}$Mp*ATG5*:Mp*ATG5-mCitrine*, the CDS for *mCitrine* was amplified and inserted into the *Asc*I site of pENTR Mp*ATG5* using the In-Fusion HD Cloning System. The 5.0 kb 5′ sequence (promoter + 5′ UTR) of Mp*ATG5* was amplified and inserted into the *Not*I site of this vector using the In-Fusion HD Cloning System.

For the construction of the clustered regularly interspaced short palindromic repeats (CRISPRs)-associated endonuclease Cas9 (CRISPR/Cas9) vector, two complementary oligonucleotides in the sequences of Mp*ATG5*, Mp*ATG2*, Mp*ATG7*, Mp*ATG13*, and Mp*ATG14* were synthesized and annealed, and the resulting double-stranded fragments were subcloned at the *Bsa*I site of the pMpGE_En03 vector (Sugano et al. 2018) using the DNA ligation kit Ver.2.1 (Takara Bio, Shiga, Japan) according to the manufacturer's instructions.

For the construction of pMpGWB101 $_{pro}$Mp*MS1*, a promoter sequence with 5.1 kb 5′ sequence (promoter + 5′ UTR) of Mp*MS1* (Mp3g17000.1) was introduced at the *Hin*dIII site of pMpGWB101 (Ishizaki et al. 2015) using the In-Fusion HD Cloning System.

The sequences flanked by the *att*L1 and *att*L2 sites in the resultant entry vectors were introduced into the destination vectors using the Gateway LR Clonase™ II Enzyme Mix (Thermo Fisher Scientific) according to the manufacturer's instructions, as listed in **Table 2**.

The $_{pro}$Mp*EF1α*:*SP-mCitrine-HDEL* vector (Mano et al. unpublished), the $_{pro}$Mp*EF1α*:*Citrine-PTS1* vector (Mano et al. 2018), the pMpGWB301 $_{pro}$Mp*VAMP71*:*mCitrine*-Mp*VAMP71* vector (Minamino et al. 2017) vector and the pMpGWB101 $_{pro}$Mp*VAMP71*:*mGFP* (*monomeric green fluorescent protein*)-

Mp*VAMP71* vector (Kanazawa et al. unpublished) were also used in this study.

Plant materials and transformation

The *M. polymorpha* accessions Tak-1 (male) and Tak-2 (female) were grown asexually on 1/2× Gamborg's B5 medium containing 1.4% (w/v) agar at 22 °C under continuous white light. For induction of sexual reproduction, two-week-old thalli grown on 1/2× Gamborg's B5 medium containing 1.4% agar at 22 °C under continuous white light were further cultivated on vermiculite soaked in 1:1000 Hyponex (HYPONeX JAPAN, Osaka, Japan) at 22 °C under continuous white light for two weeks, and mature thalli were cultivated at 22 °C under continuous white light supplemented with far-red light. For crossing male and female lines, spermatozoids were obtained by placing a mature antheridiophore upside-down on a drop of 20-30 μL water for one minute, and then applied to archegoniophores. Archegoniophores with yellow sporangia were obtained three to five weeks after crossing.

Transformation of *M. polymorpha* was performed as previously described (Kubota et al. 2013). Two-week-old thalli, whose apical parts including meristems were removed, were grown on 1/2× Gamborg's B5 medium containing 1.0% (w/v) sucrose and 1.4% (w/v) agar at 22 °C under continuous white light for four days for regeneration of the thalli. The regenerating plantlets were co-cultivated with the agrobacterium strain GV2260 harboring the binary vector in the liquid 0M51C medium containing 2% (w/v) sucrose and 100 μM 3′,5′-dimethoxy-4′-hydroxyacetophenone (Sigma-Aldrich, St. Louis, Missouri, USA) at 22 °C under continuous white light for four days. Transformants were selected on plates containing 10 mg/L hygromycin B and 250 mg/L cefotaxime for the pMpGWB101, pMpGWB103, and pMpGE010 vectors and 0.5 μM chlorsulfuron and 250

mg/L cefotaxime for the pMpGWB301 and pMpGWB308 vectors, the $_{pro}$Mp*EF1α*:*SP-mCitrine-HDEL* vector, and the $_{pro}$Mp*EF1α*:*Citrine-PTS1* vector.

Genotyping

For genotyping of mutants generated by the CRISPR/Cas9 system, total RNA was extracted from 5-day-old thalli of the wild type and Mp*atg* mutants using the RNeasy Plant Mini Kit (Qiagen, Venlo, Netherlands) and used as a template for reverse transcription using SuperScript III Reverse Transcriptase (Thermo Fisher Scientific) and the oligo (dT) (18-mer) primer according to the manufacturer's instructions. Mutations in the obtained cDNA fragments were analyzed by direct sequencing.

Before genotyping of F1 progenies, F1 progenies were grown on 1/2× Gamborg's B5 medium containing 10 mg/L hygromycin and 250 mg/L cefotaxime or 0.5 μM chlorsulfuron and 250 mg/L cefotaxime, and I isolated the F1 progenies harboring neither the hygromycin- nor chlorsulfuron-resistant genes. For the genotyping of these lines, genomic DNA was extracted from the thalli in the genotyping buffer containing 1 M KCl, 100 mM Tris-HCl (pH 9.5), and 10 mM EDTA. This DNA was used as templates for PCR using KOD FX Neo (TOYOBO, Osaka, Japan) according to the manufacturer's instructions. Sex determination was performed by PCR using the primers listed in **Table 1**. Mutations in the obtained genomic DNA fragments were analyzed by direct sequencing.

Cell wall digestion of antheridial cells

Cell wall digestion was carried out according to Shimamura (2015). Antheridia were fixed with 4% (w/v) paraformaldehyde (PFA) in PME buffer [50 mM piperazine-1,4-bis(2-ethanesulfonic acid), 5 mM ethylene glycol bis(2-aminoethyl ether)-*N*,*N*,*N′*,*N′*-tetraacetic

acid, and 1 mM $MgSO_4$, adjusted at pH 6.8 using NaOH] for 60 minutes, and then washed with PME buffer three times. The fixed antheridia were incubated in the wall-digesting enzyme solution [1% (w/v) Cellulase Onozuka RS (SERVA, Heidelberg, Germany), 0.25% (w/v) Pectolyase Y-23 (Kyowa Chemical Products, Osaka, Japan), 1% (w/v) BSA (bovine serum albumin), 0.1% (w/v) IGEPAL CA-630, and 1× cOmplete™ protease inhibitor cocktail (Roche, Basel, Switzerland), and 1% (w/v) glucose in PME buffer] for 30 minutes, and then washed with PME buffer three times. The cell wall-digested antheridia were placed on MAS-coated glass slides (Matsunami Glass, Osaka, Japan), and a coverslip was placed on the sample squashing the sample gently with a finger. The coverslip was removed, and the sample was incubated in 1:1000 Hoechst 33342 solution (Dojindo Laboratories, Kumamoto, Japan), 1:1000 SYBR™ Green I Nucleic Acid Gel Stain (Thermo Fisher Scientific) or 1 μg/mL DAPI (4′,6-diamidino-2-phenylindole) in PME buffer for at least 10 minutes.

Immunofluorescence of antheridial cells

Cell wall digestion was performed as described above. After the incubation with the wall-digesting enzyme solution, the sample was incubated in the permeabilization buffer [1% (w/v) BSA and 0.1% (v/v) Triton X-100 in PME buffer] for 10 minutes, and then washed with PME buffer three times. The cell wall-digested antheridia were placed on MAS-coated glass slides and a coverslip was placed on the sample squashing the sample gently with a finger. After the coverslip was removed, the sample was incubated in 1% (w/v) BSA in PBS buffer [150 mM NaCl, 80 mM Na_2HPO_4, and 40 mM NaH_2PO_4 (adjusted at pH 6.8 using NaOH)] for 30 minutes, then incubated in primary antibody solution [1:200 for the anti-HA antibody (M180-3; Medical & Biological Laboratories, Aichi, Japan),

1:1000 for the anti-α-Tubulin antibody (DM1A; Sigma-Aldrich), or 1:200 for the anti-double stranded DNA (dsDNA) antibody (HYB331-01; Santa Cruz Biotechnology, Dallas, Texas, USA) in PBS buffer containing 1% (w/v) BSA] overnight at 4 °C. The sample was washed with PBS buffer three times and incubated in secondary antibody solution [1:1000 for Alexa Fluor™ 546 goat anti-mouse IgG (H+L) (Thermo Fisher Scientific) for the anti-HA and anti-dsDNA antibody, 1:1000 for Alexa Fluor™ 488 goat anti-mouse IgG (H+L) (Thermo Fisher Scientific) for the anti-α-Tubulin antibody, and 1:1000 for Goat anti-Mouse IgG (H+L) Alexa Fluor™ Plus 488 (Thermo Fisher Scientific) for the anti-dsDNA antibody in PBS buffer containing 1% (w/v) BSA] for at least one hour at 37 °C. The sample was washed with PBS buffer three times, and incubated in 1:1000 Hoechst in PBS buffer for at least 10 minutes. The sample was mounted with ProLong™ Diamond Antifade Mountant (Thermo Fisher Scientific) and incubated for at least 24 hours at room temperature in the dark.

Confocal laser scanning microscopy

For the observation of the mitochondria, plastids, and MpATG8a, five-day-old thalli expressing each marker were observed. For the induction by estradiol, four-day-old thalli expressing mRFP-MpDRP3l were incubated in 1/2× Gamborg's B5 medium containing 5 μM β-estradiol or 1:4000 DMSO (dimethyl sulfoxide) at 22 °C for 24 hours under continuous light. For the observation of MpATG8a in the vacuole, four-day-old thalli expressing mCitrine-MpATG8a were incubated in 1/2× Gamborg's B5 medium containing 1 μM Concanamycin A (Santa Cruz Biotechnology) or 1:1000 DMSO at 22 °C for 14 hours under continuous light. For the observation of organelle markers in antheridial cells, antheridial cells whose cell wall was digested as described above or

antheridia hand-sectioned manually by a razor blade were used. For the observation of spermatozoids, spermatozoids were obtained as described above and fixed in 4% (w/v) PFA in PBS buffer for five minutes. Fixed spermatozoids were centrifuged at 10,000 rpm for one minute and the pellet was suspended in PBS buffer with/without 1:1000 Hoechst.

LSM780 confocal microscope (Carl Zeiss, Oberkochen, Germany) equipped with an oil immersion lens (×63, numerical aperture = 1.4) was used for confocal microscopy. Diode 405-30, Argon 488, and DPSS 561-10 lasers were used for excision of the samples at 405 nm, 488 nm, and 561 nm, respectively. Spectral unmixing was performed using the ZEN2012 software (Carl Zeiss). Image processing was performed using the ZEN2012 software and ImageJ (National Institute of Health, Bethesda, Maryland, USA).

For the measurement of the mitochondrial size, the area of Mito-Citrine in Z-projection images was measured by using Image J. As a threshold to make binary, the algorithm Moments in Image J was used.

Dark field microscopy

To trace movement of spermatozoids, spermatozoids collected as described above were observed with a dark-field microscope (Olympus, Tokyo, Japan) equipped with an ORCA-Flash4.0 V2 camera (Hamamatsu photonics, Shizuoka, Japan). For the trajectories of spermatozoids, 33 frames with 33 millisecond steps were modified by ImageJ macro, Color Footprint Rainbow (http://www.jaist.ac.jp/ms/labs/hiratsuka/images/0/09/Color_FootPrint.txt).

Electron microscopy

Wild-type and Mp*atg5-1*^{ge} antheridia were used for electron microscopy observation. Sample preparation was performed according to Minamino et al. (2017). The antheridia were fixed with 2% (w/v) PFA and 2% (v/v) glutaraldehyde in 0.05 M cacodylate buffer (pH 7.4) at 4 °C overnight. The fixed samples were washed three times with 0.05 M cacodylate buffer for 30 minutes each and were then post-fixed with 2% (w/v) osmium tetroxide in 0.05 M cacodylate buffer at 4 °C for three hours. The samples were dehydrated in graded ethanol solutions [50 and 70% (v/v) ethanol for 30 minutes each at 4 °C, 90% (v/v) for 30 minutes at room temperature, four times with 100% for 30 minutes each at room temperature, and 100% overnight at room temperature]. The samples were infiltrated with propylene oxide (PO) two times for 30 minutes each, and then placed into a 70:30 mixture of PO and resin (Quetol-651; Nisshin EM, Tokyo, Japan) for one hour. The caps of tubes were opened overnight to volatilize PO. The samples were transferred to fresh 100% resin and polymerized at 60 °C for 48 hours. Ultra-thin sample sections were mounted on copper grids, stained with 2% (w/v) uranyl acetate and lead stain solution (Sigma-Aldrich) and observed with a transmission electron microscope (JEM-1400Plus; JEOL, Tokyo, Japan) at an acceleration voltage of 80 kV. Digital images (3296 × 2472 pixels) were taken with a CCD camera (EM-14830RUBY2; JEOL).

Immunoblot analysis

For the immunoblot analysis, gemma were grown on 1/2× Gamborg's B5 agar medium with cellophane for five days. 50 mg or 100 mg of plants were homogenized in 100 µL or 200 µL of grinding buffer [50 mM HEPES–KOH (pH 7.5), 340 mM sorbitol, 5 mM $MgCl_2$, and 1× cOmplete^{TM} Protease Inhibitor Cocktail] for each genotype and centrifuged at 1,000× g for 10 min, respectively. The supernatants were centrifuged at

3,000× g for 10 minutes, and the resulting supernatants were used for immunoblotting. The polyclonal anti-GFP antibody (Kanazawa et al. 2016) was purified by affinity column chromatography using the GST-mCitrine protein bound to the HiTrapTM NHS-activated HP Column (GE Healthcare, Chicago, Illinois, USA) and used at 500-1000× dilution. The peroxidase-conjugated donkey anti-rabbit immunoglobulin antibody (GE Healthcare) was used as the secondary antibody. Signals were detected using Immobilon^{TM} Western Chemiluminescent HRP Substrate (Merck Millipore, Billerica, Massachusetts, USA).

Measurement of chlorophyll content

Five-day-old thalli were incubated in 1 mL of liquid 1/2× Gamborg's B5 medium for five days under continuous light or in 0.05% (w/v) MES buffer (pH 5.5) for five days under dark condition, and chlorophyll was extracted by soaking in 500 µl *N*,*N*-dimethylformamide overnight. Calculation of chlorophyll concentrations was done according to Porra et al. (1989). Three thalli were treated as one sample for correct measurement of fresh weights.

Statistics

Statistical differences were analyzed by Tukey's test or Welch's t test in R. Measurements were significant when $p < 0.05$.

TABLES

Table 1. The primer list

	Primer 1 (5′->3')	Primer 2 (5′->3')
pENTR *Mito*	CACCATGGCTTCCGGAAGTGCACG	GGACTTCACAGATTTCATCCTATTTCTC
pENTR Mp*PGM1*	CACCATGGCGTTCTCCGCAGCA	CGTAATTACTGTTGGCTTGGTTCG
mTurquoise2 (*Asc*I)	AAGGGTGGGCGCGGGGTGTCTAAGGGTGAGGAACTCTTC	AGCTGGGTCGGCGCGCTATTTGTAAAGCTCATCCATTCCGAG
pENTR backbone-SP-HDEL	GATCTTGGTGGAGGCCATCAT	GGCCGAGGATAATGATAGGAGAAG
mTurquoise2 (pENTR *SP-mTurquoise2-HDEL*)	TCATTATCCTCGGCCGTGTCTAAGGGTGAGGAACTCTTC	GCCTCCACCAAGATCTTTGTAAAGCTCATCCATTCCGAGG
pENTR *ST*	CACCATGATTCATACCAACTTGAAGAAAAAGTTC	CATGGCCACTTTCTCCTGGC
mTurquoise2 (*Not*I)	GCAGGCTCCGCGGCCATGGTGTCTAAGGGTGAGGAACT	GAAGGGGGCGGCCGCTTTGTAAAGCTCATCCATTCCGAGG
pENTR (backbone)	AAGGGTGGGCGCGCCGACC	GGTGAAGGGGGCGGCCG
mTurquoise2-PTS1 (pENTR)	GCCGCCCCCTTCACCATGGTGTCTAAGGGTGAGGAACT	GGCGCGCCCACCCTTTCATAGCTTCGAAACTTTGTAAAGCTCATCCATTCCGAGG
pENTR Mp*DRP3I*^{K75A}	AGTGGGGCGTCGAGTGTCCTGGAAGCTATGGTGGG	ACTCGACGCCCCACTGCTCTGGCTACCAACGACG
$_{pro}$Mp*MS1*	GGCCAGTGCCAAGCTTGATGAAGGGAAACAAGATGTGTCA	TTTGTACAAACTTGTTTTGAGAGATATCTCTGAACCTCGAAC
mRFP (*Not*I)	GCAGGCTCCGCGGCCATGGCCTCCTCCGAGGAC	GTGAAGGGGGCGGCCGCGGCGCCGGTGGAGTGGCG
pENTR Mp*ATG8a*	CACCCCCGGGGGCAGCGGCATGACGGGGAAGAGGAGTTCGTTCA	CTGACAAAGTATCAGTCGTAGGCTCATGG
mCitrine (*Sma*I)	GCCCCCTTCACCCCCGGGATGGTGAGCAAGGGCGAGG	CATGCCGCTGCCCCCCTTGTACAGCTCGTCCATGCC
$_{pro}$Mp*ATG8a* (*mCitrine*-Mp*ATG8a*)	GCCCCCTTCACCCCCAGGTCTAGTAATCGCTCACTTAGGG	CTTGCTCACCATCCCCTTGCCGCTGCTACTACTTTCTTCT
pENTR *HA*-Mp*ATG8a*	CACCATGTATCCATACGATGTTCCTGACTATGCTGGGGGCAGCGGCACGGGGAAGAGGAGTTCGT	CACCATGGAGCAAAAGTTGATTTCTGAAGAAGATCTTGGGGGCAGCGGCACGGGGAAGAGGAGTTCGT
$_{pro}$Mp*ATG8a* (*HA*-Mp*ATG8a*)	GCAGGCTCCGCGGCCAGGTCTAGTAATCGCTCACTTAGGG	GTGAAGGGGGCGGCCCTTGCCGCTGCTACTACTTTCTTCT
pENTR Mp*ATG5*	CACCATGGGGAATGAAGATGAAGATGGA	TCTAGAAACCCATGTACATATGCAAAG
Mp*ATG5*^{res}	TGCTGTGTGCAGAACCGGAGAGGCCATGGAACT	GTTCTGCACACAGCAAGTCGAAAAGGACGCCTGTG

mCitrine (*Asc*I)	AAGGGTGGGCGCGCCATGGTGAGCAAGGGCGAGGAG	AGCTGGGTCGGCGCGTTACTTGTACAGCTCGTCCATGC
Mp*ATG5* guide sequence	CTCGGTGCAGAACCGGAGAGACCT	AAACAGGTCTCTCCGGTTCTGCAC
Mp*ATG2* guide sequence	CTCGGAGTCCATCAACTCAGGGTG	AAACCACCCTGAGTTGATGGACTC
Mp*ATG7* guide sequence	CTCGTACAAAGTGTCTTCTTTTAG	AAACCTAAAAGAAGACACTTTGTA
Mp*ATG13* guide sequence	CTCGGTGGAGGGGTAGGGGGTCCA	AAACTGGACCCCCTACCCCTCCAC
Mp*ATG14* guide sequence (Mp*atg14-1*^{ge})	CTCGGCAGCAGGCTGCACAGACAG	AAACCTGTCTGTGCAGCCTGCTGC
Mp*ATG14* guide sequence (Mp*atg14-2*^{ge})	CTCGGGAAGCACGCTCCAAAGCGT	AAACACGCTTTGGAGCGTGCTTCC
Rbm27 (Male)	CCAAGTGCGGGCAGAATCAAGT	TTCATCGCCCGCTATCACCTTC
Rhf73 (Female)	TGACGACGAAGATGTGGATGAC	GAAACTTGGCCGTGTGACTGA

Table 2. Vectors used in LR reactions

Expression vector	Entry vector	Ref.	Destination vector	Ref.
*pro*Mp*EF1α*:*Mito-Citrine*	pENTR *Mito*	1	pMpGWB308	2
*pro*Mp*SYP2*:*Mito-Citrine*	pENTR *pro*Mp*SYP2*:*Mito*	1	pMpGWB307	2
*pro*Mp*EF1α*:Mp*PGM1-Citrine*	pENTR Mp*PGM1*	1	pMpGWB308	2
*pro*Mp*EF1α*:Mp*PGM1-mTurquoise2*	pENTR Mp*PGM1-mTurquoise2*	1	pMpGWB103	2
*pro*Mp*EF1α*:*SP-mTurquoise2-HDEL*	pENTR *SP-mTurquoise2-HDEL*	1	pMpGWB103	2
*pro*Mp*DUO1*:*mCitrine-*Mp*SEC20*	pENTR Mp*SEC20*	3	pMpGWB301 *pro*Mp*DUO1*:*mCitrine**	4
*pro*Mp*DUO1*:*mCitrine-*Mp*SEC22*	pENTR Mp*SEC22*	3	pMpGWB301 *pro*Mp*DUO1*:*mCitrine**	4
*pro*Mp*DUO1*:*mTurquoise2-*Mp*SEC20*	pENTR *mTurquoise2-*Mp*SEC20*	1	pMpGWB101 *pro*Mp*DUO1***	4
*pro*Mp*DUO1*:*mTurquoise2-*Mp*SEC22*	pENTR *mTurquoise2-*Mp*SEC22*	1	pMpGWB101 *pro*Mp*DUO1***	4
*pro*Mp*DUO1*:*ST-Venus*	pENTR *ST-Venus*	3	pMpGWB301 *pro*Mp*DUO1***	4
*pro*Mp*DUO1*:*mCitrine-*Mp*GOS11*	pENTR Mp*GOS11*	3	pMpGWB301 *pro*Mp*DUO1*:*mCitrine**	4
*pro*Mp*DUO1*:*mCitrine-*Mp*SFT1*	pENTR Mp*SFT1*	3	pMpGWB301 *pro*Mp*DUO1*:*mCitrine**	4
*pro*Mp*DUO1*:*ST-mTurquoise2*	pENTR *ST-mTurquoise2*	1	pMpGWB101 *pro*Mp*DUO1***	4

$_{pro}$Mp*DUO1*: *mTurquoise2*-Mp*GOS11*	pENTR *mTurquoise2*-Mp*GOS11*	1	pMpGWB101 $_{pro}$Mp*DUO1***	4
$_{pro}$Mp*DUO1*: *mTurquoise2*-Mp*SFT1*	pENTR *mTurquoise2*-Mp*SFT1*	1	pMpGWB101 $_{pro}$Mp*DUO1***	4
mRFP-Mp*DRP3l*^{WT} (Estradiol-induction vector)	pENTR *mRFP*-Mp*DRP3l*^{WT}	1	pMpGWB168	5
mRFP-Mp*DRP3l*^{K75A} (Estradiol-induction vector)	pENTR *mRFP*-Mp*DRP3l*^{K75A}	1	pMpGWB168	5
$_{pro}$Mp*DUO1*: *mTurquoise2*-Mp*DRP3l*^{WT}	pENTR *mTurquoise2*-Mp*DRP3l*^{WT}	1	pMpGWB101 $_{pro}$Mp*DUO1***	4
$_{pro}$Mp*DUO1*: *mTurquoise2*-Mp*DRP3l*^{K75A}	pENTR *mTurquoise2*-Mp*DRP3l*^{K75A}	1	pMpGWB101 $_{pro}$Mp*DUO1***	4
$_{pro}$Mp*MS1*: *mTurquoise2*-Mp*DRP3l*^{WT}	pENTR *mTurquoise2*-Mp*DRP3l*^{WT}	1	pMpGWB101 $_{pro}$Mp*MS1*	1
$_{pro}$Mp*MS1*: *mTurquoise2*-Mp*DRP3l*^{K75A}	pENTR *mTurquoise2*-Mp*DRP3l*^{K75A}	1	pMpGWB101 $_{pro}$Mp*MS1*	1
$_{pro}$Mp*DRP3*:*3×HA*-Mp*DRP3l*	pENTR $_{pro}$Mp*DRP3*:*3×HA*-Mp*DRP3l*	1	pMpGWB101	2
$_{pro}$MpA*TG8a*:*mCitrine*-Mp*ATG8a*	pENTR $_{pro}$Mp*ATG8a*: *mCitrine*-Mp*ATG8a*	1	pMpGWB301	2
$_{pro}$Mp*ATG8a*:*HA*-Mp*ATG8a*	pENTR $_{pro}$Mp*ATG8a*:*HA*-Mp*ATG8a*	1	pMpGWB101	2
$_{pro}$Mp*ATG5*: Mp*ATG5*^{res}	pENTR $_{pro}$Mp*ATG5*: Mp*ATG5*^{res}	1	pMpGWB301	2

Mp*ATG5* CRISPR vector	pMpGE_En03 Mp*ATG5* guide sequence	1	pMpGE010	6
Mp*ATG2* CRISPR vector	pMpGE_En03 Mp*ATG2* guide sequence	1	pMpGE010	6
Mp*ATG7* CRISPR vector	pMpGE_En03 Mp*ATG7* guide sequence	1	pMpGE010	6
Mp*ATG13* CRISPR vector	pMpGE_En03 Mp*ATG13* guide sequence	1	pMpGE010	6
Mp*ATG14* CRISPR vector (Mp*atg14-1*^{ge})	pMpGE_En03 Mp*ATG14* guide sequence (Mp*atg14-1*^{ge})	1	pMpGE010	6
Mp*ATG14* CRISPR vector (Mp*atg14-2*$^{ge)}$	pMpGE_En03 Mp*ATG14* guide sequence (Mp*atg14-2*^{ge})	1	pMpGE010	6

*The pMpGWB301/101 vector containing the promoter sequence of Mp*DUO1* and the cDNA for *mCitrine*

**The pMpGWB301/101 vector containing the promoter sequence of Mp*DUO1*

1: this study, 2: Ishizaki et al. 2015, 3: Kanazawa et al. 2016, 4: Minamino et al. unpublished, 5: Nishihama et al. unpublished, 6: Sugano et al. 2018.

CHAPTER 1: Organelle dynamics during spermiogenesis in *Marchantia polymorpha*

INTRODUCTION

Spermiogenesis is a complicated developmental event in which dynamic and complex reorganization of organelles takes place. With the implementation of electron microscopy on a wide range of plants, major morphogenetic processes, which occurs during plant spermiogenesis, have been observed (Renzaglia and Garbary 2001). Despite the intensive TEM observation, however, it remains largely unknown how organelle reorganization during spermiogenesis occurs. This is in part because of a lack of appropriate tools and methods to observe organelle dynamics during spermiogenesis.

Fluorescent protein-tagged organelle markers are useful tools for observation of organelle dynamics during developmental events in plants such as embryogenesis and meiosis in *A. thaliana* (Brownfield et al. 2015; Kimata et al. 2019; Kimata et al. 2020). In *M. polymorpha*, various organelle markers have been developed (Kanazawa et al. 2016; Mano et al. 2018). Whereas Minamino et al. (2017) examined dynamics of some organelles during spermiogenesis using these markers, it remains largely unknown when each organelle is reorganized during spermiogenesis, because the stage of spermiogenesis has not been firmly defined for plant spermiogenesis.

In this study, I observed organelle dynamics along developmental stages characterized by Minamino *et al*. (unpublished). In this classification, the nuclear shape is used as the primary stage mark. For visualizing the nuclear shape, cell wall of antheridial cells was digested, because the antheridia are composed of numerous piled cells and it is difficult to detect morphology of the nucleus and other organelles without separating cells from each other (Minamino et al. unpuplished). Spermiogenesis in *M. polymorpha* is divided into six stages (Stage 0 to 5). At Stage 0, antheridial cells are non-flagellated and possess a spherical nucleus, including not only non-flagellated spermatids but also spermatid

mother cells or spermatogenous cells (these cells are not distinguishable after the cell wall digestion). At Stage 1, cells are flagellated whereas they possess a spherical nucleus. At Stage 2, the nucleus starts to elongate to exhibit an ellipsoidal shape, and flagellar elongation is mostly completed. At Stage 3, the elongating nucleus is observed in a crescent shape. At Stage 4, the nucleus is elongated to be cylindrical, whereas the spermatid at this stage still retains abundant cytoplasm. Mature spermatozoids are defined as Stage 5, in which the highly elongated helical nucleus and little amount of the cytoplasm are observed (Minamino et al. unpublished; **Figure 2**).

I performed observation of various organelles at each stage along spermiogenesis, which demonstrated that the shape and number of each organelle drastically change during spermiogenesis. Furthermore, I found that each organelle and/or organelle protein are removed at a different stage of spermiogenesis. I also found that MpDRP3-mediated fission of the anterior mitochondrion yields the posterior mitochondrion. These results highlight dynamic, complex, and highly organized remodeling of each organelle during spermiogenesis in *M. polymorpha*.

RESULTS

Observation of reorganization of various organelles during spermiogenesis

For observation of reorganization of various organelles during spermiogenesis, I developed transgenic plants expressing various organelle markers (**Table 3**).

At first, I observed mitochondria. I used the fluorescent protein Citrine with the mitochondria-targeted sequence (Mito-Citrine) as a mitochondria marker. As a mitochondria-targeted sequence, amino-terminal 64 amino acids of the gamma subunit of F1ATPase in *M. polymorpha* were used. Mito-Citrine was shown to colocalize with subcellular compartments labeled by MitoTracker (Nagaoka et al. 2017), indicating that this protein is targeted to mitochondria (**Figure 3A**). Using this marker, I observed reorganization of mitochondria during spermiogenesis (**Figure 4**). At Stage 0, two populations of cells were observed; a population of cells possessed many small spherical mitochondria, the other population possessed highly elongated mitochondria surrounding the nucleus with a round shape. At Stage 1, mitochondria were largely fragmented, but one rod-shaped mitochondrion is observed at the base of flagella (arrowhead in **Figure 4**). Since the anterior mitochondrion, which is associated with the multi-layered structure (MLS) beneath the basal bodies, starts to be formed when flagella start to be formed (Kreitner 1977a), this rod-shaped mitochondrion should be the precursor of the anterior mitochondrion. During Stage 1 and 2, the total area of mitochondria was decreased, and only one mitochondrion was remained at Stage 3. At Stage 4 and 5, two mitochondria, namely the anterior and posterior mitochondria, were observed in each cell body of spermatids and spermatozoids (**Figure 4**). Thus, the number and size of mitochondria drastically change during spermiogenesis in *M. polymorpha*.

Next, I observed plastids. In this study, I used the fluorescent protein-tagged MpPGM1

as a plastid marker. *PGM* genes encode phosphoglucomutase (PGM) and plastidal PGM (AtPGM1) is shown to be required for starch synthesis in the plastid in *A. thaliana* (Caspar et al. 1985; Periappuram et al. 2000). In thallus cells, MpPGM1-Citrine was localized in chloroplasts overlapping with autofluorescence from chlorophyll, indicating that MpPGM1-Citrine can be used as a plastid marker in *M. polymorpha* (**Figure 3B**). I then observed reorganization of plastids during spermiogenesis using this marker (**Figure 5**). At Stage 0, the tentaculate plastid was observed, which was consistent with the previous TEM observation of another liverwort *Blasia pusilla* (Renzaglia and Duckett, 1987). During spermiogenesis, a plastid changed to a spherical configuration until Stage 3. At Stage 4, the plastid became flattened, and spermatozoids possessed one elongated plastid at their posterior region (**Figure 5**). These results indicated that the morphology of the plastid also drastically changes during spermiogenesis.

Next, I observed the endoplasmic reticulum (ER) using Citrine fused with the signal peptide (SP) required for translocation to the ER lumen at its amino terminus and four amino acids (His-Asp-Glu-Leu) sufficient for ER localization of Citrine at its carboxyl terminus (SP-mCitrine-HDEL; Mano et al. 2018; **Figure 6A**). At Stage 0 and 1, the signal from this ER marker was detected at the nuclear envelop and the peripheral ER, similar to reported pattern in thallus cells (Mano et al. 2018). However, at Stage 2, the signal from this marker at the nuclear envelop was markedly decreased, and the signal at the nuclear envelop was hardly detected at Stage 3, whereas the cytoplasmic signal was still observed at this stage. Intriguingly, at Stage 5, this ER marker was detected at the anterior and posterior regions of spermatozoids (**Figure 6A**). SP-mCitrine-HDEL is a soluble protein, and I also monitored ER dynamics using a fluorescently tagged membrane protein, mCitrine-MpSEC20, which is the ER-localized SNARE (soluble *N*-

ethylmaleimide-sensitive factor attachment protein receptor) protein (Kanazawa et al. 2016; **Figure 6B**). Although the signal at the nuclear envelop was detected until Stage 2, at Stage 3 to 5, this signal disappeared. Unlike SP-mCitrine-HDEL, the signal from mCitrine-MpSEC20 was hardly detected in the cytoplasm of the cell bodies of spermatids or spermatozoids at Stage 3 to 5 (**Figure 6B**). There have been no reports regarding the ER structure in bryophyte spermatozoids as long as I know (Renzaglia and Garbary 2001), and it is not clear whether spermatozoids of *M. polymorpha* is completely devoid of the ER. However, considering these results together with my observation that the nuclear envelop undergoes dynamic reorganization during spermiogenesis, the ER is drastically reorganized and probably largely removed during spermiogenesis.

Next, I observed the Golgi apparatus using Venus fused with the transmembrane domain of rat sialyltransferase (ST) (Kanazawa et al. 2016; **Figure 7A**). At Stage 0, many small puncta were observed in the cytoplasm, similar to the pattern reported in thallus cells of *M. polymorpha* (Kanazawa et al. 2016). Intriguingly, at Stage 1 and 2, one large Golgi apparatus was observed in the cytoplasm, which would be consistent with the previous report from TEM observation of another liverwort *B. pusilla* that the enlarged Golgi apparatus is observed in the cytosol during spermiogenesis (Renzaglia and Duckett, 1987). A similar enlarged Golgi structure was also observed using other Golgi markers mCitrine-MpGOS11 and mCitrine-MpSFT1, which are Golgi-localized SNARE proteins (Kanazawa et al. 2016; **Figure 7B**). At Stage 3, merely faint signal from ST-Venus was detected, and signal was not detected in spermatozoids (Stage 5) (**Figure 7A**). These results suggested that Golgi proteins/structures are removed from spermatids around Stage 3.

Finally, I observed peroxisomes using Citrine fused with the peroxisome-targeting

sequence which is ten amino acids derived from pumpkin hydroxypyruvate reductase (Mano et al. 1999; Mano et al. 2018; **Figure 8**). Several peroxisomes were observed in the cytoplasm until Stage 4, however, the signal from this marker was hardly detected in spermatozoids (**Figure 8**). These results suggested that peroxisomes are removed from spermatids after Stage 4.

Mitochondria undergo frequent fission in the early stage of spermiogenesis

Mitochondria are a highly dynamic organelle undergoing frequent fission and fusion (Arimura 2018; Giacomello et al. 2020). Since fragmentated mitochondria were observed during spermiogenesis (**Figure 4**), I investigated whether mitochondrial fission occurs in reorganization of mitochondria during spermiogenesis. In land plants including *M. polymorpha*, dynamin-related protein DRP3 is reported to accumulate at fission sites of mitochondria, which is required for mitochondrial fission (Arimura and Tsutsumi 2002; Fujimoto et al. 2009; Nagaoka et al. 2017). Thus, I examined localization of 3×HA-tagged MpDRP3l, which is a transcriptional variant from the Mp*DRP3* gene (Nagaoka et al. 2017).

At Stage 0 and 1, 3×HA-MpDRP3l was observed as many puncta located on mitochondria in spermatids, suggesting that mitochondrial fission frequently occurs at these stages (**Figure 9**). However, at Stage 3, the signal from 3×HA-MpDRP3l was hardly detected in spermatids, probably reflecting that mitochondrial fission scarcely occurs at this stage (**Figure 9**). Since fragmented mitochondria were frequently observed at Stage 0 and 1, mitochondria fission should mainly occur at an early stage of spermiogenesis (**Figures 4 and 9**).

In mammals, the relationship between mitochondrial fission and the distribution and

maintenance of mitochondrial DNA (mtDNA) has been intensively analyzed (Chapman et al. 2020). Therefore, I hypothesized that frequent fission of mitochondria in an early stage of spermiogenesis is important for mtDNA dynamics during spermiogenesis in *M. polymorpha*. Since organelle DNA is often visualized by the fluorescent dyes such as DAPI (Nishimura et al. 1999; Matsushima et al. 2011), I observed organelle DNA in antheridial cells using these dyes. However, organelle DNA was not observed by using these dyes under my experimental condition (**Figure 10**). I also tried to visualize organelle DNA using the anti-DNA antibody, as previously performed in other organisms (Liu et al. 2004; Sasaki et al. 2017). While plastid DNA was visualized, mtDNA was hardly observed (**Figure 11**). Thus, I cannot conclude whether mitochondrial fission is related to the distribution and maintenance of mtDNA during spermiogenesis in *M. polymorpha*.

Reorganization of mitochondria during spermiogenesis requires mitochondrial fission

I then investigated whether mitochondrial fission is required for reorganization of mitochondria during spermiogenesis. The Mp*drp3* knockout mutant exhibits a severe defect in thallus growth (Nagaoka et al. 2017). Therefore, to inhibit the function of MpDRP3 only during spermatogenesis, I used a dominant negative form of MpDRP3. Replacement of the lysine residue in the GTP-binding element I to alanine is widely used to generate a dominant negative form of dynamin, and this mutant form of dynamin exhibits no GTPase activity while retaining the GTP binding activity (Arimura and Tsutsumi 2002; Naylor et al. 2006). To confirm that the transient expression of MpDRP3l^{K75A} (**Figure 12A**) exerts a dominant negative effect, the expression of MpDRP3l^{K75A} was induced by β-estradiol in thallus cells (Nishihama et al. unpublished). In contrast to wild-type MpDRP3l (MpDRP3l^{WT}), expression of MpDRP3l^{K75A} resulted

in elongated mitochondria, indicating that this mutant version of MpDRP3 exerted a dominant-negative effect on mitochondrial fission (**Figure 12B**).

Next, I investigated the effect of MpDRP3l^{K75A} during spermiogenesis. To restrict the effect of MpDRP3l^{K75A} to spermatogenesis, I used the promoters of Mp*DUO1* and Mp*MS1*, which are predominantly expressed in antheridia (Higo et al. 2016; Higo et al. 2018). Transgenic plants expressing MpDRP3l^{K75A} driven by these promoters formed wild type-like spermatozoids in all lines I examined, which were also fertile with an exception for $_{pro}$Mp*DUO1*:*mTurquoise2*-Mp*DRP3l*^{K75A} #2 (**Figures 13 and 14 and Table 4**). The sterility of this line could be due to insertion of transfer DNA (T-DNA) cassette harboring $_{pro}$Mp*DUO1*:*mTurquoise2*-Mp*DRP3l*^{K75A} into the locus of genes which is required for spermatozoid functions. Intriguingly, however, MpDRP3l^{K75A} affected morphology of mitochondria in spermatozoids. I found that four types of mitochondria were produced in the transgenic plants expressing MpDRP3l^{K75A}: spermatozoids with one anterior and one posterior mitochondria like the wild-type spermatozoid (Type 1), spermatozoids with only one anterior mitochondrion (Type 2), spermatozoids with two closely associated mitochondria (Type 3), and spermatozoids additional mitochondria to one anterior and one posterior mitochondria (Type 4) (**Figure 13 and Table 5**). Regardless of these effects on mitochondria morphology, MpDRP3l^{K75A} did not markedly affect the total area of mitochondria in spermatozoids (**Figure 15**). I confirmed that MpDRP3l^{K75A} was expressed at Stage 0 in all three lines of $_{pro}$Mp*MS1*:*mTurquoise2*-Mp*DRP3l*^{K75A} and one of three lines of $_{pro}$Mp*DUO1*:*mTurquoise2*-Mp*DRP3l*^{K75A} I observed (**Figure 16**). These results suggest that MpDRP3l^{K75A} seemed not to affect mitochondria reorganization at an early stage of spermiogenesis, probably because of the reason I discuss below.

Because only one anterior mitochondrion was observed in Stage 3 wild-type spermatids and Type 2 spermatozoids without the posterior mitochondrion was observed in MpDRP3l^{K75A}-expressing spermatozoids (**Figures 4 and 13**), I hypothesized that the posterior mitochondrion could be formed by division of the anterior mitochondrion. Dynamin in *S. cerevisiae*, Dnm1, is reported to be not dissociated from the fission site of mitochondria to accumulate at this site when the mutation equivalent to MpDRP3l^{K75A} is introduced (ScDnm1^{K41A} in **Figure 12A**) (Naylor et al. 2006). If the posterior mitochondrion in spermatozoids of *M. polymorpha* is formed by division of the anterior mitochondrion, MpDRP3l^{K75A} would be accumulated at the anterior mitochondrion in the Type 2 and 3 spermatozoids. Concordant with this hypothesis, MpDRP3l^{K75A} was found to be localized to the anterior mitochondrion in Type 2 and 3, but not in Type 1 and 4 spermatozoids (**Figure 17**). In Type 2 spermatozoids, MpDRP3l^{K75A} was detected at the posterior region of the anterior mitochondrion, and in Type 3 spermatozoids, MpDRP3l^{K75A} was found to be accumulated between two anterior mitochondria (**Figure 17**). Since the mean diameter of mitochondrial constriction sites is about 100 nm in *S. cerevisiae* (Ingerman et al. 2005), the signal from Mito-Citrine, which is targeted to the matrix of mitochondria, might be hardly detected at the constriction site under my experimental condition, and two anterior mitochondria in Type 3 spermatozoids could be connected with each other. Distinct from MpDRP3l^{K75A}, MpDRP3l^{WT} driven by the Mp*DUO1* promoter was not localized to the anterior mitochondrion, while it was occasionally found at the middle region of spermatozoids (**Figure 18**). This localization might reflect binding of MpDRP3 with spline, which is a microtubule-containing structure aligned along the elongated nucleus in spermatozoids (**Figure 1B**), since *A. thaliana* DRP3 is shown to interact with tubulin (wang et al. 2012). Signals from

MpDRP3l^{K75A} were observed in the posterior region of all types of spermatozoids, which could represent remnants of the cytosol (**Figure 17**). These results suggest that the posterior mitochondrion is formed by fission from the anterior mitochondrion.

DISCUSSION

Observation of various organelles using a newly established method

In this study, I aimed to perform detailed observation of various organelles during spermiogenesis according to classification of developmental stages developed by Minamino et al. (unpublished). I applied several modern techniques to this study. First, I used fluorescent protein-tagged organelle markers recently established for studies in *M. polymorpha* (Kanazawa et al. 2016; Mano et al. 2018) to visualize various organelles including peroxisomes, which is difficult to be identified by TEM (**Table 3**). Second, I observed antheridial cells separated from other cells by digesting their cell wall, which allowed me to observe dynamic change of distribution and structures of organelles and flagella during spermiogenesis. This strategy was effective because numerous antheridial cells are piled up, which make observation of fine cellular structures difficult. Recently, several *M. polymorpha* mutants defective in spermatozoid formation were isolated, however, it remains unclear which processes in spermatogenesis are compromised in these mutants (Koi et al. 2016; Higo et al. 2018; Hisanaga et al. 2019a; Hisanaga et al. 2019b). The method I developed in this study and information on organelle reorganization would be useful for analyses of these mutants, which would lead to better understanding the molecular mechanism of spermiogenesis in *M. polymorpha*.

Drastic change in mitochondria morphology during spermiogenesis

Sperms in plants and animals generally possess mitochondria with unique characteristics. For instance, mitochondria exhibit a helical sheath surrounding axonemal structures at the middle pieces in mammalian spermatozoa (Ho and Wey 2007). For most of bryophyte spermatozoids, they possess two mitochondria: one at the anterior and the other at the

posterior region of their cell bodies. Previous TEM observation suggested that the two mitochondria are formed via the mono-mitochondrion stage in hornworts and mosses, although in liverworts mono-mitochondrion stage was not believed to exist during spermiogenesis (Renzaglia and Garbary 2001). However, I found that only one mitochondrion exists in Stage 3 of spermiogenesis and that the posterior mitochondrion is formed by fission from the anterior mitochondrion in the liverwort *M. polymorpha* (**Figures 4, 13, and 17**). This discovery also demonstrated that molecular cell biological tools that I employed in this study are useful for studies of bryophyte spermiogenesis.

Although this study showed MpDRP3-mediated fission of the anterior mitochondrion is involved in formation of the posterior mitochondrion, the function of two mitochondria in spermatozoids remains unknown. Since the anterior mitochondrion is localized just beneath the basal bodies, the anterior mitochondrion might supply ATP and/or other metabolites, which are required for flagellar formation and/or motility. On the other hand, the posterior mitochondrion is localized far from the base of flagella, implying that the posterior mitochondria could have no functions in supply to flagella. The posterior mitochondrion is tightly associated with the plastid. Therefore, the posterior mitochondrion might be required for the function of the plastid (see below). Intriguingly, Type 2 and 3 spermatozoids observed in the experiment using a dominant negative form of MpDRP3 exhibited wild type-like morphology except for an abnormal number of mitochondria, suggesting that the posterior mitochondrion is not required for spermatozoid morphogenesis (**Figure 13**). However, although these spermatozoids except for the line #2 of $_{pro}$Mp*DUO1*:*mTurquoise2*-Mp*DRP3l*^{K75A} are fertile, I could not conclude that the posterior mitochondrion is not required for proper function of spermatozoids, because wild type-like spermatozoids (Type 1) are also formed in plants

expressing MpDRP3l^{K75A}. Further studies on motility and fertility of the Type 2 and 3 spermatozoids would be needed to reveal the precise function of the posterior mitochondrion.

Although mitochondrial fission frequently occurs at Stage 0 and 1, dominant negative effects of MpDRP3l^{K75A} appeared to be exerted only in formation of the posterior mitochondrion (**Figures 9 and 13**). Given the detected expression of MpDRP3l^{K75A} driven by the Mp*MS1* promoter in Stage 0 (**Figure 16**), it is unlikely that the late-stage specific inhibitory effect of MpDRP3l^{K75A} is due to absence of the protein in earlier stages. In *S. cerevisiae*, dominant negative effects of dynamin depend on the expression ratio of dominant negative to wild-type dynamin (Otsuga et al. 1998). Since the strong signal from 3×HA-MpDRP3l driven by its native promoter was detected at Stage 0 and 1, and its signal was reduced at Stage 3 (**Figure 9**), the stage-specific dominant negative effect of MpDRP3l^{K75A} might reflect an elevated ratio of the mutant MpDRP3 protein in Stage 3. It could be also possible that MpDRP3 is dispensable for mitochondria reorganization at an early stage of spermiogenesis (see discussion in **Chapter 2**).

For the investigation of the role of mitochondrial fission at the early stage of spermiogenesis, I investigated dynamics of mtDNA during spermiogenesis in *M. polymorpha*, since mitochondrial fission is reported to be related to the dynamics of mtDNA in mammals (Chapman et al. 2020). However, I did not succeed in visualizing mtDNA in antheridial cells under my experimental condition, and the relationship between mitochondrial fission and mtDNA during spermiogenesis remains still unclear (**Figures 10 and 11**). It is possible that mtDNA could be degraded before spermiogenesis. Observation of mtDNA dynamics in the young antheridial cells including antheridium initial cells (Shimamura 2016) must be needed to investigate this possibility. Another

important role of mitochondrial fission is the degradation of mitochondria (Twig et al. 2008; Rambold et al. 2011; Mao et al. 2013; Yamashita et al. 2016). Around the stage when mitochondria undergo fission frequently, the total area of mitochondria was decreased, implying that mitochondrial fission might be involved in the degradation of mitochondria by autophagy (see discussion in **Chapter 2**).

Plastid dynamics during spermiogenesis

As shown in **Figure 5**, the shape of the plastid also drastically changed during spermiogenesis. Dynamic changes of intra-plastid structures during spermiogenesis including increased deposition of starch and disappearance of thylakoids are reported by TEM analyses in some land plants (Renzaglia and Garbary 2001), although the relationship between the morphological changes of the plastid and reorganization of intra-plastid structures remains unknown. Furthermore, a precise function of plastids in spermatozoids remains unknown, whereas some studies implied that starch-filled plastids could act as weights for efficient motility of spermatozoids (Renzaglia and Garbary 2001). Further analyses are needed to reveal biological significance of the plastid transfiguration during spermiogenesis in land plants.

ER dynamics during spermiogenesis

The nuclear shape drastically changes during spermiogenesis in most land plants (Renzaglia and Garbary 2001). However, it still remains unknown how this morphological change occurs during spermiogenesis in land plants. In *A. thaliana*, nuclear shaping involves various factors such as cytoskeletons, lamin-like proteins, chromatin composition, and proteins on the nuclear envelop (Meier et al. 2016; Goswami

et al. 2020). During spermiogenesis chromatin condensation occurs, which might involve protamine in *M. polymorpha* (Higo et al. 2016; D'Ippolito et al. 2019). The composition of the nuclear envelop could also change during spermiogenesis, as the signal from soluble and integral membrane ER proteins were markedly decreased during spermiogenesis (**Figure 6**). These changes might be associated with nuclear shaping during spermiogenesis. An intriguing result for the soluble ER marker is that it remains at the anterior and posterior regions of cell bodies of spermatozoids. Although the ER was not reported to be remained in bryophyte spermatozoids, Kreitner (1977a) showed that the anterior tip of the nucleus is embedded between the spline and the anterior mitochondrion during spermiogenesis of *M. polymorpha*. Accumulation of the ER marker at the anterior region of spermatozoid cell bodies could represent this anterior tip of the nucleus, and soluble proteins in this region might be escaped from degradation. It is also possible that the soluble ER marker is in other compartments than the ER in spermatozoids, given that the ER membrane protein MpSEC20 tagged with mCitrine was not detected in spermatozoids (**Figure 6**). Further analyses are needed to determine what this structure is.

Golgi dynamics during spermiogenesis

The size and number of the Golgi apparatus also dynamically changed during spermiogenesis. Intriguingly, one large structure with the Golgi marker was observed at Stage 1 and 2 (**Figure 7**). The large Golgi apparatus is also observed in another liverwort *B. pusilla* (Renzaglia and Duckett 1987), suggesting that at least in the liverwort the large Golgi apparatus is observed during spermiogenesis. However, the function of this large Golgi apparatus still remains unknown. Studies of metazoan systems suggested that the

size of the Golgi apparatus could relate with the Golgi function including membrane trafficking (Sengupta and Linstedt 2011). Vacuolar transport is highly activated during spermiogenesis in *M. polymorpha* (Minamino et al. 2017) , thus formation of the large Golgi apparatus might be required for underpinning the vacuolar transport during spermiogenesis.

Peroxisome dynamics during spermiogenesis

Despite intensive TEM observation conducted thus far, little information is available for on peroxisome dynamics during spermiogenesis. In this study, I observed peroxisome dynamics during spermiogenesis using the peroxisome marker (**Figure 8**). Peroxisomes remained in the cytosol until late stages of spermiogenesis, suggesting that peroxisomal functions could be required in earlier stages of spermiogenesis. Although the peroxisome is indispensable for mouse spermatogenesis (Brauns et al. 2019), it still remains unclear how the peroxisome is involved in spermatogenesis. I could not detect the signal from Citrine-PTS1 in the mature spermatozoid, suggesting that the peroxisome is removed from spermatids during Stage 4 to 5 (**Figure 8**). Consistent with my observation, spermatozoids in bryophytes have been reported to possess no peroxisome-like structures (Renzaglia and Garbary 2001). Rat spermatozoa also possess no peroxisomes (Figueroa et al. 2000). These results indicated that peroxisomes could be required for spermatogenesis, not spermatozoids.

Each organelle is removed at a distinctive stage

I revealed that the Golgi apparatus and the peroxisome are removed during spermiogenesis (**Figures 7 and 8**), and the total area of mitochondria is decreased during

spermiogenesis (**Figure 4**). Intriguingly, removal of these organelle occurs at different timing. While the Golgi proteins are removed around Stage 3, the peroxisome protein and the cytosol are removed during Stage 4 to 5 (**Figures 1, 7, and 8**). The decrease in the total area of mitochondria occurs at Stage 1 and 2 (**Figure 4**). Based on these results, it is unlikely that the whole cytoplasm is removed by bulk degradation of the cytoplasm during spermiogenesis in *M. polymorpha*. Rather, each organelle should be selectively removed at a certain stage of spermiogenesis. Further analyses are needed to know how removal of each organelle is regulated during spermiogenesis in *M. polymorpha*, which will be addressed in the next chapter.

TABLES

Table 3. Organelle markers used in Chapter 1

Organelle	Marker	Reference	Promoter in this study
Mitochondrion	Mito-Citrine	This study	$_{pro}$Mp*EF1α*
Plastid	MpPGM1-Citrine	This study	$_{pro}$Mp*EF1α*
ER	SP-mCitrine-HDEL	Mano et al. 2018	$_{pro}$Mp*EF1α*
	mCitrine-MpSEC20	Kanazawa et al. 2016	$_{pro}$Mp*DUO1*
Golgi	ST-Venus	Kanazawa et al. 2016	$_{pro}$Mp*DUO1*
	mCitrine-MpSFT1	Kanazawa et al. 2016	$_{pro}$Mp*DUO1*
	mCitrine-MpGOS11	Kanazawa et al. 2016	$_{pro}$Mp*DUO1*
Peroxisome	Citrine-PTS1	Mano et al. 2018	$_{pro}$Mp*EF1α*

Table 4. Fertility of spermatozoids expressing a dominant negative form of MpDRP3

		Fertility (%)	
$_{pro}$Mp*DUO1*	*K75A* #1	100	n = 9
	K75A #2	0	n = 9
	K75A #3	100	n = 9
	WT #1	100	n = 9
	WT #2	100	n = 9
	WT #3	88.9	n = 9
$_{pro}$Mp*MS1*	*K75A* #1	100	n = 9
	K75A #2	100	n = 9
	K75A #3	100	n = 9
	WT #1	100	n = 7
	WT #4	100	n = 10
	WT #5	100	n = 10

The percentage of archegoniophores with yellow sporangia in **Figure 14**. n: the number of archegoniophores used for crossing.

Table 5. Effects of dominant negative effects of MpDRP3l^{K75A} on spermiogenesis

		(%)				
		Type 1	**Type 2**	**Type 3**	**Type 4**	
$_{pro}$Mp*DUO1*	*K75A* #1	36.0	39.3	19.7	4.9	n = 61
	K75A #2	24.2	53.0	22.7	0	n = 66
	K75A #3	10.2	55.9	23.7	10.2	n = 59
	WT #1	100	0	0	0	n = 50
	WT #2	98.4	0	0	1.6	n = 30
	WT #3	94.0	4.0	0	2.0	n = 30
$_{pro}$Mp*MS1*	*K75A* #1	17.6	55.8	17.6	8.8	n = 34
	K75A #2	11.4	74.3	5.7	8.6	n = 35
	K75A #3	14.2	65.7	11.4	8.6	n = 35
	WT #1	100	0	0	0	n = 20
	WT #4	100	0	0	0	n = 30
	WT #5	96.7	0	0	3.3	n = 30

The percentage of each type of spermatozoids expressing $_{pro}$Mp*EF1α*:*Mito-Citrine* /$_{pro}$Mp*DUO1*:*mTurquoise2-MpDRP3l*^{WT} or ^{K75A} or $_{pro}$Mp*EF1α*:*Mito-Citrine*/ $_{pro}$Mp*MS1*:*mTurquoise2-MpDRP3l*$^{WT\text{ or }K75A}$ in **Figure 13**. n: the number of spermatozoids.

FIGURES

	Stage 0	Stage 1	Stage 2	Stage 3	Stage 4	Stage 5 (Spermatozoid)
Nucleus	Spherical	Spherical	Elliposidal	Crescent	Cylindlical	Helical (Fully elongated)
Flagellum	-	+	+	+	+	+
Cytosol	Abundant	Abundant	Abundant	Abundant	Abundant	Mostly removed

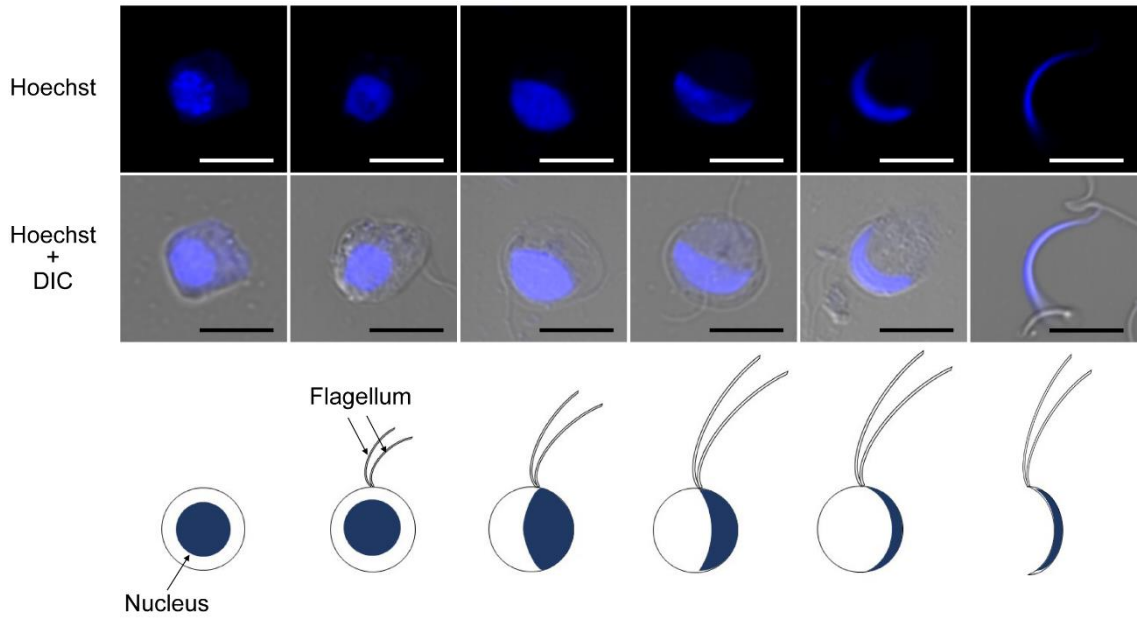

Figure 2. Stages of spermiogenesis in *M. polymorpha*

Six stages of spermiogenesis in *M. polymorpha* (Minamino et al. unpublished). Cell wall-digested antheridial cells and spermatozoids are used. The blue color indicates the fluorescence from Hoechst. DIC: differential interference contrast. Bars = 5 μm.

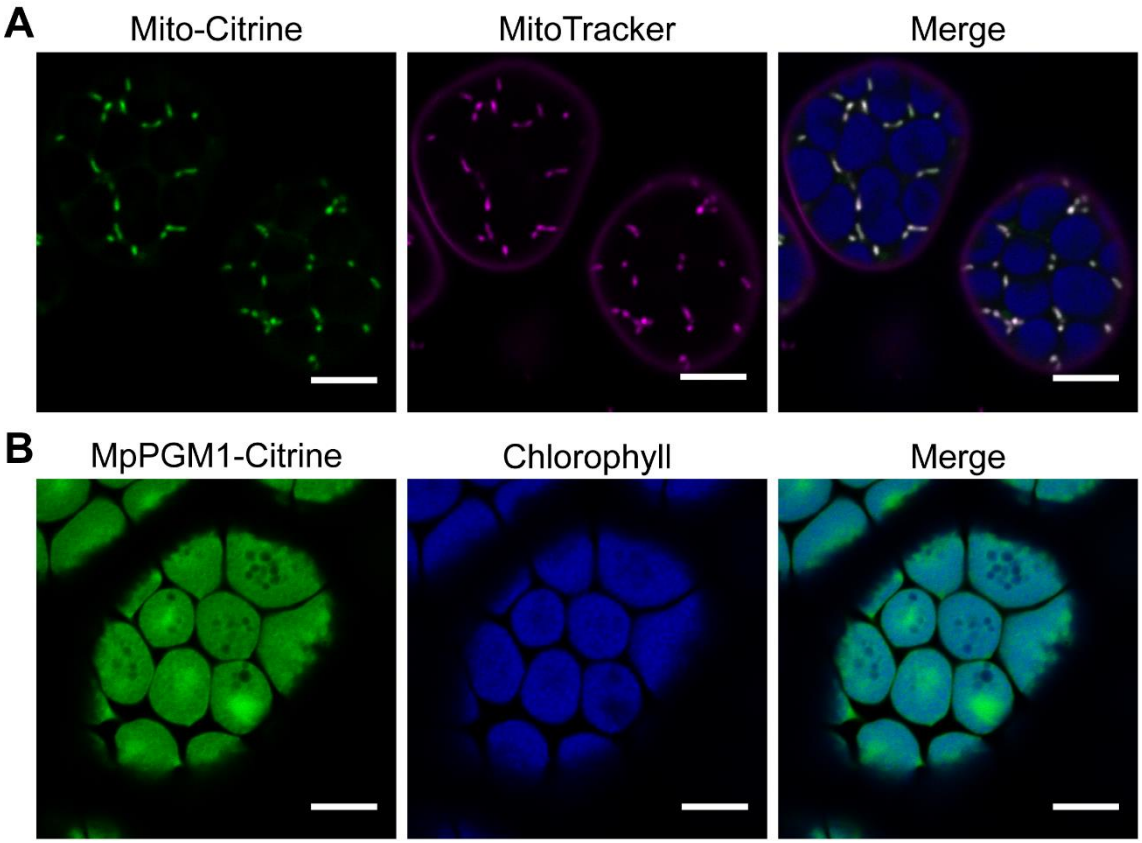

Figure 3. Mitochondria and plastid markers in *M. polymorpha*

Subcellular localization of Mito-Citrine (**A**) and MpPGM1-Citrine (**B**) in thallus cells. MitoTracker labelled the mitochondria and apoplast. The green, magenta, and blue colors indicate the fluorescence from Citrine, MitoTracker, and autofluorescence of chlorophyll, respectively. Bars = 10 μm.

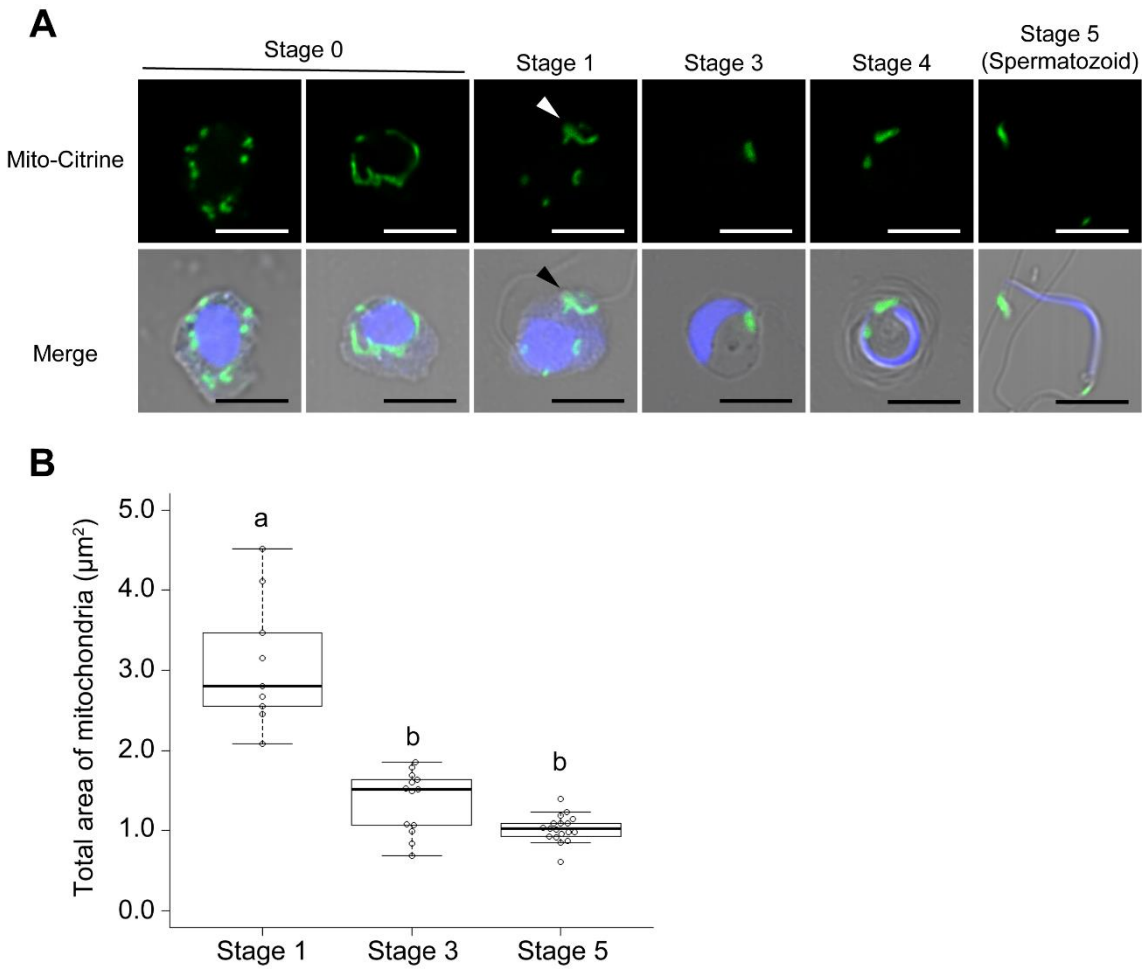

Figure 4. Mitochondria dynamics during spermiogenesis

(**A**) Subcellular localization of Mito-Citrine in cell wall-digested antheridial cells and spermatozoids. The green and blue colors indicate the fluorescence from Citrine and Hoechst, respectively. Bars = 5 μm. (**B**) Quantification of the total area of mitochondria in Stage 1, 3, and 5. n = 9 cells for Stage 1, 13 for Stage 3, and 18 for Stage 5. The boxes and solid lines in the boxes indicate the first quartile and third quartile, and median values, respectively. The whiskers indicate 1.5× interquartile ranges. Different letters denote significant differences based on Tukey's test ($p < 0.05$).

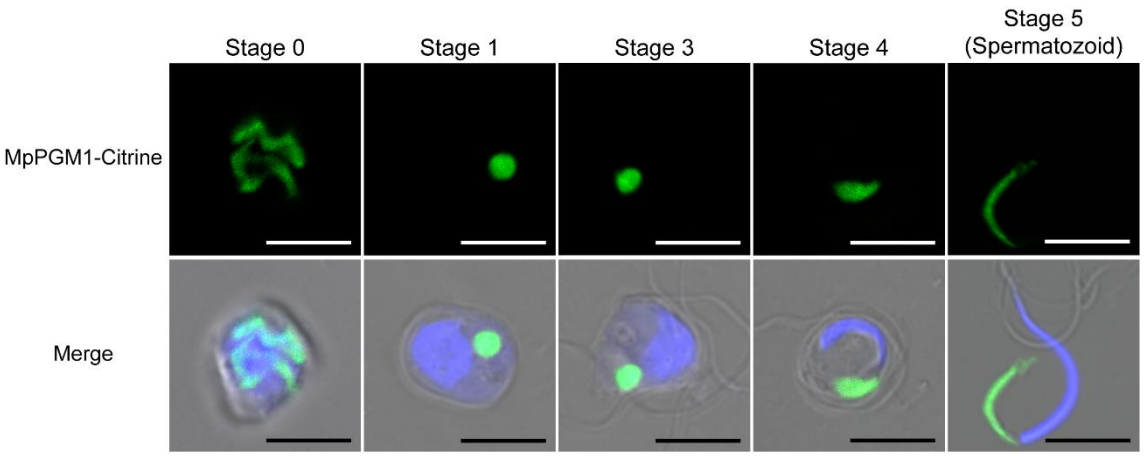

Figure 5. Plastid dynamics during spermiogenesis

Subcellular localization of MpPGM1-Citrine in cell wall-digested antheridial cells and spermatozoids. The green and blue colors indicate the fluorescence from Citrine and Hoechst, respectively. Bars = 5 μm.

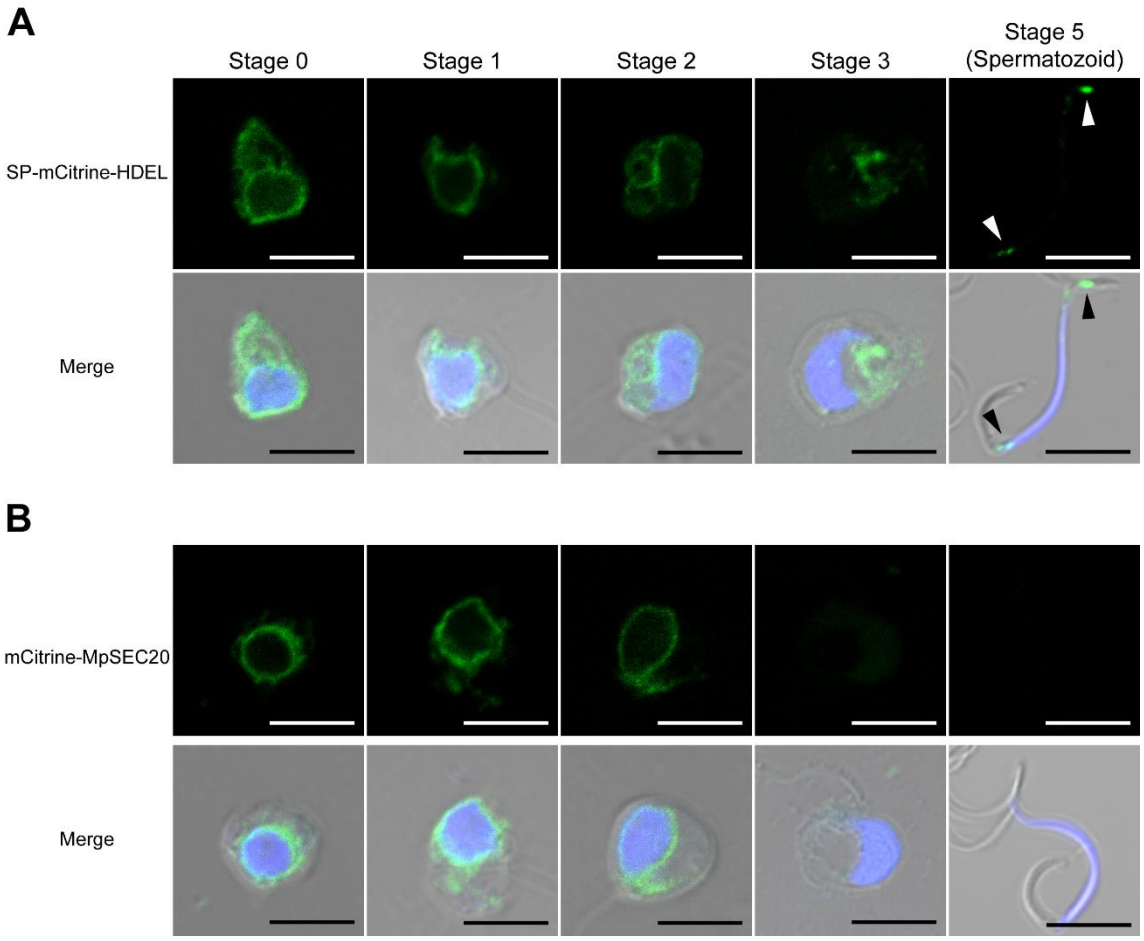

Figure 6. ER dynamics during spermiogenesis

Subcellular localization of SP-mCitrine-HDEL (**A**) or mCitrine-MpSEC20 (**B**) in cell wall-digested antheridial cells and spermatozoids. Arrowheads indicate remained SP-mCitrine-HDEL in spermatozoids. The green and blue colors indicate the fluorescence from mCitrine and Hoechst, respectively. Bars = 5 μm.

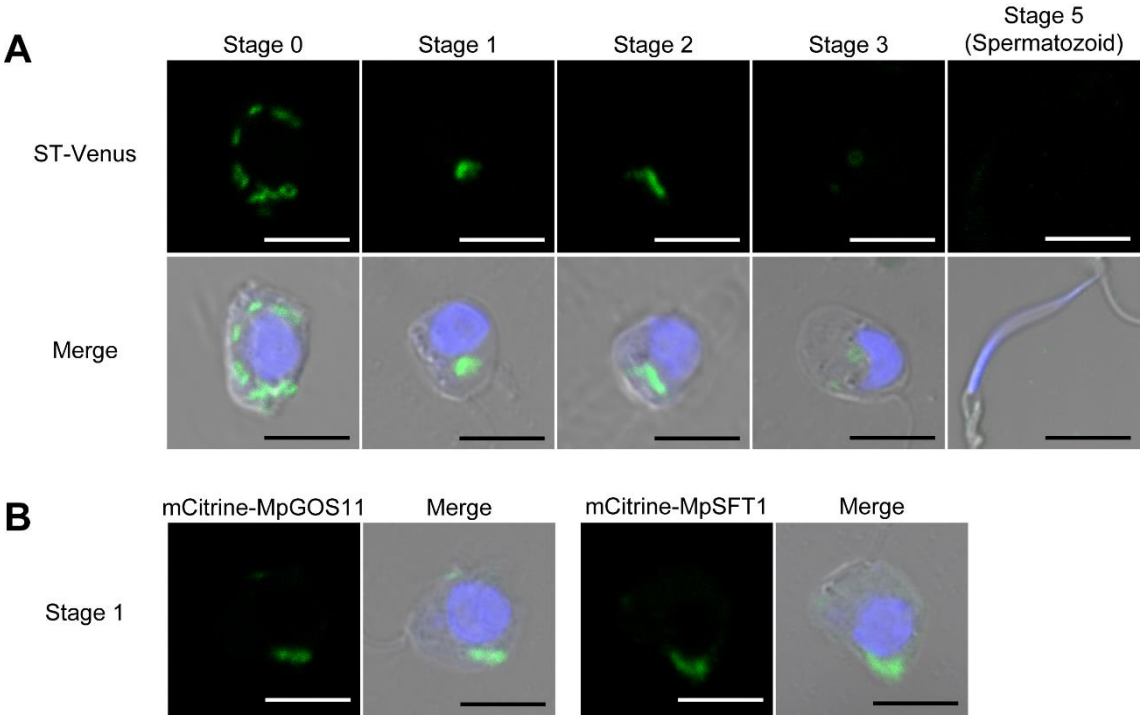

Figure 7. Golgi dynamics during spermiogenesis

Subcellular localization of ST-Veuns (**A**) and mCtrine-MpGOS11 and mCitrine-MpSFT1 (**B**) in cell wall-digested antheridial cells and spermatozoids. The green and blue colors indicate the fluorescence from Venus or mCitrine and Hoechst, respectively. Bars = 5 μm.

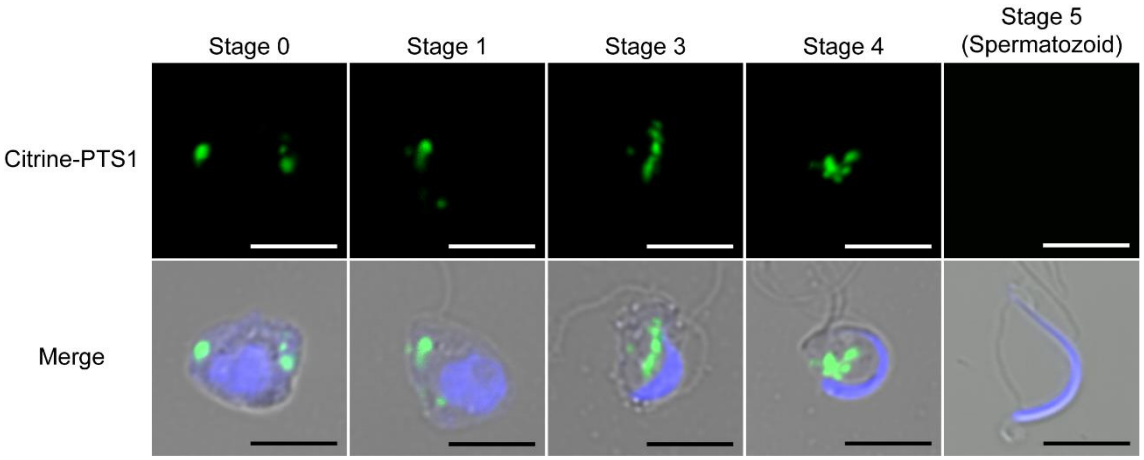

Figure 8. Peroxisome dynamics during spermiogenesis

Subcellular localization of Citrine-PTS1 in cell wall-digested antheridial cells and spermatozoids. The green and blue colors indicate the fluorescence from Citrine and Hoechst, respectively. Bars = 5 μm.

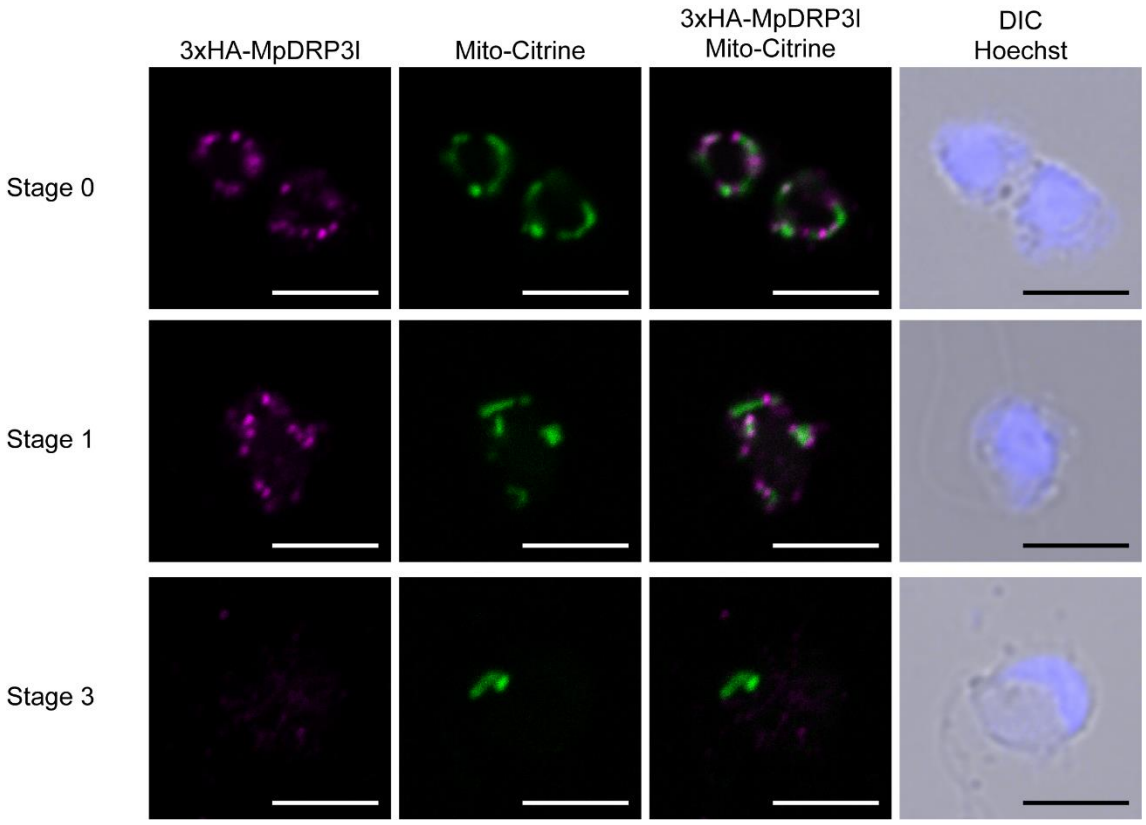

Figure 9. Localization of MpDRP3 during spermiogenesis

Subcellular localization of 3×HA-MpDRP3l in cell wall-digested antheridial cells The magenta, green, and blue colors indicate the fluorescent from Alexa Fluor 546, Citrine, and Hoechst, respectively. Bars = 5 μm.

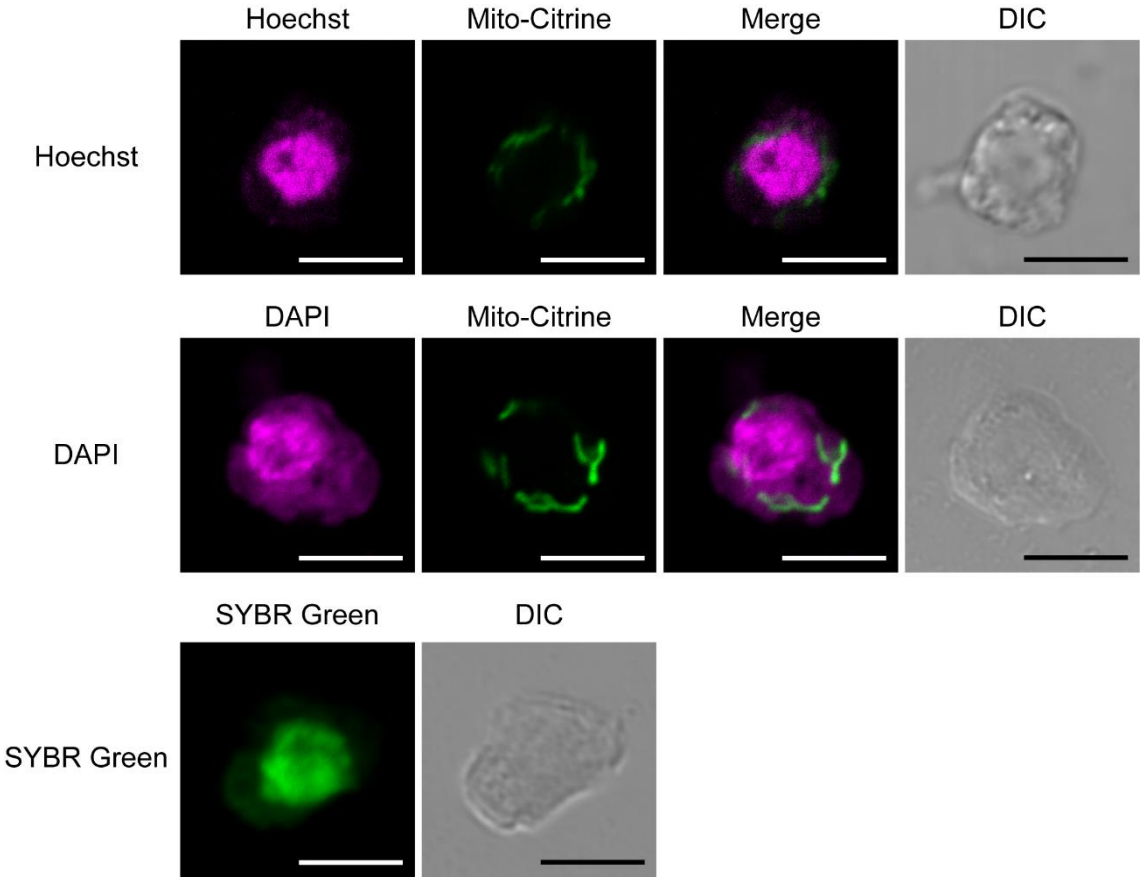

Figure 10. DNA labelling by fluorescent dyes cell wall-digested antheridial cells

DNA is labelled by the fluorescent dyes (Hoechst, DAPI, and SYBR Green) in Stage 0 cells. In the top and middle panels, the magenta and green colors indicate the fluorescent from Hoechst or DAPI and Citrine, respectively. In the bottle panel, the green color indicates the fluorescent from SYBR Green. Bars = 5 μm.

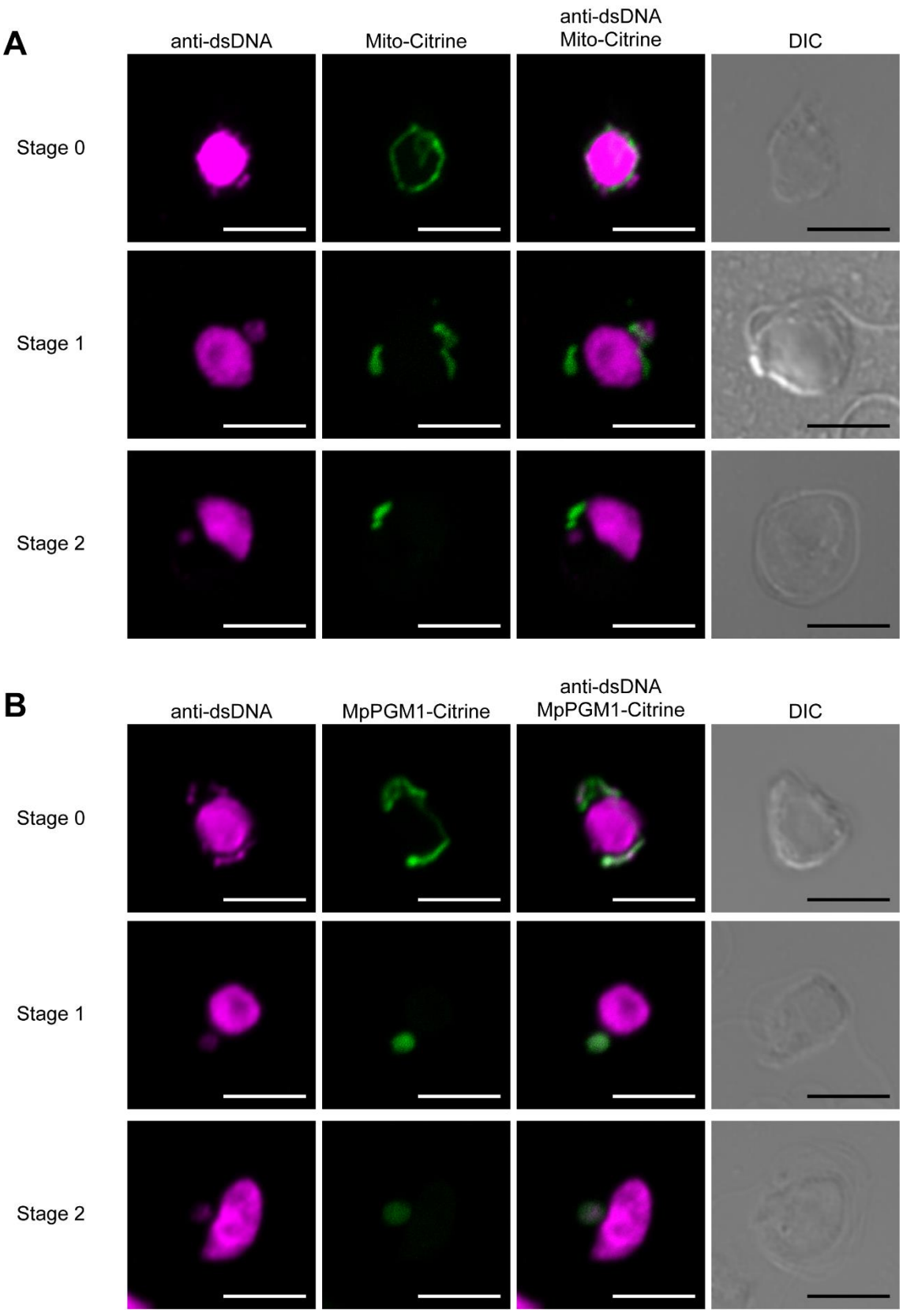
A
anti-dsDNA
Mito-Citrine
anti-dsDNA
Mito-Citrine
DIC
Stage 0
Stage 1
Stage 2
B
anti-dsDNA
MpPGM1-Citrine
anti-dsDNA
MpPGM1-Citrine
DIC
Stage 0
Stage 1
Stage 2

Figure 11. DNA labelling by the anti-dsDNA antibody in cell wall-digested antheridial cells

DNA is labelled by the anti-dsDNA antibody in Stage 0, 1, and 2 cells expressing Mito-Citrine (**A**) and MpPGM1-Citrine (**B**). The magenta and green colors indicate the fluorescent from Alexa Flour 546 and Citrine, respectively. Bars = 5 μm.

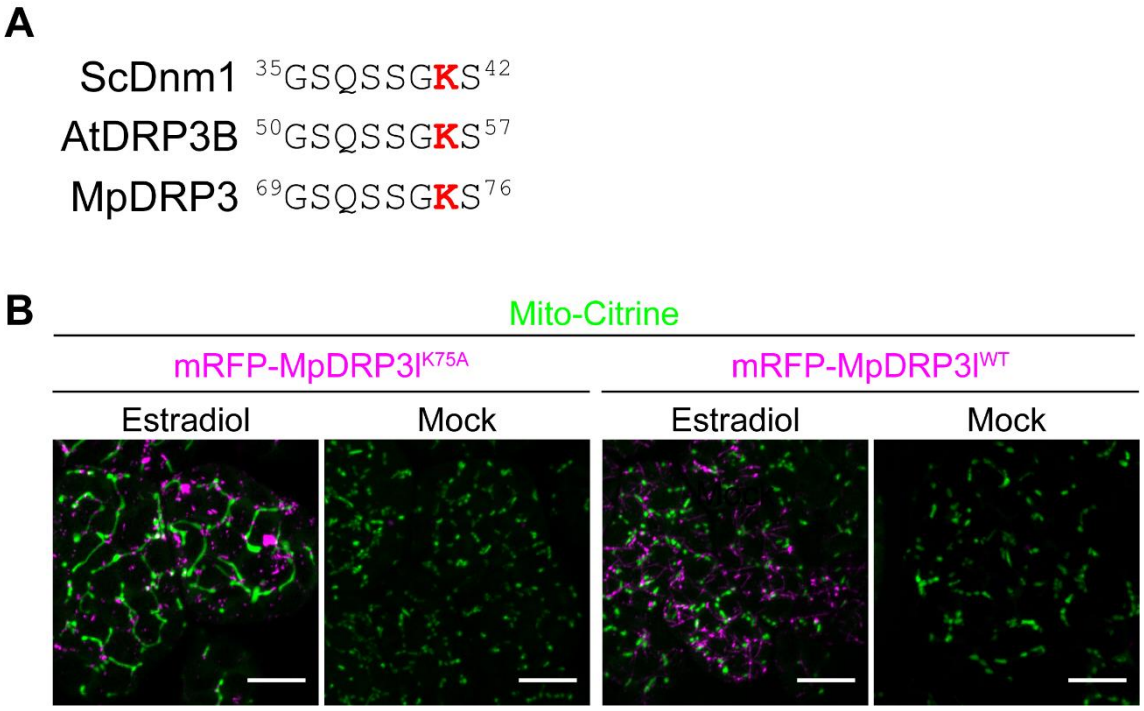

Figure 12. Dominant negative effects of MpDRP3l^{K75A} on thallus cells

(**A**) A part of alignment sequences of ScDnm1, AtDRP3B, and MpDRP3. The letter colored by red is the lysine residue which is replaced into alanine in a dominant-negative form of dynamin. Sc: *S. cerevisiae*, At: *A. thaliana*. (**B**) Induction of MpDRP3l by estradiol in thallus cells. The green and magenta colors indicate the fluorescence from Citrine and mRFP, respectively. Bars = 10 μm.

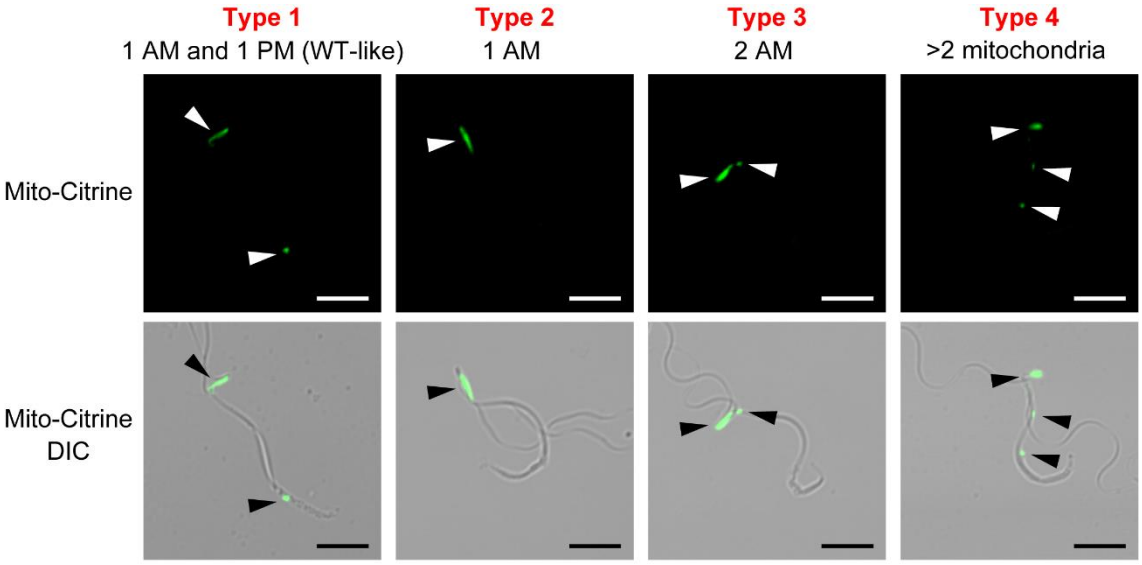

Figure 13. Dominant negative effects of MpDRP3l^{K75A} on the mitochondrial number of spermatozoids

Spermatozoids expressing mTurquoise2-MpDRP3l^{K75A} driven by the Mp*DUO1* promoter. Arrowheads indicate mitochondria labelled by Mito-Citrine. AM: anterior mitochondrion, PM: posterior mitochondrion. The green color indicates the fluorescence from Citrine. Bars = 5 μm. See also **Table 5**.

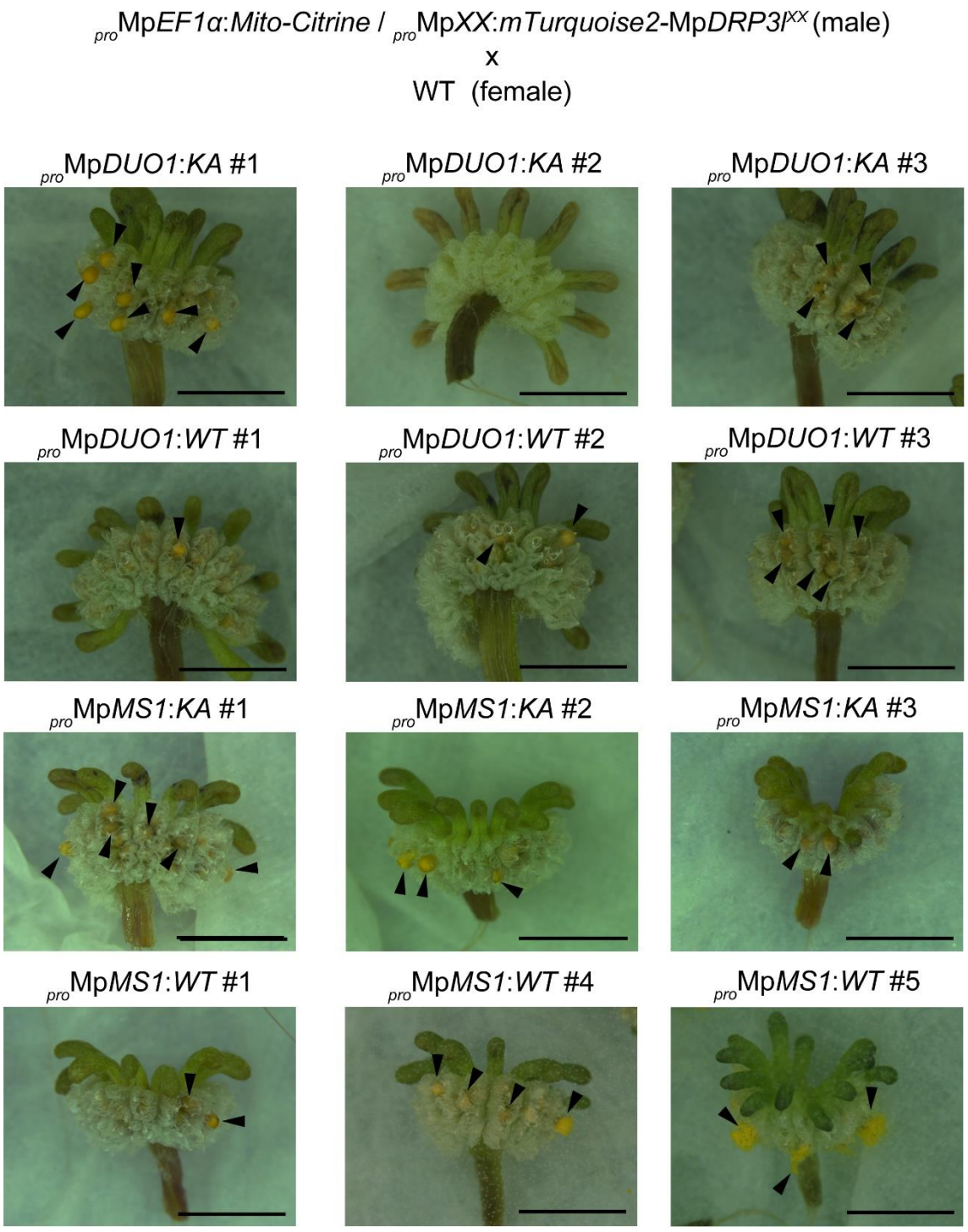

Figure 14. Fertility of spermatozoids expressing a dominant negative form of MpDRP3

Crossing of $_{pro}$Mp*EF1α*:*Mito-Citrine*/$_{pro}$Mp*DUO1*:*mTurquoise2*-Mp*DRP3l*$^{WT\ or\ K75A}$ or $_{pro}$Mp*EF1α*:*Mito-Citrine*/$_{pro}$Mp*MS1*:*mTurquoise2*-Mp*DRP3l*$^{WT\ or\ K75A}$ with wild-type (WT) female were performed, and three to five weeks after crossing archegoniophores were observed. Arrowheads indicate yellow sporangia. Bars = 0.5 cm. See also **Table 4**.

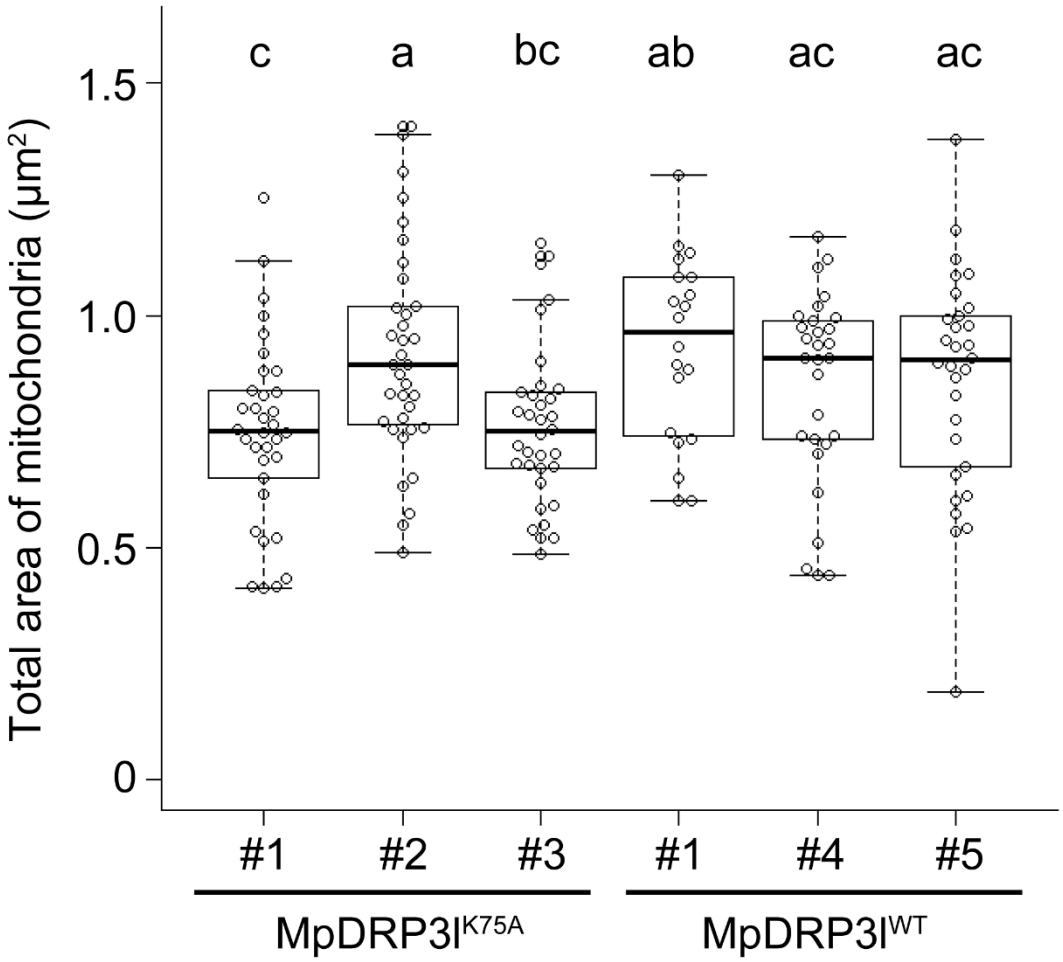

Figure 15. Dominant negative effects of MpDRP3l^{K75A} on the total mitochondrial size of spermatozoids

Quantification of the total area of mitochondria in spermatozoids expressing $_{pro}$Mp*MS1*:*mTurquoise2*-Mp*DRP3l*^{WT} or $_{pro}$Mp*MS1*:*mTurquoise2*-Mp*DRP3l*^{K75A}. n = 34 spermatozoids for K75A #1, 35 for K75A #2, 34 for K75A #3, 20 for WT #1, 29 for WT #4, and 30 for WT #5. The boxes and solid lines in the boxes indicate the first quartile and third quartile, and median values, respectively. The whiskers indicate 1.5× interquartile ranges. Different letters denote significant differences based on Tukey's test ($p < 0.05$).

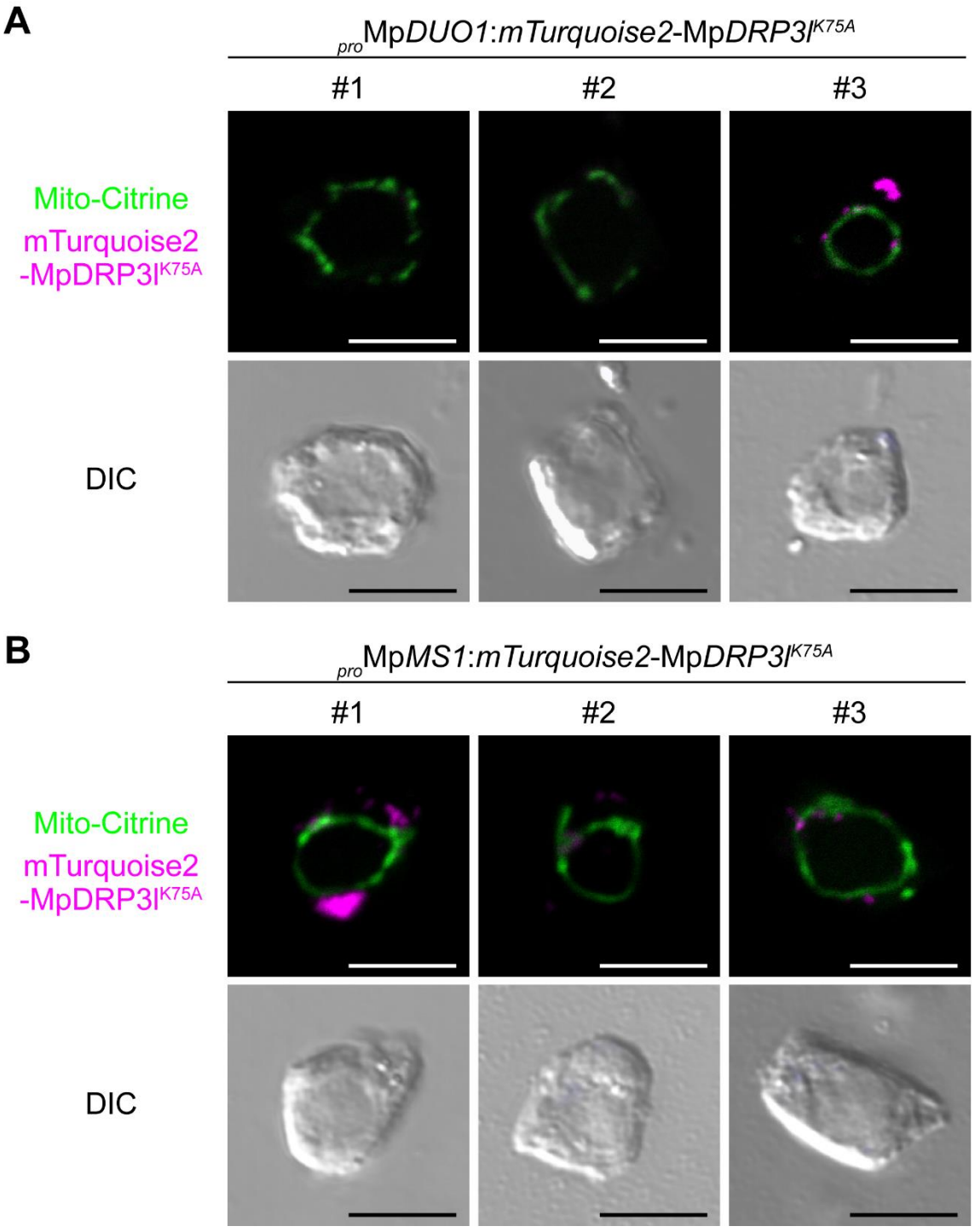

Figure 16. Expression of MpDRP3l^{K75A} at Stage 0

Subcellular localization of MpDRP3l^{K75A} driven by Mp*DUO1* promoter (**A**) or Mp*MS1* promoter (**B**) in cell-wall digested antheridial cells. The green and magenta colors indicate

the fluorescence from Citrine and mTurquoise2, respectively. Bars = 5 μm.

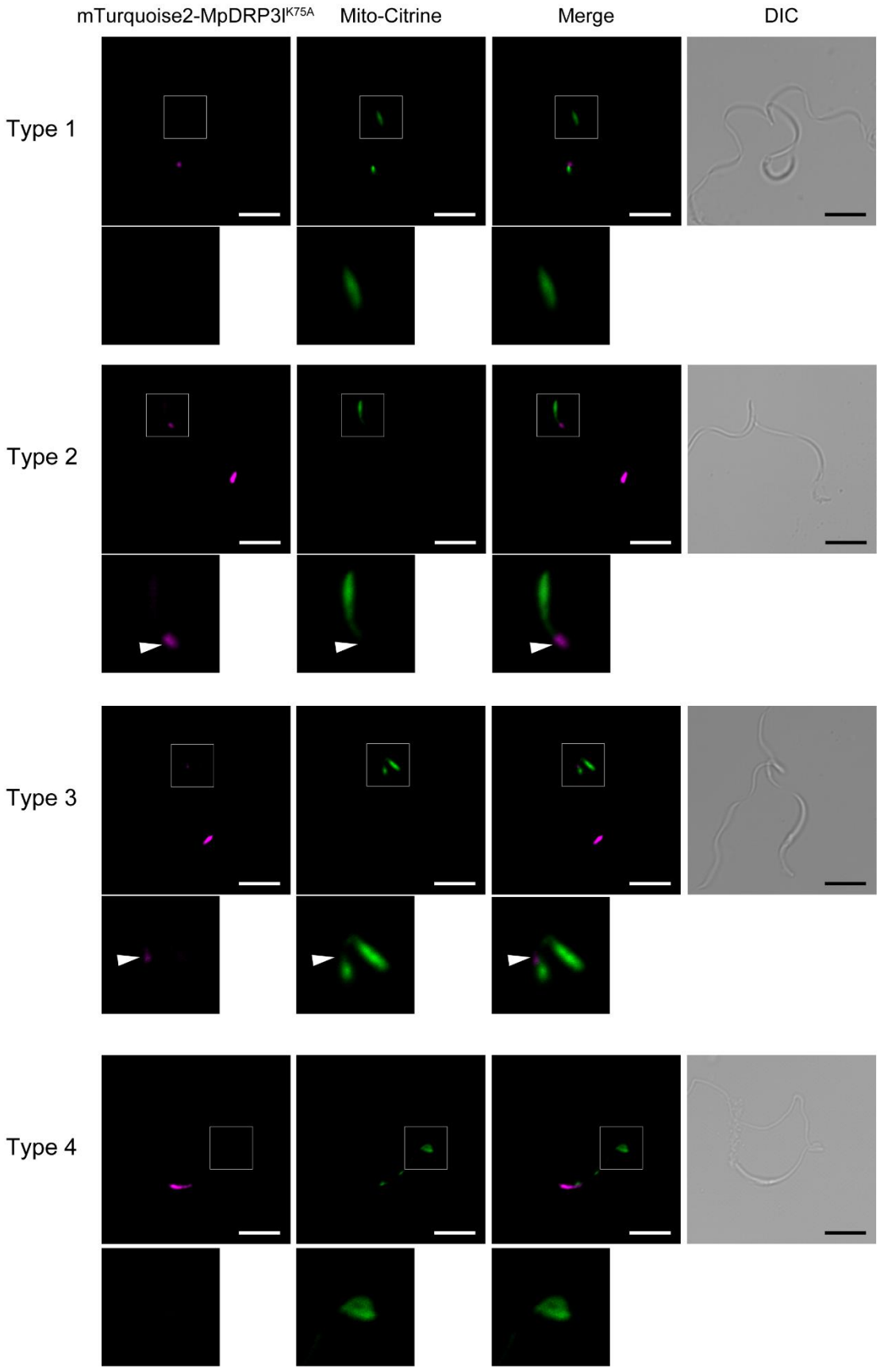
mTurquoise2-MpDRP3I^{K75A}
Mito-Citrine
Merge
DIC
Type 1
Type 2
Type 3
Type 4

Figure 17. Localization of MpDRP3l^{K75A} in spermatozoids

Subcellular localization of mTurquoise2-MpDRP3l^{K75A} driven by Mp*DUO1* promoter in each type of spermatozoids. Lower panels in each type are magnified images of the boxed regions. Arrowheads indicate MpDRP3l^{K75A} associated with the anterior mitochondrion of spermatozoids. The magenta and green colors indicate the fluorescent from mTurquoise2 and Citrine, respectively. Bars = 5 μm.

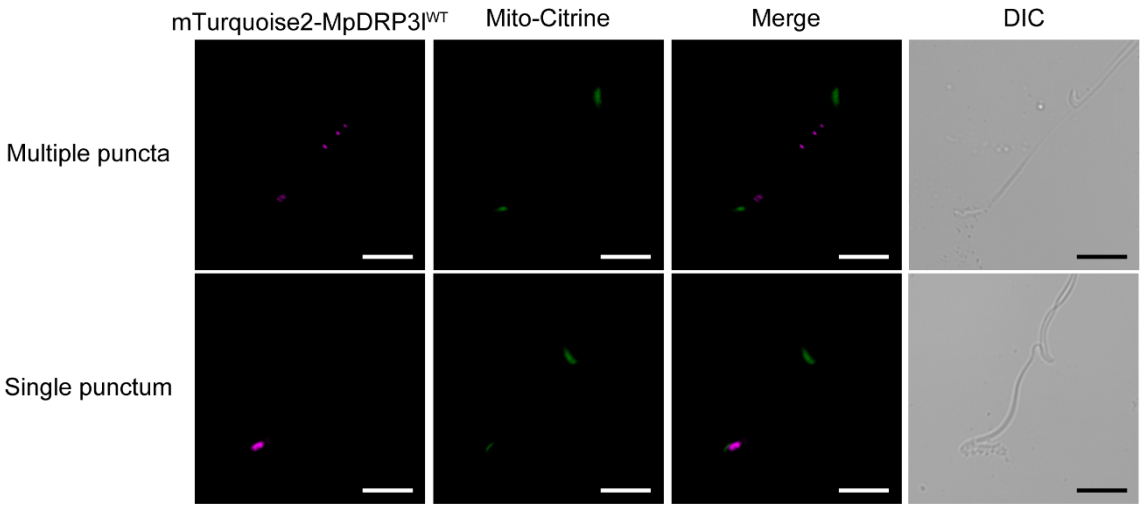

Figure 18. Localization of MpDRP3l^{WT} in spermatozoids

Subcellular localization of mTurquoise2-MpDRP3l^{WT} driven by Mp*DUO1* promoter in each type of spermatozoids. The magenta and green colors indicate the fluorescent from mTurquoise2 and Citrine, respectively. Bars = 5 μm.

CHAPTER 2: Analyses of molecular mechanisms of cytoplasm removal during spermiogenesis in *Marchantia polymorpha*

INTRODUCTION

In **Chapter 1**, I revealed dynamics of various organelles during spermiogenesis in *M. polymorpha*. The signals from the ER, Golgi, and peroxisome markers were markedly decreased during spermiogenesis. The total area of mitochondria was also decreased during Stage 1 to 3. Furthermore, spermatozoids in the bryophytes possess a limited amount of the cytosol (Renzaglia and Garbary 2001). These results indicated that drastic cytoplasm removal takes place during spermiogenesis in bryophytes including *M. polymorpha*. However, it remains largely unknown how this cytoplasm removal takes place during spermiogenesis. Cytoplasm removal also takes place during metazoan spermiogenesis. In mammals, unnecessary cytoplasmic components are degraded by the phagocytic activity of the neighboring cell (Smith and Lacy 1959; Dietert 1966; O'Donnell et al. 2011; **Figure 19**). Meanwhile, the cytoplasm of plant cells cannot be phagocytosed by neighboring cells due to the surrounding rigid cell wall (Hara-Nishimura and Hatsugai 2011; van Doorn et al. 2011; Dickman et al. 2017). Therefore, there should be a distinct molecular mechanism of cytoplasm removal during bryophyte spermiogenesis. Since previous observation showed that autophagy is highly activated during spermiogenesis in *M. polymorpha* (Kreitner 1977b; Minamino et al. 2017), I hypothesized that autophagy could be involved in the cytoplasm removal during spermiogenesis in *M. polymorpha*. To verify this hypothesis, I attempted to investigate the role of autophagy in organelle reorganization during spermiogenesis.

Autophagy is a well conserved system in eukaryotes for degradation of cytoplasmic components in the vacuole/lysosome. As shown in **Figure 20**, in macroautophagy (referred to simply as autophagy hereafter), the isolation membrane or the phagophore extends engulfing cytoplasmic components to form the double-membraned structure

autophagosome. The outer membrane of the autophagosome fuses with the vacuolar membrane, releasing the single-membraned structure autophagic body into the vacuole to be degraded by vacuolar enzymes (Takeshige et al. 1992; Baba et al. 1994; Zhao and Zhang 2019). In early autophagy studies, it was believed that autophagy is involved in bulk degradation of cytoplasmic components in response to nutrient starvation. However, now autophagy is shown to be also required for selective degradation of various cytoplasmic components including damaged or excess organelles (Gatica et al. 2018; Johansen and Lamark 2020). In the 1990s, autophagy-related (*ATG*) genes required for autophagosome formation were identified by forward genetic studies in *S. cerevisiae* (Tsukada and Ohsumi 1993; Thumm et al. 1994; Klionsky et al. 2003). Atg and Atg-related proteins involved in autophagosome formation compose several functional units: the Atg1 complex, the phosphatidylinositol 3-kinase (PI3K) complex, Atg9, the Atg2-Atg18 complex, and the lipidation system complex (Mizushima et al. 2011; **Figure 21A**). Roles of these complexes and the molecular mechanisms governing autophagosome formation have been extensively studied thus far (Nakatogawa et al. 2020; **Figure 21B**). Reverse genetic approaches have also unraveled physiological roles of autophagy in a wide range of biological functions, including metabolic adaptation, intracellular quality control, and development using various organisms (Mizushima and Komatsu 2011; Marshall and Vierstra 2018).

Recent studies also demonstrated that autophagy is required for spermiogenesis (reviewed by Norizuki et al. [2020]). In mice, *atg* spermatozoa exhibits abnormalities such as defects in acrosome biogenesis, reorganization of cytoskeletons, rearrangement of mitochondria and the nucleus (Wang et al. 2014; Shang et al. 2016; Huang et al. 2020). Despite multiple defects in *atg* spermatozoa, cytoplasm removal is not severely affected,

suggesting that autophagy has minor roles in cytoplasm removal, probably because that is fulfilled by phagocytosis by Sertoli cells (Wang et al. 2014; Shang et al. 2016; Huang et al. 2020). In the moss *Physcomitrium patens*, autophagy is also required for differentiation of spermatozoids; the *atg* spermatozoid is not fertile and possess an abundant amount of the cytoplasm (Sanchez-Vera et al. 2017). However, detailed observation of organelles during spermiogenesis is not performed in this past study, and it remains largely unknown in which processes of spermiogenesis autophagy is required.

Here I generated autophagy-defective mutants (Mp*atg* mutants) and performed detailed observation of organelle dynamics in Mp*atg* mutants. My results demonstrated that autophagy is required for degradation of various organelles in the vacuole during spermiogenesis, and mitochondria are degraded by autophagy at a different stage of spermiogenesis from other organelles. Furthermore, I also discovered that some organelle proteins are transported into the vacuole in an autophagy-independent manner. These results indicated that each cytoplasmic component is removed in a distinct cell-autonomous manner during spermiogenesis in *M. polymorpha*, also highlighting a divergent mechanism for cytoplasm removal during spermiogenesis between plants and animals.

RESULTS

Identification of MpATG genes

To investigate the role of autophagy during spermiogenesis, the autophagosome marker and autophagy-defective mutants are useful. Since molecular analyses of autophagy have not been performed in *M. polymorpha* thus far, I firstly identified homologs of core *ATG* genes in *M. polymorpha*. For identification of Mp*ATG* genes, *ATG* genes in *S. cerevisiae* and *A. thaliana* were used as a query. Although ATG11 is not required for bulk autophagy in *S. cerevisiae* and the homolog of *ATG101* is not detected in the *S. cerevisiae* genome, ATG11 and ATG101 in *A. thaliana* form the ATG1 complex, and ATG11 is required for starvation-induced autophagy (Kim et al. 2001; Hosokawa et al. 2009; Li et al. 2014). Therefore, *ATG11* and *ATG101* were included in my analysis. As shown in **Table 6**, *M. polymorpha* possess all core *ATG* genes conserved in *A. thaliana* with low genetic redundancy. Homologs of *ATG29* and *ATG31* were not identified in *A. thaliana* and *M. polymorpha* under my analytical condition.

Establishment of the autophagosome marker in M. polymorpha

In various organisms, ATG8 is widely used as the autophagosome marker, because ATG8 is localized on the isolation membrane, the autophagosome, and the autophagic body (Kirisako et al. 1999; Kabeya et al. 2000; Yoshimoto et al. 2004; Izumi et al. 2015). Therefore, I generated transgenic plants expressing mCitrine-MpATG8a and observed its subcellular localization. Under the normal growth condition, mCitrine-MpATG8a was observed as small puncta, which might represent autophagosome-related structures. mCitrine-MpATG8a was also localized in the nucleus (**Figure 22A**). Nuclear localization of ATG8 is also reported in mammals (Huang et al. 2015). If small puncta on which

mCitrine-MpATG8a is localized are the isolation membrane or the autophagosome, mCitrine-MpATG8a should be also localized on the autophagic body. Since autophagic bodies are quickly degraded by vacuolar enzymes, I treated the mCitrine-MpATG8a plant with Concanamycin A, which inhibits acidification of the vacuole and inactivates vacuolar enzymes (Yoshimoto et al. 2004). Only under treatment with Concanamycin A, I observed autophagic body-like structures in the vacuole (**Figure 22B**). These localization patterns are similar to those reported in *A. thaliana* (Yoshimoto et al. 2004), suggesting that mCitrine-MpATG8a could be used as the autophagosome marker.

Generation of Mpatg mutants

Next, I generated autophagy-defective mutants by genome editing using the CRISPR/Cas9 system (Sugano et al. 2014; Sugano et al. 2018). First, I attempted to generate the Mp*atg5* mutant. ATG5 is required for conjugation of ATG8 to phosphatidylethanolamine, and *atg5* mutants in various organisms are defective in autophagy (Tsukada and Ohsumi 1993; Mizushima et al. 2001; Kuma et al. 2004; Thompson et al. 2005; Hanada et al. 2007). I obtained two alleles of Mp*atg5* mutants, referred to as Mp*atg5-1*^{ge} and Mp*atg5-2*^{ge}, with frame shift mutations (**Figure 23**). If the Mp*atg5* mutant is defective in autophagy, mCitrine-MpATG8a should not be transported into the vacuole. I observed subcellular localization of mCitrine-MpATG8a in Mp*atg5-1*^{ge}. While mCitine-MpATG8a was also observed as small puncta in Mp*atg5-1*^{ge} like the wild type, autophagic body-like structures were not observed in Mp*atg5-1*^{ge} (**Figures 24A and B**). I also attempted to check the vacuolar transport of mCitrine-MpATG8a by western blotting. Since ATG8 is rapidly degraded in the vacuole, whereas fluorescent proteins are more stable to vacuolar enzymes, the transport of mCitrine-MpATG8 to the

vacuole can be monitored by examining the accumulation of free mCitrine by immunoblotting (Shintani and Klionsky 2004; Chung et al. 2010). In the wild type, two bands were observed via immunoblotting using an anti-GFP antibody, at approximately 43 and 27 kDa. The 43 kDa band represented full-length mCitrine-MpATG8a, and the 27 kDa product represented free mCitrine. In contrast, only the 43 kDa product was detected in Mp*atg5-1*^{ge} (**Figure 24C**). These data indicated that small puncta of mCitrine-MpATG8a in Mp*atg5-1*^{ge} could be not the autophagosome, but aberrant structures which cannot be transported into the vacuole. These aberrant structures are also observed in various *atg* mutants of *A. thaliana* (Yoshimoto et al. 2004; Kang et al. 2018). Therefore, Mp*atg5-1*^{ge} could be defective in autophagy.

I also generated mutants of other *ATG* genes. Mp*ATG2*, Mp*ATG7*, Mp*ATG13*, and Mp*ATG14* were used as targets. *atg2*, *atg7*, *atg13a/atg13b*, and *atg14a/atg14b* mutants of *A. thaliana* exhibit severe defects in autophagy (Doelling et al. 2002; Inoue et al. 2006; Suttangkakul et al. 2011; Liu et al. 2020). I obtained these mutants by similar methods in the Mp*atg5* mutant (**Figures 25 to 28**). I also checked whether these mutants are defective in autophagy by cleavage assay of mCitrine-MpATG8a. Like Mp*atg5-1*^{ge}, in Mp*atg2-1*^{ge}, Mp*atg7-1*^{ge}, Mp*atg14-1*^{ge}, and Mp*atg14-2*^{ge}, only the 43 kDa product was detected, confirming that these mutants are defective in autophagy (**Figures 29A and C**). Meanwhile, in the Mp*atg13-1*^{ge} and Mp*atg13-2*^{ge}, the faint signal of the 27 kDa band was detected (**Figure 29B**), suggesting that Mp*atg13* mutants could possess weak activity of autophagy compared with other Mp*atg* mutants, consistent with the phenotypes of *atg13a/atg13b* mutants of *A. thaliana* (Huang et al. 2019).

Mpatg mutants exhibit chlorosis and higher sensitivity to nutrient starvation

Before analyzing the role of autophagy during spermiogenesis, I observed phenotypes in vegetative growth of Mp*atg* mutants. Under the normal growth condition, Mp*atg* mutants except for Mp*atg13* mutants exhibited a yellowish chlorotic phenotype at the central part of their thalli (**Figure 30**), similar to *atg* mutants of *A. thaliana* (Doelling et al. 2002; Hanaoka et al. 2002). Mp*atg13* mutants did not exhibit this phenotype under the same condition, probably because autophagy might occur to some extent in these mutants (**Figures 29B and 30B**). These data suggested that autophagy is required for preventing chlorosis in *M. polymorpha*.

One of the best characterized roles of autophagy in land plants is adaptation to nutrient starvation (Masclaux-Daubresse et al. 2017; Marshall and Vierstra 2018). I also investigated whether Mp*atg* mutants are sensitive to nutrient starvation. As shown in **Figure 31**, Mp*atg* mutants except for Mp*atg13* mutants exhibited higher sensitivity to nutrient starvation. I did not find any significant differences between the wild type and Mp*atg13* mutants, which possess some activity of autophagy (**Figures 29B and 31B**). These results indicated that autophagy is also required for adaptation to nutrient starvation in *M. polymorpha*.

Autophagy is required for organelle reorganization during spermiogenesis in M. polymorpha

I examined whether autophagy is also required for formation of spermatozoids. Wild-type spermatozoids possessed little amount of the cytoplasm. Conversely, Mp*atg5* spermatozoids harbored an abundant cytoplasm and exhibited defective motility (**Figures 32 and 33**). Introduction of CRISPR/Cas9-resistant Mp*ATG5* (Mp*ATG5*^{res}) rescued the defects in spermiogenesis in Mp*atg5-1*^{ge}, suggesting that these defects result from the loss

of function of MpATG5 (**Figure 32**). Other Mp*atg* mutants also exhibited similar phenotypes to the Mp*atg5* mutant (**Figure 32**). Mp*atg2* spermatozoids were not yielded, which was consistent with the severer chlorosis phenotype of Mp*atg2* compared with other Mp*atg* mutants. Crossing of male Mp*atg* mutants with wild-type females yielded no sporangia (**Figure 34**), suggesting male sterility of Mp*atg* mutants. These results suggested that autophagy is indispensable for formation of functional spermatozoids. Intriguingly, while Mp*atg13* mutants did not exhibit chlorosis and elevated sensitivity to nutrient starvation, Mp*atg13* spermatozoids exhibited a similar phenotype to other Mp*atg* mutants, suggesting that MpATG13-dependent autophagic activity is critical for spermiogenesis (**Figures 29B, 30B, 31B, and 32**). This result also indicated that defective spermiogenesis does not result from chlorosis of thalli. Thus, autophagy is required for cytoplasm removal during spermiogenesis, which is essential for generating functional spermatozoids.

To reveal which process of organelle reorganization requires autophagy during spermiogenesis, I then observed each organelle in Mp*atg* mutant spermatids undergoing spermiogenesis. TEM observation of Mp*atg5* spermatozoids was not successful, because spermatozoids of Mp*atg5* was rarely obtained from antheridiophores of the mutant and I could not collect a sufficient amount of Mp*atg5* spermatozoids for TEM observation. Hence, I performed TEM observation using antheridial cells undergoing spermiogenesis, and also conducted observation of organelles in spermatozoids expressing organelle markers by confocal microscopy.

For the shape of the nucleus, the wild-type spermatozoid possessed a highly elongated helical nucleus. Conversely, the Mp*atg5* spermatozoid possessed a nucleus with abnormal morphology (**Figure 35**). 7.7% of Mp*atg5* spermatozoids possessed a nucleus similar to

that observed in Stage 4 of the wild-type spermiogenesis (**Figure 2 in Chapter 1**), and 52.3% of Mp*atg5* spermatozoids harbored an abnormally shaped nucleus with protrusions (n = 65 spermatozoids). Among the nuclei with protrusions, nuclei with hollows that were not stained by Hoechst were also observed. The rest population of spermatozoids harbored an amorphous shape of nucleus (**Figure 35**). These results suggested that autophagy is somehow involved in nuclear shaping during spermiogenesis in *M. polymorpha*.

Next, I examined mitochondria. Wild-type spermatozoids possessed two mitochondria: one anterior and one posterior mitochondria. Intriguingly, Mp*atg5-1*^{ge} possessed more fragmented mitochondria in the cell body (**Figure 36A**). These fragmented mitochondria were also observed in other Mp*atg* mutants (**Figure 36A**). As shown in **Figure 4 in Chapter 1**, highly elongated mitochondria were observed in wild-type antheridium cells at Stage 0 and 1. To investigate whether Mp*atg* mutants exhibited defects in formation of elongated mitochondria, I observed mitochondria in Mp*atg5-1*^{ge} antheridium cells at Stage 0 and 1. At these stages, I did not find any marked difference in mitochondria distribution between wild-type and Mp*atg5-1*^{ge} spermatids, suggesting that the defect in mitochondria reorganization would appear after Stage 1 in Mp*atg5-1*^{ge} (**Figure 4 in Chapter 1 and Figure 36B**). I also performed TEM observation of mitochondria in spermatids. In wild-type and Mp*atg5-1*^{ge} spermatids, the anterior mitochondrion was associated with the MLS. However, in Mp*atg5-1*^{ge} spermatids, more mitochondria were observed near the anterior mitochondrion, confirming that Mp*atg5-1*^{ge} spermatids possess more mitochondria than wild-type spermatids (**Figures 36C and D**). These results indicated that autophagy is required for removal of mitochondria during spermiogenesis in *M. polymorpha*.

Next, I observed the plastid. Wild-type spermatozoids possessed one cylindrical plastid. However, in Mp*atg5-1*^{ge} spermatozoids, one round plastid was observed, suggesting that autophagy could be involved in shaping the plastid, but not the regulation of its number (**Figure 37A**).

I then observed peroxisomes. Signal from a peroxisome marker, Citrine-PTS1, was not detected in wild-type spermatozoids. Conversely, Citrine-PTS1 was observed as multiple puncta in Mp*atg5-1*^{ge} spermatozoids, suggesting that autophagy is involved in removal of peroxisomes (**Figure 37B**).

Next, I examined ER markers. As shown in **Figure 6A in Chapter 1**, SP-mCitrine-HDEL was observed as puncta at the anterior and posterior regions of wild-type spermatozoids. However, in Mp*atg5-1*^{ge} spermatozoids, this ER marker was observed accumulating in the cytosol, suggesting that this protein is degraded by autophagy (**Figure 37C**). Furthermore, signals from mCitrine-MpSEC20 and mCitrine-MpSEC22 were also observed in the cytoplasm of Mp*atg5-1*^{ge} spermatozoids, although their intensities were not so high, whereas these markers were not detected in wild-type spermatids (**Figure 37C**). Thus, autophagy is responsible for removal of the ER from the cytoplasm during spermiogenesis, at least partly. Intriguingly, signals from these ER markers were not detected at the nuclear envelop of Mp*atg5-1*^{ge} spermatozoids. This could imply that reorganization of the nuclear envelop takes place in an MpATG5-independent manner (**Figure 37C**).

Next, I observed the Golgi apparatus. In wild-type spermatozoids, signals from all Golgi markers used in this study were not detected. Although the signal from mCitrine-MpGOS11 was not detected in Mp*atg5-1*^{ge} spermatozoids, ST-Venus was observed as a large structure, which was similar to the structure observed at Stage 1 and 2 in wild-type

spermatids (**Figure 7 in Chapter 1 and Figure 38A**). For mCitrine-MpSFT1, faint signal was detected only in a limited proportion of spermatozoids of Mp*atg5-1*^{ge}, although most spermatozoids did not possess this signal (**Figure 38A**). These results suggested that some Golgi structures/proteins are degraded by autophagy, and another part of Golgi structures/proteins are removed independent of MpATG5. Intriguingly, I found that the curved Golgi apparatus engulfing the cytosol to form a vesicle-like structure was observed in spermatozoids of Mp*atg5-1*^{ge} (**Figure 38B**). A similar structure is observed in *atg* mutants of *S. cerevisiae* and mammals (Nishida et al. 2009; Yamaguchi et al. 2016). The curved Golgi apparatus generates a double-membraned structure, which is distinct from the canonical autophagosome, and is required for degradation of cytoplasmic components such as mitochondria in the vacuole/lysosome in some *atg* mutants of *S. cerevisiae* and mammals (Nishida et al. 2009; Yamaguchi et al. 2016). I also found the double-membraned structures in Mp*atg5-1*^{ge} spermatids, which could reflect that a similar mechanism also operates in *M. polymorpha*, although the possibility that canonical autophagosomes were formed in Mp*atg5-1*^{ge} spermatids was not excluded (**Figure 38C**).

I then observed plastid DNA in the Mp*atg5-1*^{ge} spermatid. In another liverwort *Dumortiera hirsuta* and the hornwort *Anthoceros punctatus*, the loss of plastid DNA is reported to occur during spermiogenesis (Izumi and Ono 1999; Shimamura et al. 1999). To visualize plastid DNA in spermatids, I used the anti-dsDNA antibody as shown in **Figure 11 in Chapter 1**. In wild-type spermatids, plastid DNA was detected in Stage 2, but not in Stage 4 (**Figure 39**). The loss of plastid DNA was also observed in Mp*atg5-1*^{ge} spermatids (**Figure 39**). These data suggested that the loss of plastid DNA occurs during spermiogenesis in an MpATG5-independent manner.

Microtubule organization in the Mpatg5 mutant

As shown in **Figure 33**, spermatozoids of Mp*atg5-1*^{ge} exhibited abnormal motility. In mice and *P. patens*, abnormal microtubule structures including aberrant axonemal 9 + 2 structures of flagella are observed in *atg* mutants (Wang et al. 2014; Shang et al. 2016; Sancehz-Vera et al. 2017). Therefore, I examined whether the Mp*atg5-1*^{ge} mutant was defective in organization of microtubules during spermiogenesis. Distinct from mice and *P. patens*, I did not find any marked defects in the 9 + 2 structure of flagella in Mp*atg5-1*^{ge} (**Figure 40A**). I also found that the spline was normally formed in Mp*atg5-1*^{ge} by immunostaining of tubulin using an anti-α-Tubulin antibody (**Figure 40B**). These results suggested that autophagy regulates spermiogenesis in *M. polymorpha* in a different manner from mice and *P. patens*.

Generation of the Mpatg5 mutant without the T-DNA cassette

As shown above, Mp*atg* mutants exhibited defects in organelle reorganization during spermiogenesis. I then attempted to investigate how autophagy regulates spermiogenesis. Since autophagy is a degradation system in the vacuole, various organelles should be degraded in the vacuole by autophagy. To detect transport of organelles into the vacuole, I performed dual-color imaging of the vacuolar membrane and other organelles. To generate transgenic plants expressing a vacuolar membrane marker and another organelle marker, two transgenes harboring constructs of organelle markers must be inserted into the genome of *M. polymorpha*. Although four selection markers usable in transformation are established (Ishizaki et al. 2015), only hygromycin and chlorsulfuron worked for efficient thallus transformation under my experimental condition. Mp*atg5-1*^{ge} already harbored one T-DNA fragment containing the hygromycin-resistant gene *HYGROMYCIN*

PHOSPHOTRANSFERASE (*HPT*) and the *Cas9* gene, which was inserted when the mutant was generated (**Figure 41A**). To introduce two additional transgenes to the Mp*atg5-1*^{ge} mutant, I attempted to generate the Mp*atg5* mutant without a T-DNA insertion (**Figure 41B**). As the Mp*atg5* mutant was sterile (**Figure 34**), the complemented line of Mp*atg5-1*^{ge} was used for this purpose. However, F1 male progenies that possess the Mp*atg5-1*^{ge} mutation but not the T-DNA insertion were not recovered by genotyping 62 F1 progenies, probably because of linkage between the mutation and T-DNA. Meanwhile, when the complemented Mp*atg5-2*^{ge} was crossed with wild-type female line, F1 male progenies which possess the Mp*atg5-2*^{ge} mutation but not the T-DNA insertion (hereafter referred to as Mp*atg5-2*$^{ge/cf}$) was easily recovered. Recently, I succeeded in obtaining one F1 male progeny, which possesses the Mp*atg5-1*^{ge} mutation but not the T-DNA insertion (hereafter referred to as Mp*atg5-1*$^{ge/cf}$), after genotyping 203 F1 progenies. Mp*atg5-1*$^{ge/cf}$ and Mp*atg5-2*$^{ge/cf}$ spermatozoids exhibited the same phenotype as the Mp*atg* mutants, and introduction of Mp*ATG5-mCitrine* rescued these defects (**Figure 41C**). I performed further analyses using Mp*atg5-2*$^{ge/cf}$.

Various organelle marker proteins are transported into the vacuole by autophagy

If autophagy is required for degradation of some organelles during spermiogenesis, marker proteins for such organelles should be also transported into the vacuole by autophagy. Minamino et al. (2017) observed that some organelle marker proteins are transported into the spherical structures, most likely vacuoles, during spermiogenesis in hand-sectioned antheridia. To check whether organelle markers are indeed transported into the vacuole, I attempted dual-color observation of organelle markers with mCitrine- or mGFP-tagged MpVAMP71, which is localized to the vacuole membrane in thallus and

spermatid cells (Kanazawa et al. 2016; Minamino et al. 2017).

First, I observed localization of MpATG8a. Consistent with the results in thallus cells, mTurquoise2-MpATG8a is transported into the vacuole in an MpATG5-dependent manner; we did not detect accumulation of mTurquoise2 in the vacuole in Mp*atg5-2*$^{ge/cf}$ (**Figures 24 and 42A**). This result is not due to the complete block of vacuolar transport pathways including the endocytic pathway in the Mp*atg5* mutant, because mCitrine-MpSYP12A, a fluorescently tagged Qa-SNARE localizing to the plasma membrane (Kanazawa et al. 2016), was transported into the vacuole in the Mp*atg5-2*$^{ge/cf}$ mutant (**Figure 42B**), also confirming that MpSYP12A is transported to the vacuole independent of autophagy.

Next, I investigated whether other organelle marker proteins were transported into the vacuole in the Mp*atg5-2*$^{ge/cf}$ mutant. The mitochondria, peroxisome, and plastid marker proteins were not transported into the vacuole in the Mp*atg5-2*$^{ge/cf}$ mutant, indicating that these organelles are degraded by autophagy during spermiogenesis (**Figure 43**). Intriguingly, behavior of ER markers was different between the soluble and membrane protein markers (**Figure 44**). While the soluble ER protein marker SP-mTurquoise2-HDEL was transported into the vacuole both in the wild type and the Mp*atg5-2*$^{ge/cf}$ mutant, the ER membrane protein markers mCitrine-MpSEC20 and mCitrine-MpSEC22 were transported into the vacuole in an MpATG5-dependent manner (**Figure 44**). This result suggested that at least subpopulation of ER proteins/structures are degraded by autophagy. Regarding the Golgi apparatus, all Golgi marker proteins I examined were transported into the vacuole both in the wild type and the Mp*atg5-2*$^{ge/cf}$ mutant, suggesting that the Golgi proteins and/or structures are transported into the vacuole in an MpATG5-independent manner, at least partly (**Figure 45**). Thus, autophagy distinctly contributes

to degradation of organelles during spermiogenesis: mitochondria, peroxisomes, plastids, and subpopulation of the ER are degraded by autophagy, whereas other vacuolar degradation systems such as endocytic degradation also contribute to degradation of organelles during spermiogenesis (**Table 7**).

Mitochondrial degradation by autophagy precedes autophagic degradation of other organelles

Previous TEM observation in *M. polymorpha* revealed autophagosomes containing the cytosol including ribosomes are observed during spermiogenesis, however, autophagosomes containing membrane-bounded organelles have not directly observed thus far (Kreitner 1977b; Minamino et al. 2017). In my TEM observation, I found the forming autophagosome, which seemed to be selectively engulfing a mitochondrion (**Figure 46A**). I also found the autophagosome containing a mitochondrion almost exclusively (**Figure 46A**). These morphological features of autophagy were similar to those observed in selective autophagic degradation of mitochondria in non-plant systems (Kanki et al. 2009). Thus, my results would suggest that mitochondria are selectively degraded by autophagy during spermiogenesis.

I also tried to observe autophagic degradation of mitochondria by immunostaining using the autophagosome marker HA-MpATG8a. At Stage 2, HA-MpATG8a was observed as a few puncta in the cytoplasm, some of which were colocalized with mitochondria (**Figure 46B**). However, at Stage 4, at which removal of mitochondria is mostly completed, HA-MpATG8a was localized as many punctate and/or large structures, which were not colocalized with mitochondria (**Figure 4 in Chapter 1 and Figure 46B**). At this stage, the MpATG8a-positive structures should be involved in degradation of

peroxisomes and the cytosol, because these cytoplasmic components were removed during Stage 4 to 5 (**Figures 2 and 8 in Chapter 1**). These results indicated that autophagic degradation of mitochondria could occur in advance the degradation of other cytoplasmic components, indicating distinct regulation of organelle remodeling depending each cellular component (**Figure 47**).

DISCUSSION

Autophagy is required for cytoplasm removal during spermiogenesis in M. polymorpha

In this chapter, I demonstrated that autophagy plays pivotal roles in degradation of various organelles during spermiogenesis. This finding demonstrated that spermiogenesis in *M. polymorpha* is accomplished through the cell-autonomous degradation of unneeded cytoplasmic components. It should be noted that metazoan spermiogenesis is accomplished in totally distinct manners. In mammals, unnecessary and excess cytoplasmic components are segregated as residual bodies, which are removed by the phagocytic activity of neighboring cells (Smith and Lacy 1959; Dietert 1966; O'Donnell et al. 2011; **Figure 19**). Also, during *Caenorhabditis elegans* spermiogenesis, the cytoplasm is eliminated through a similar degradation system (L'Hernault, 2006; Huang et al., 2012). In *Drosophila melanogaster*, the individualization complex progressively translocates from the head to the tail of transforming spermatids, stripping away unneeded cytoplasmic components from elongated spermatids to form the cystic bulge. At the last step of spermiogenesis, the cystic bulge containing unneeded cytoplasmic components are excluded from spermatozoa as the waste bag (Tokuyasu et al. 1972; Fabian and Brill 2012). Although the role of autophagy in spermiogenesis in *C. elegans* and *D. melanogaster* remains unknown, autophagy is required for distinct processes than cytoplasm removal in mice, suggesting that cytoplasm removal is mostly fulfilled by cell-non-autonomous degradation systems at least in mice (Wang et al. 2014; Shang et al. 2016; Huang et al. 2020). In contrast to these species, cytoplasm removal in *M. polymorpha* should be fulfilled in a cell-autonomous way, because plant cells are surrounded by the rigid cell wall and phagocytic activity was secondarily lost in the plant lineage during evolution (Dacks and Field 2007; Hara-Nishimura and Hatsugai 2011; van

Doorn et al. 2011; Dickman et al. 2017), thus phagocytic removal of the unneeded cytoplasm cannot occur during spermiogenesis in plants. In the moss *P. patens*, autophagy is also required for cytoplasm removal during spermiogenesis, suggesting that bryophytes adopt similar strategies for cytoplasm removal (Sanchez-Vera et al. 2017).

In mammals, the amount of remained cytoplasm is reported to correlate with the function of spermatozoa such as their motility (Gomez et al., 1996; Keating et al., 1997; Rengan et al., 2012). Consistent to this, Mp*atg* spermatozoids exhibited defective motility and sterility (**Figures 33 and 34**), suggesting that cytoplasm removal is required for the function of spermatozoids also in *M. polymorpha*. However, the green alga *Nephroselmis olivacea*, which harbors flagella with similar motility to that of *M. polymorpha*, contains abundant cytoplasm (Inouye and Hori 1991; Miyamura et al. 2002). Further analyses are needed to reveal the relationship between cytoplasm removal during spermiogenesis and the function of spermatozoids in *M. polymorpha*.

Mitochondria are selectively degraded by autophagy during spermiogenesis

As shown in **Chapter 1**, I found that the shape and size of mitochondria drastically change during spermiogenesis in *M. polymorpha*, and mitochondrial fission is important for this process. In this chapter, I also revealed that mitochondria are selectively degraded by autophagy. Also, in *S. cerevisiae* and mammals, mitochondrial fission is involved in mitochondrial degradation, and fragmented mitochondria are the target of autophagy (Twig et al. 2008; Rambold et al. 2011; Mao et al. 2013; Yamashita et al. 2016). During an early stage of spermiogenesis, mitochondria undergo constant fission and are degraded by autophagy in *M. polymorpha* (**Figure 9 in Chapter 1 and Figure 46**). Furthermore, fragmented mitochondria accumulated in the cytosol of spermatozoids in Mp*atg* mutants

(**Figure 36**). Therefore, fragmented mitochondria could be the target of autophagy during spermiogenesis in *M. polymorpha*. However, it remained unknown whether MpDRP3 is involved in degradation of mitochondria by autophagy, because expression of a dominant negative form of MpDRP3 did not result in accumulation of mitochondria (**Figure 15 in Chapter 1**). Further studies are needed to unveil the relationship between fission and degradation of mitochondria.

One interesting question is how mitochondria to be degraded are determined. Spermatozoids of *M. polymorpha* possess two mitochondria, the anterior and posterior mitochondria, which must be escaped from degradation by autophagy. Although the molecular mechanism of protection from the degradation remains unknown, the MLS might be involved in this process, because the mitochondrion was associated with the MLS at the mono-mitochondrion stage during spermiogenesis (**Figure 4 in Chapter 1**). Although previous TEM observation revealed the morphological process of the MLS formation, the functions and components of the MLS have remained largely unknown. Functional analyses of the MLS would reveal how the anterior mitochondrion is escaped from degradation by autophagy.

Distinct mechanisms of organelle degradation during spermiogenesis

My study demonstrated that autophagy is involved in degradation of various organelles. Furthermore, my results suggested that all organelles are not degraded by bulk autophagy. I concluded that mitochondria are degraded in a unique mechanism from three reasons. First, TEM observation showed that mitochondria are selectively engulfed by the autophagosome (**Figure 46A**). Second, degradation of mitochondria takes place before Stage 3, peroxisomes and most of the cytosol are degraded by autophagy during Stage 4

to 5 (**Figures 2, 4, and 8 in Chapter 1 and Figure 46B**). Third, the autophagic activity is more prominent at Stage 4 than the stage in which mitochondria are degraded (**Figure 46B**). These results strongly suggest existence of distinct degradation systems responsible for distinctive organelles during spermiogenesis (**Figure 47**).

Then, the next interesting question is what determines the target of autophagy at each stage. One possibility is that autophagy receptors could be distinctly targeted to organelles to be degraded at distinct timing. Various autophagy receptors required for recognition of targets of selective autophagy have been identified in *S. cerevisiae* and mammals thus far (Johansen and Lamark 2020). However, homologs of most of those receptors are not conserved in plants including *A. thaliana* and *M. polymorpha* (Stephani and Dagdas 2020). Although recent studies using *A. thaliana* are shedding light on selective autophagy in this plant, molecular mechanisms of selective autophagy are poorly understood yet (Marshall and Vierstra 2018; Stephani and Dagdas 2020). Since the autophagy receptors reported in various organisms thus far interact with ATG8 (Johansen and Lamark 2020), identification of MpATG8 interactors during spermiogenesis would be hopeful in understanding how autophagy regulates organelle reorganization during spermiogenesis. Although I demonstrated that various organelles are degraded in the vacuole by autophagy, it is not clear whether other organelles than mitochondria are degraded by bulk autophagy or selective autophagy. This is partly because autophagosome are quickly fused with the vacuole and autophagic bodies released into the vacuole are immediately degraded by vacuolar enzymes. Genetic or pharmacological inhibition of vacuolar transport of the autophagosome or degradation of the autophagic body in the vacuole would also be effective in investigating how each organelle is degraded by autophagy.

Autophagy-independent degradation also occurs during spermiogenesis

Intriguingly, some organelle marker proteins were transported into the vacuole in the Mp*atg5* mutant, suggesting that MpATG5-independent vacuolar transport also contributes to organelle reorganization during spermiogenesis. One of the vacuolar transport systems is endocytosis. Endocytosis plays pivotal roles in the regulation of distribution and turnover of various plasma membrane proteins (Paez Valencia et al. 2016). A fluorescently tagged plasma membrane SNARE protein, mCtrine-MpSYP12A, was transported into the vacuole in the Mp*atg5-2*$^{ge/cf}$ mutant (**Figure 42B**), confirming that MpSYP12A is transported to and degraded in the vacuole through the endocytic pathway as proposed previously (Minamino et al. 2017). How the soluble ER marker and the Golgi markers are transported into the vacuole in an MpATG5-independent manner is unclear at present. ST-Venus was remained in Mp*atg5* spermatozoids but not in wild-type spermatozoids, and more SP-mCitrine-HDEL signal was remained in Mp*atg5* spermatozoids than in wild-type spermatozoids, which suggests that at least some populations of these proteins are transported into the vacuole by autophagy (**Figures 37C, 38A, 44, and 45A**). However, this result would not necessarily indicate that some parts of the ER and Golgi apparatus are transported into the vacuole by autophagy, as some fluorescently tagged Golgi proteins are reported to be transported from the Golgi apparatus into the vacuole in an endosomal sorting complex required for transport (ESCRT)-dependent manner (Dobzinski et al. 2015). In *S. cerevisiae* and mammals, the Golgi membrane-associated degradation (GOMED) pathway that is independent of some core ATG proteins is also reported (Yamaguchi et al. 2016). Although existence of the GOMED pathway has not firmly demonstrated in plants, my result that the Golgi structure similar to the Golgi apparatus undergoing GOMED in *S. cerevisiae* and mammals was

observed in the Mp*atg5* spermatid suggests that the GOMED pathway might be also involved in spermiogenesis in *M. polymorpha* (**Figure 38**). Further studies will reveal how autophagy-independent degradation systems contribute to plant spermiogenesis.

Autophagy-independent cellular reorganization during spermiogenesis

Reorganization of several organelles/cellular structures during spermiogenesis took place normally in Mp*atg* mutants. I did not detect abnormal organization of the axoneme in flagella and the spline in the Mp*ATG5* mutant (**Figure 40**), although abnormalities in microtubule structures are reported in autophagy-defective mutants of mice and *P. patens* (Shang et al. 2016; Sanchez-Vera et al. 2017; Huang et al. 2020). This discrepancy may reflect diversified involvement of autophagy in cellular remodeling including microtubule organization during spermiogenesis in bryophytes.

The Mp*atg5* spermatozoid possessed one plastid like in the wild type, although it was abnormally shaped (**Figure 37A**). This would be consistent with the previous TEM result that the number of plastids is already one in spermatids before spermiogenesis in bryophytes (Renzaglia and Garbary 2001). However, the plastid marker was transported into the vacuole in an autophagy-dependent manner, which suggests that the piecemeal-type chloroplast autophagy (Izumi et al. 2019) occurs during spermiogenesis, although its biological significance remains unknown. It is less likely that the piecemeal-type chloroplast autophagy is responsible for the loss of plastid DNA during spermiogenesis, because the loss of plastid DNA was also observed in the Mp*atg5* spermatid (**Figure 39**).

The nuclear shaping during spermiogenesis was also partially affected in Mp*atg5* spermatozoids, although a low percentage of spermatozoids harbored the Stage 4-like nucleus. Curiously, the protrusion was observed in the nucleus of the Mp*atg5*

spermatozoid (**Figure 35**). Selective autophagy of a part of the nucleus has been reported in *S. cerevisiae* and mammals (Mochida et al. 2015; Papandreou et al. 2019), and my result could imply that a part of the nucleus is eliminated by autophagy during spermiogenesis in *M. polymorpha*. Therefore, autophagy might regulate the nuclear shaping via the autophagic degradation of a part of the nucleus such as the nucleolus. Further detailed observation of the nucleoplasm dynamics in the spermatid would be needed to verify this hypothesis.

TABLES

Table 6. The list of autophagy-related genes in *M. polymorpha*

Group	Gene	Gene ID
ATG1 complex	Mp*ATG1*	Mp3g05030
	Mp*ATG11*	Mp4g18080
	Mp*ATG13*	Mp7g03210
	Mp*ATG101*	Mp4g10990
PI3K complex	Mp*ATG6*	Mp6g21390
	Mp*ATG14*	Mp1g00090
	Mp*VPS15*	Mp1g27200
	Mp*VPS34*	Mp7g11730
ATG9	Mp*ATG9*	Mp1g27300
ATG2-ATG18 complex	Mp*ATG2*	Mp6g18570
	Mp*ATG18*	Mp1g16930
		Mp1g05420
		Mp5g05830
		Mp3g05770
Lipidation system	Mp*ATG3*	Mp7g11950
	Mp*ATG4*	Mp1g14510
	Mp*ATG5*	Mp1g12840
	Mp*ATG7*	Mp2g07850
	Mp*ATG8*	Mp1g21590
		Mp5g05930
	Mp*ATG10*	Mp1g25570
	Mp*ATG12*	Mp2g25440
	Mp*ATG16*	Mp7g17850

Homologs of *ATG* and *ATG*-related genes involved in autophagosome formation in *M. polymorpha*.

Table 7. The summary of Figure 42 to 45

Organelle	Marker protein	Transported into the vacuole in WT	Transported into the vacuole in Mp*atg5*
Mitochondrion	Mito-XFP	+	-
Peroxisome	XFP-PTS1	+	-
Plastid	MpPGM1-XFP	+	-
ER	XFP-MpSEC20	+	-
	XFP-MpSEC22	+	-
	SP-XFP-HDEL	+	+
Golgi	XFP-MpGOS11	+	+
	XFP-MpSFT1	+	+
	ST-XFP	+	+
PM	XFP-MpSYP12A	+	+

Summary of the transport of organelle marker proteins into the vacuole in the wild type (WT) and Mp*atg5-2*$^{ge/cf}$. XFP: fluorescent proteins including Citrine, mCitrine, and mTurquoise2. +: transported into the vacuole. -: not transported into the vacuole.

FIGURES

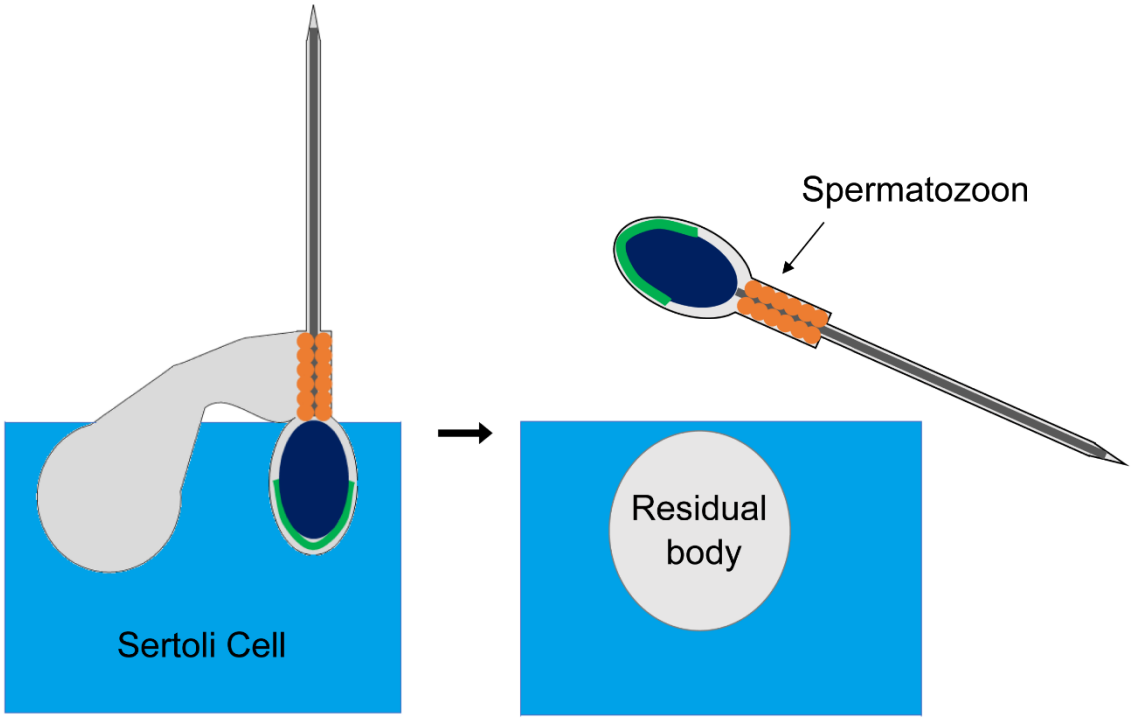

Figure 19. The schematic model of cytoplasm removal during mammalian spermiogenesis

Just before the release of spermatozoa, unnecessary cytoplasmic components are excluded from their cell bodies as the residual body, which is phagocytosed and degraded by the neiboring Sertoli cell. This figure is illustrated based on figures in O'Donnell et al. (2011).

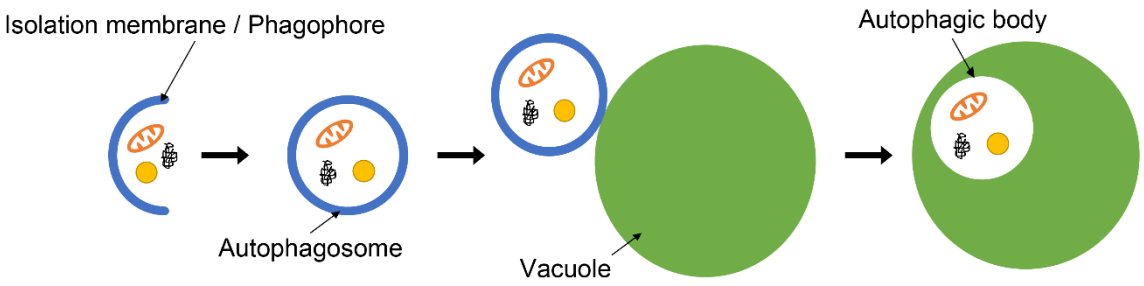

Figure 20. The schematic model of formation and vacuolar transport of the autophagosome

A

Group	Subunit							
Atg1 complex	Atg1	Atg13	Atg17	Atg29	Atg31			
PI3K complex	Atg6	Atg14	Vps34	Vps15				
Atg9	Atg9							
Atg2-Atg18 complex	Atg2	Atg18						
Lipidation system	Atg3	Atg4	Atg5	Atg7	Atg8	Atg10	Atg12	Atg16

B

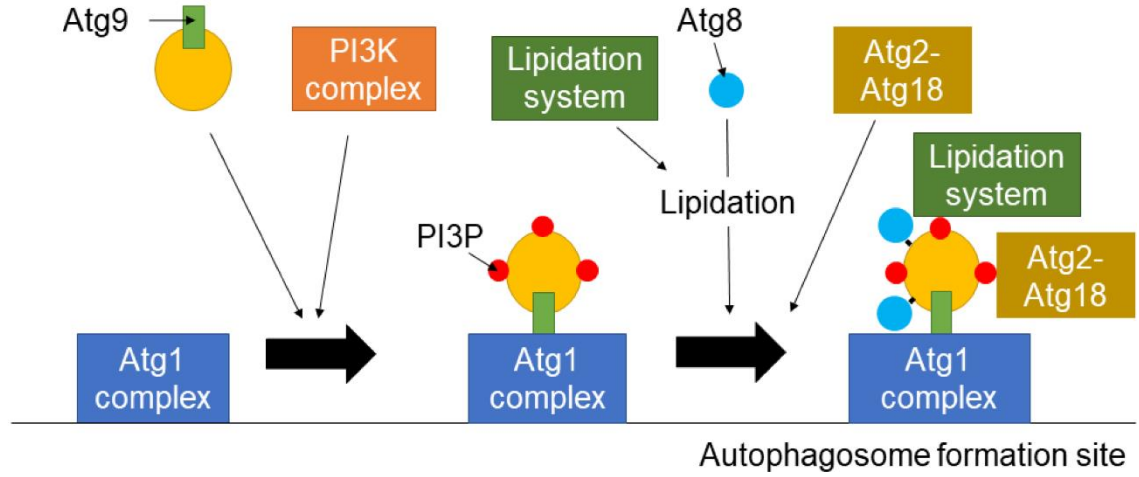

Figure 21. Roles of core Atg proteins in autophagosome formation

(**A**) Five functional groups of core Atg proteins in *S. cerevisiae*. (**B**) A schematic model of core Atg functions. First, the Atg1 complex is recruited to the autophagosome formation site. The Atg1 complex recruits Atg9 vesicles and the PI3K complex, and phosphatidylinositol 3-phosphate (PI3P) is generated. Then the Atg2-18 complex and Atg proteins involved in lipidation are recruited at this site. Atg8 is conjugated to phosphatidylethanolamine by the lipidation system and localized and anchored to the membrane (Nakatogawa 2020).

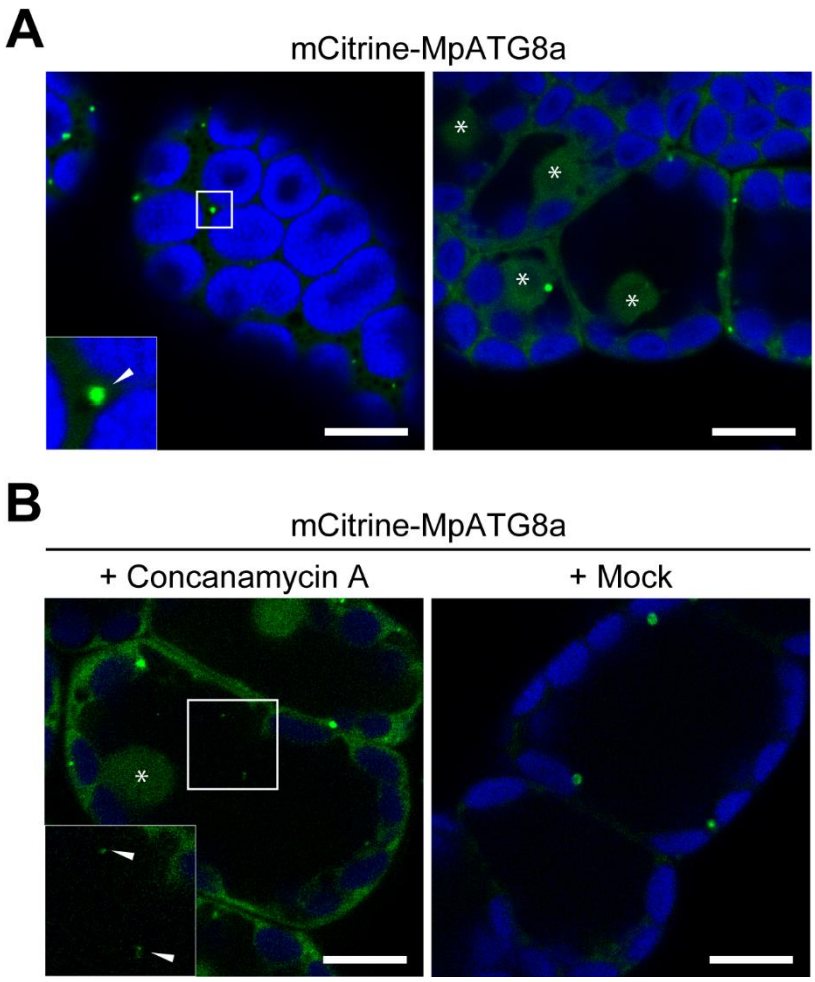

Figure 22. Subcellular localization of mCitrine-MpATG8a in thallus cells

(**A**) Subcellular localization of mCitrine-MpATG8a in thallus cells under the normal growth condition. (**B**) Localization of mCitrine-MpATG8a in thallus cells treated with Concanamycin A. The insets are magnified images of the boxed regions. The green and blue colors indicate fluorescence from mCitrine and autofluorescence of chlorophyll, respectively. Bars = 10 μm.

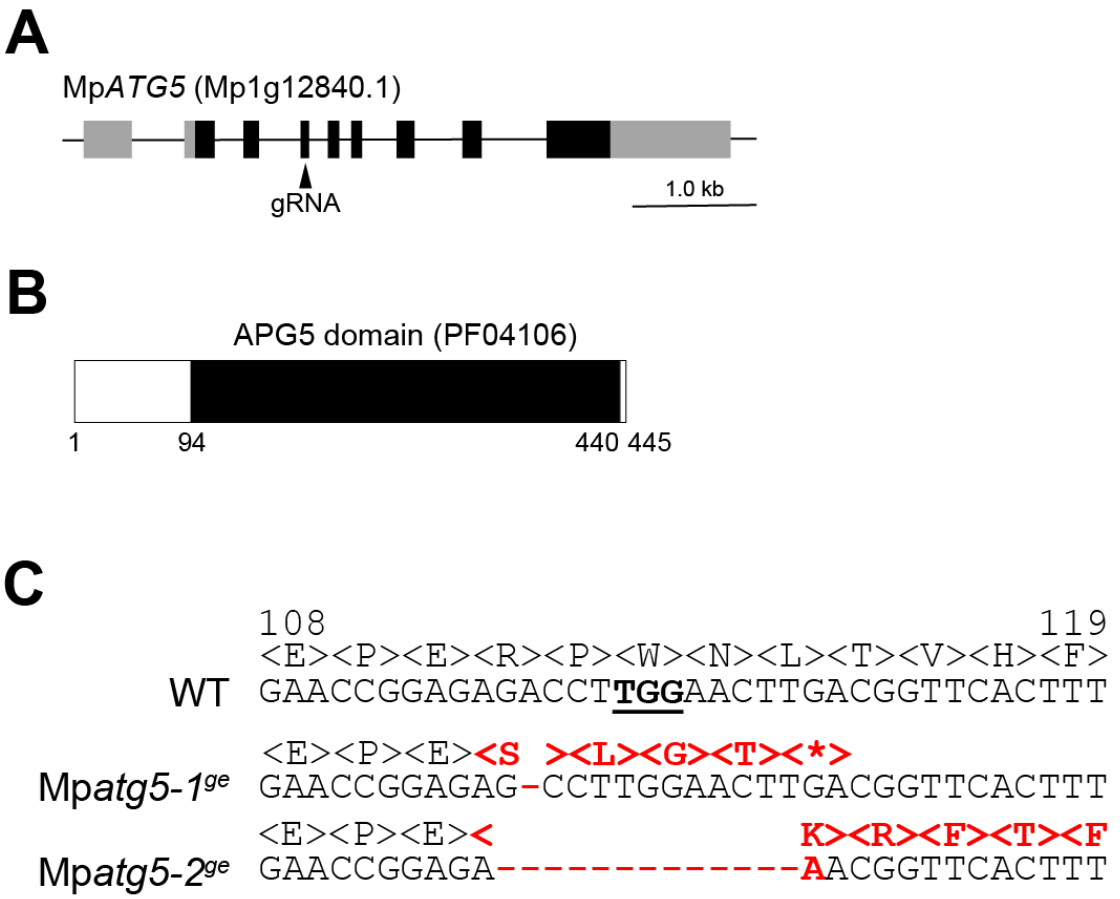

Figure 23. Generation of Mp*atg5* mutants

(**A**) The gene body of Mp*ATG5*. The black and gray colors indicate the CDS and UTR of Mp*ATG5*, respectively. gRNA: guide RNA used for generation of the Mp*atg5* mutants. (**B**) The domain structure of MpATG5. (**C**) Sequences of the mutations in Mp*ATG5* introduced by genome editing. All two mutations result in frame shifts. The underline indicates the protospacer adjacent motif (PAM) sequence. Deleted and substituted bases and substituted amino acid residues are shown in red. The asterisk indicates the stop codon.

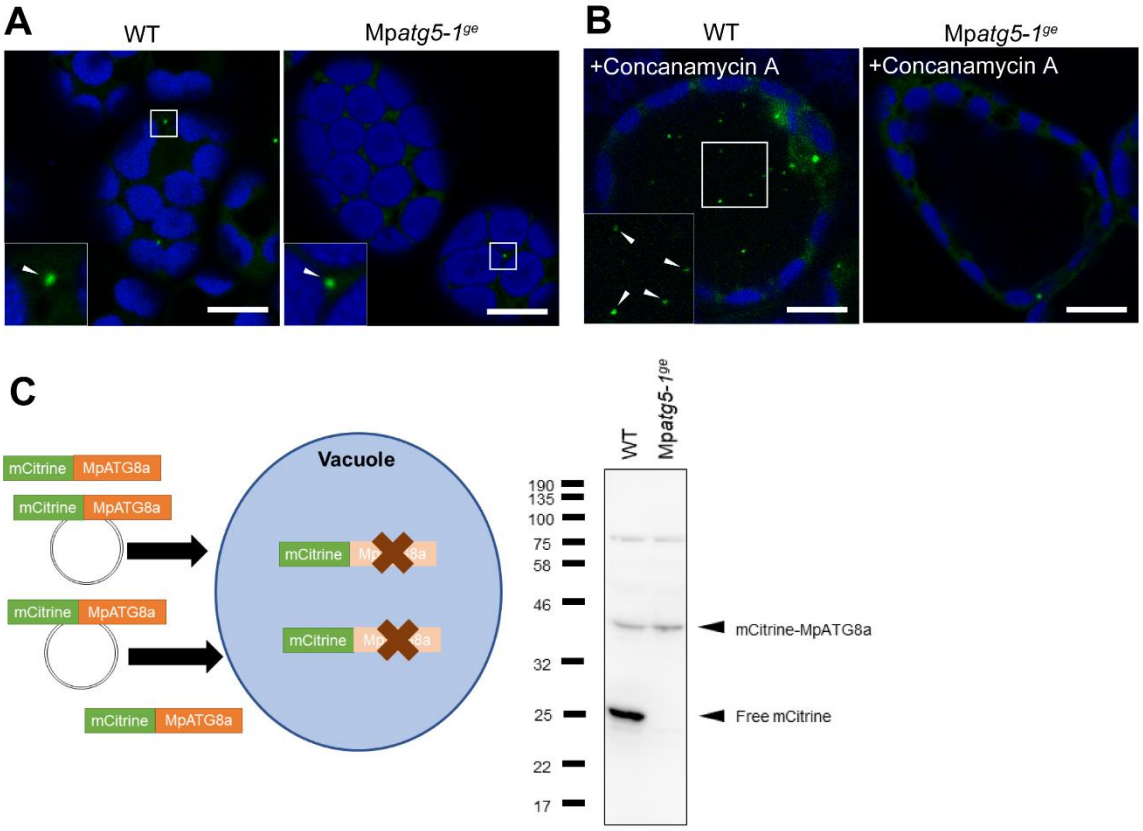

Figure 24. Subcellular localization of mCitrine-MpATG8a in thallus cells of the Mp*atg5* mutant

(**A**) Subcellular localization of mCitrine-MpATG8a in thallus cells of the wild type (WT) and Mp*atg5-1*^{ge} under the normal growth condition. (**B**) Localization of mCitrine-MpATG8a under treatment of Concanamycin A. The insets are magnified images of the boxed regions. The green and blue colors indicate fluorescence from mCitrine and autofluorescence of chlorophyll, respectively. Bars = 10 μm. (**C**) Western blotting of five-day-old thalli expressing mCitrine-MpATG8a using the anti-GFP antibody.

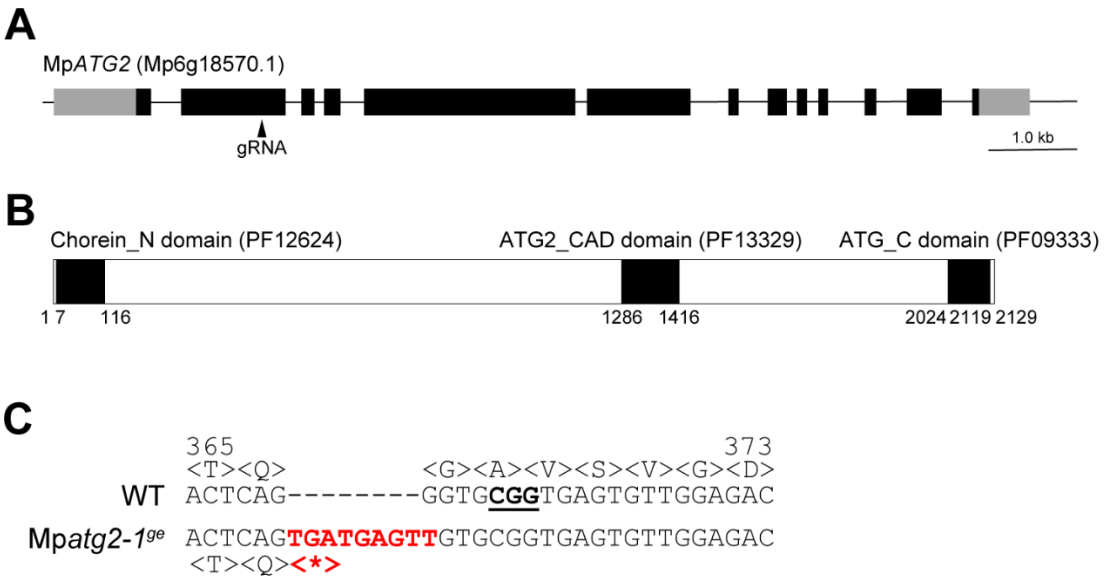

Figure 25. Generation of the Mp*atg2* mutant

(**A**) The gene body of Mp*ATG2*. The black and gray colors indicate the CDS and UTR of Mp*ATG2*, respectively. (**B**) The domain structure of MpATG2. (**C**) The sequence of the mutation in Mp*ATG2* introduced by genome editing. The underline indicates the PAM sequence. Inserted and substituted bases are shown in red. The asterisk indicates the stop codon.

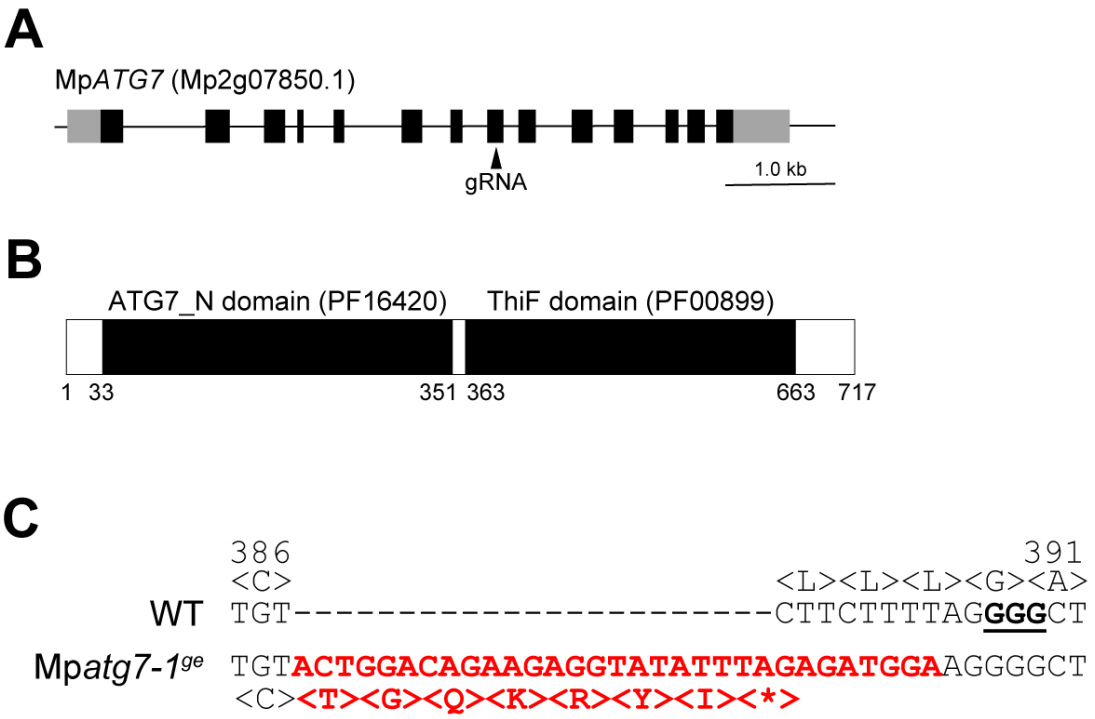

Figure 26. Generation of the Mp*atg7* mutant

(**A**) The gene body of Mp*ATG7*. The black and gray colors indicate the CDS and UTR of Mp*ATG7*, respectively. (**B**) The domain structure of MpATG7. (**C**) The sequence of the mutations in Mp*ATG7* introduced by genome editing. The underline indicates the PAM sequence. Inserted and substituted bases and inserted amino acid residues are shown in red. The asterisk indicates the stop codon.

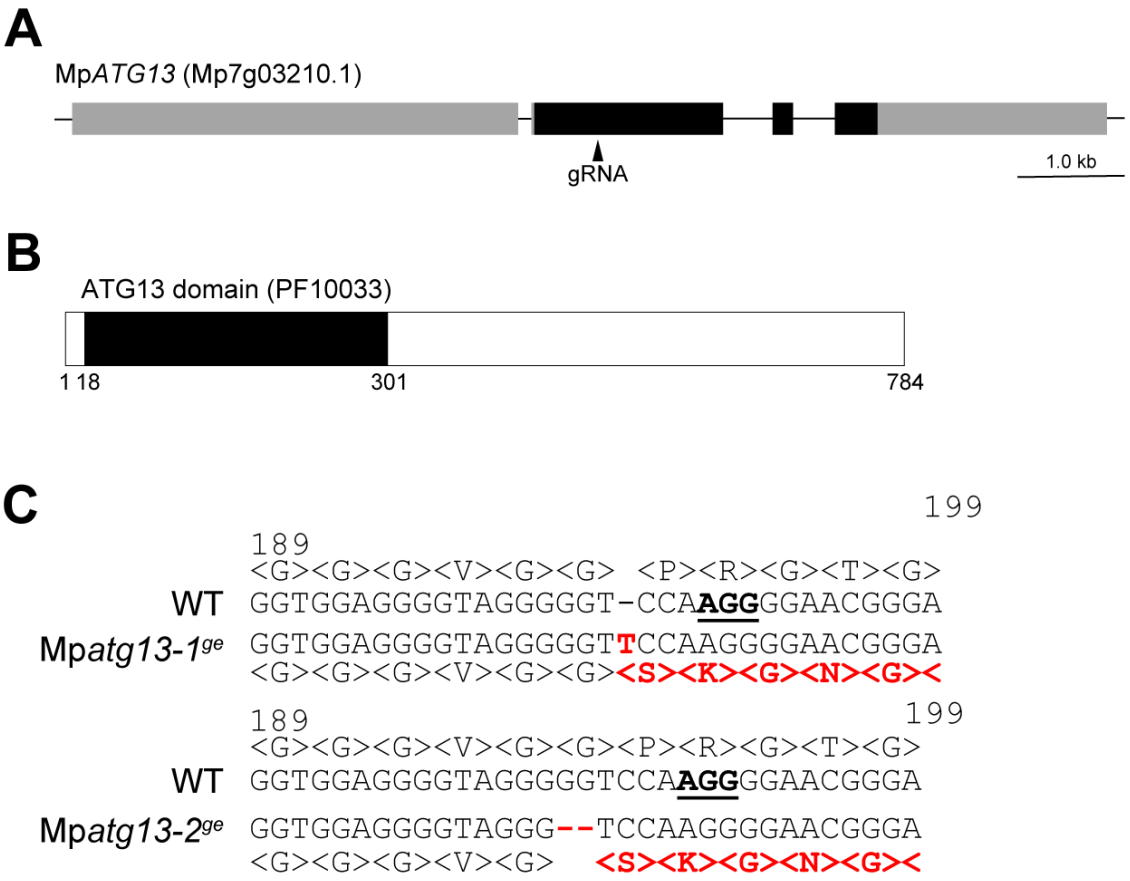

Figure 27. Generation of Mp*atg13* mutants

(**A**) The gene body of Mp*ATG13*. The black and gray colors indicate the CDS and UTR of Mp*ATG13*, respectively. (**B**) The domain structure of MpATG13. (**C**) Sequences of the mutations in Mp*ATG13* introduced by genome editing. The underline indicates the PAM sequence. Inserted and deleted bases, and substituted amino acid residues are shown in red. The asterisk indicates the stop codon.

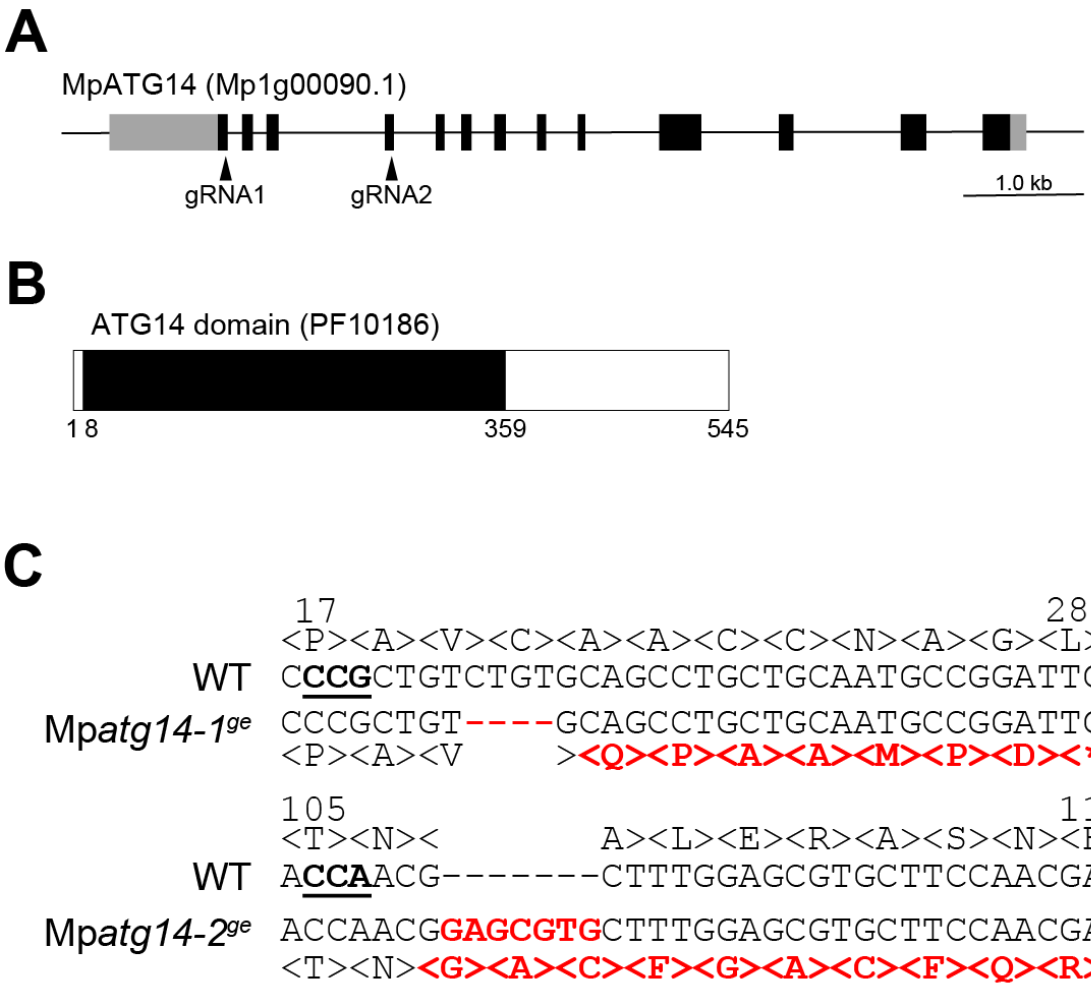

Figure 28. Generation of Mp*atg14* mutants

(**A**) The gene body of Mp*ATG14*. The black and gray colors indicate the CDS and UTR of Mp*ATG14*, respectively. (**B**) The domain structure of MpATG14. (**C**) Sequences of the mutations in Mp*ATG14* introduced by genome editing. The underline indicates the PAM sequence. Inserted and deleted bases and substituted amino acid residues are shown in red. The asterisk indicates the stop codon.

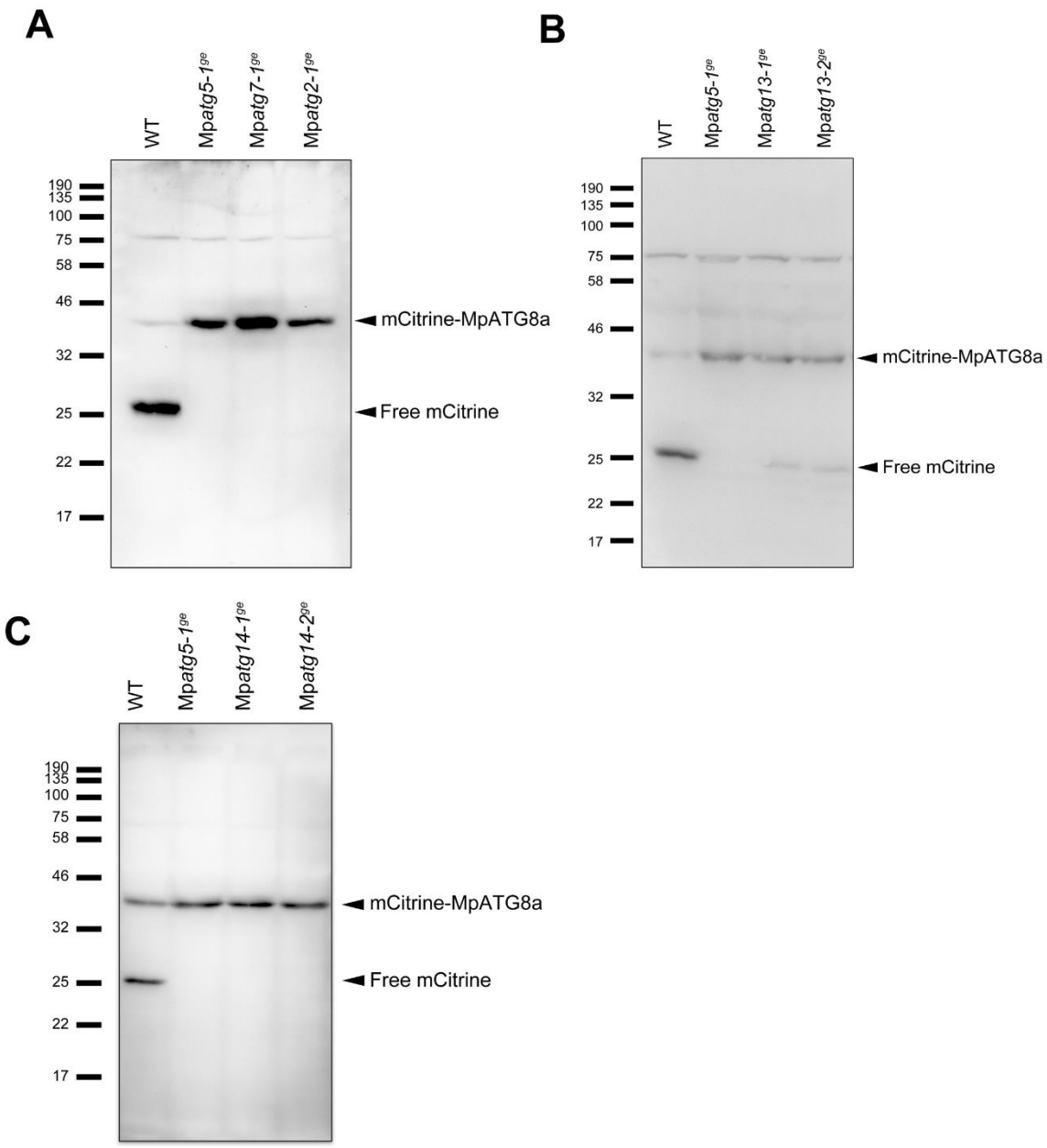

Figure 29. Cleavage assay of mCitrine-MpATG8a in Mp*atg* mutants

Western blotting of five-day-old thalli expressing mCitrine-MpATG8a in the wild type (WT) and Mp*atg5-1*^{ge} (**A to C**), Mp*atg2-1*^{ge} (**A**), Mp*atg7-1*^{ge} (**A**), Mp*atg13-1*^{ge} and Mp*atg13-2*^{ge} (**B**), and Mp*atg14-1*^{ge} and Mp*atg14-2*^{ge} (**C**) using the anti-GFP antibody.

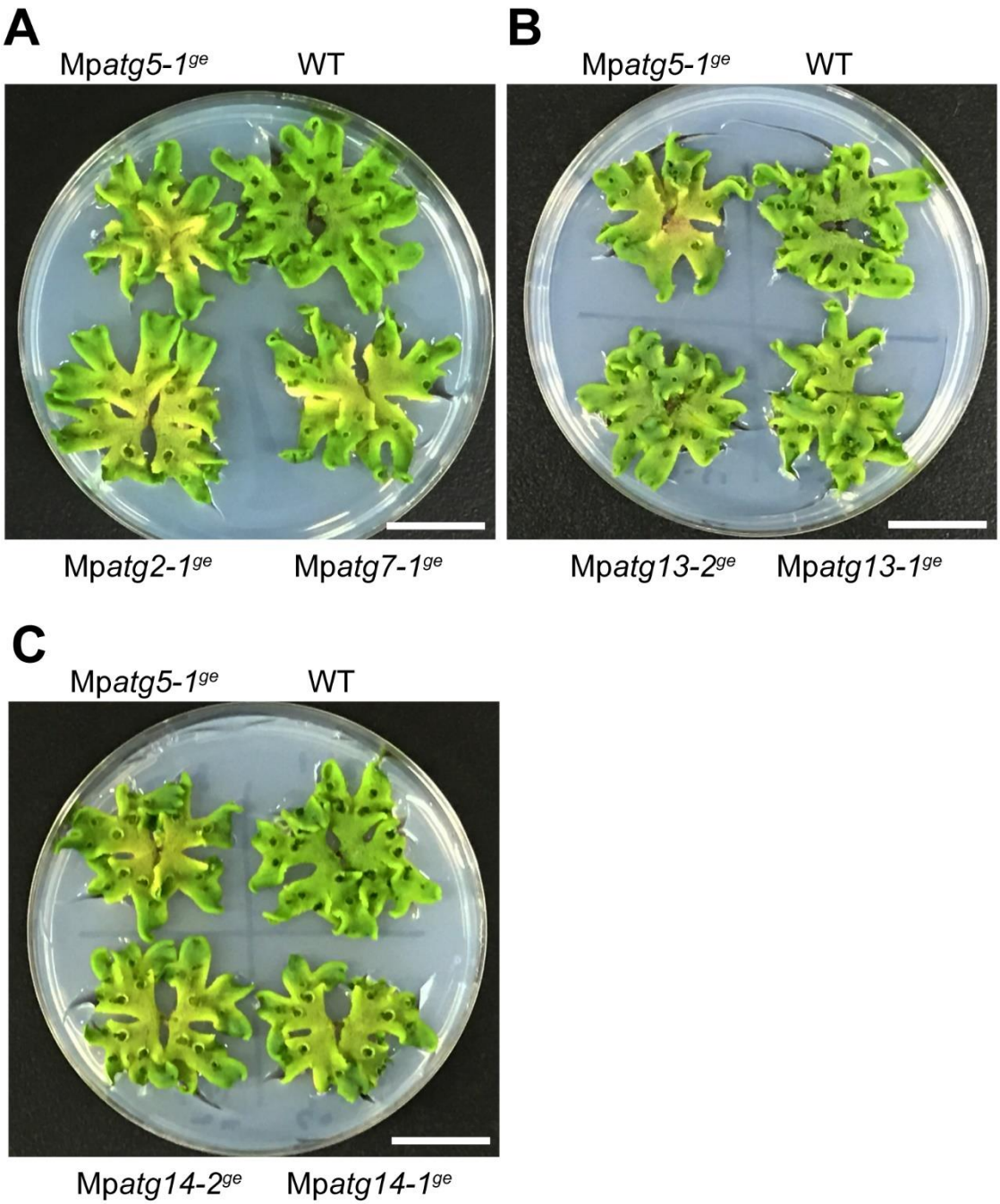

Figure 30. Chlorosis of Mp*atg* mutants

26-day-old thalli of the wild type (WT) and Mp*atg5-1*^{ge} (**A to C**), Mp*atg2-1*^{ge} (**A**), Mp*atg7-1*^{ge} (**A**), Mp*atg13-1*^{ge} and Mp*atg13-2*^{ge} (**B**), and Mp*atg14-1*^{ge} and Mp*atg14-2*^{ge} (**C**) grown under the normal condition. Bars = 2 cm.

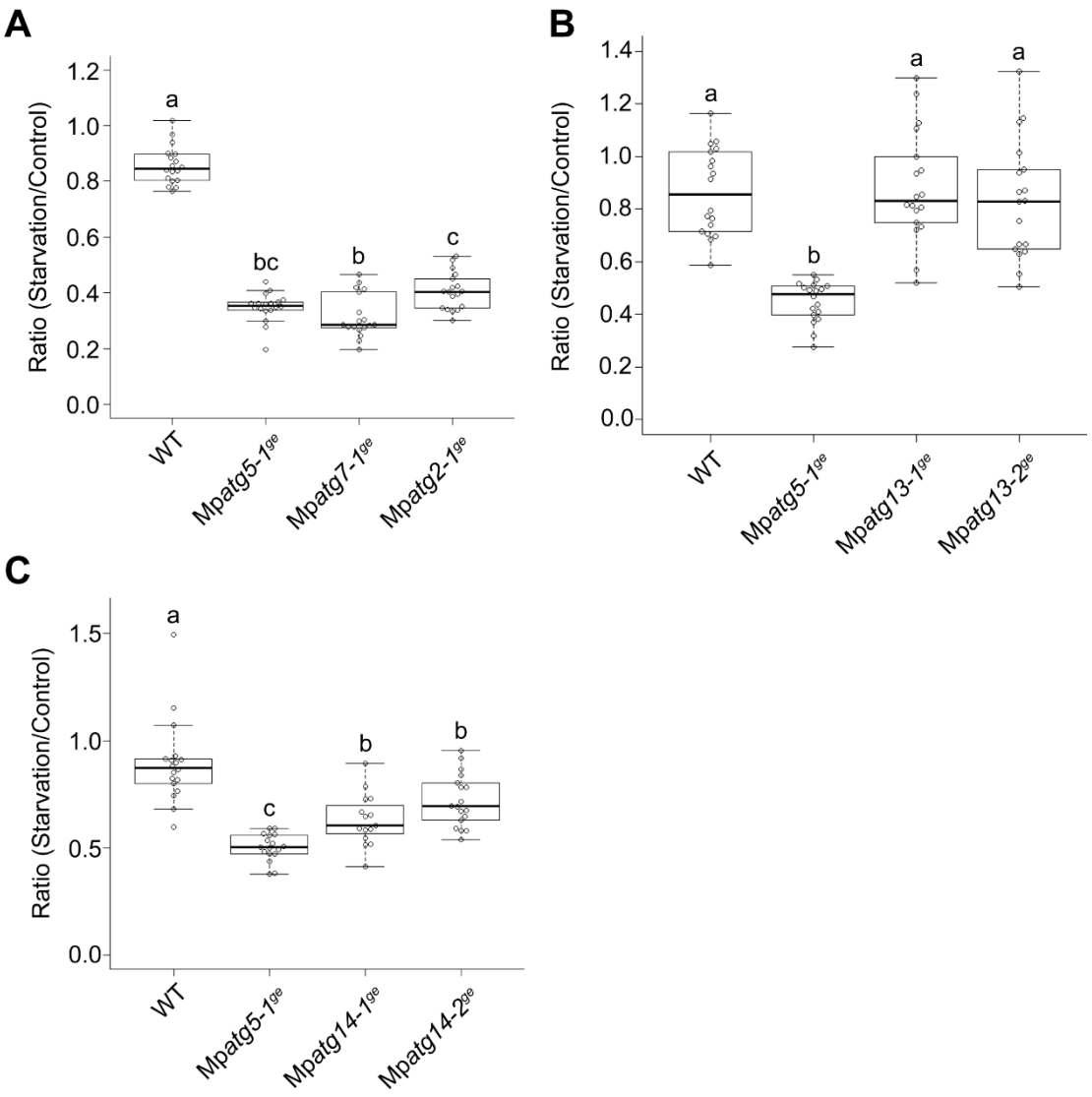

Figure 31. Higher sensitivity to nutrient starvation in Mp*atg* mutants

Five-day-old thalli of the wild type (WT) and Mp*atg5-1*^{ge} (**A to C**), Mp*atg2-1*^{ge} (**A**), Mp*atg7-1*^{ge} (**A**), Mp*atg13-1*^{ge} and Mp*atg13-2*^{ge} (**B**), and Mp*atg14-1*^{ge} and Mp*atg14-2*^{ge} (**C**) were grown in 1/2× Gamborg's B5 medium under the light condition (control) or 0.05% (w/v) MES buffer under the dark condition (starvation) for five days. Chlorophyll contents are measured and the ratio of those in starvation to control is plotted. (**A, B**) n = 18 samples (three thalli were treated as one sample for correct measurement of the fresh

weight). (**C**) n = 18 samples for WT, 17 for Mp*atg5-1*^{ge}, 15 for Mp*atg14-1*^{ge}, and 18 for Mp*atg14-2*^{ge}. The boxes and solid lines in the boxes indicate the first quartile and third quartile, and median values, respectively. The whiskers indicate 1.5× interquartile ranges. Different letters denote significant differences based on Tukey's test ($p < 0.05$).

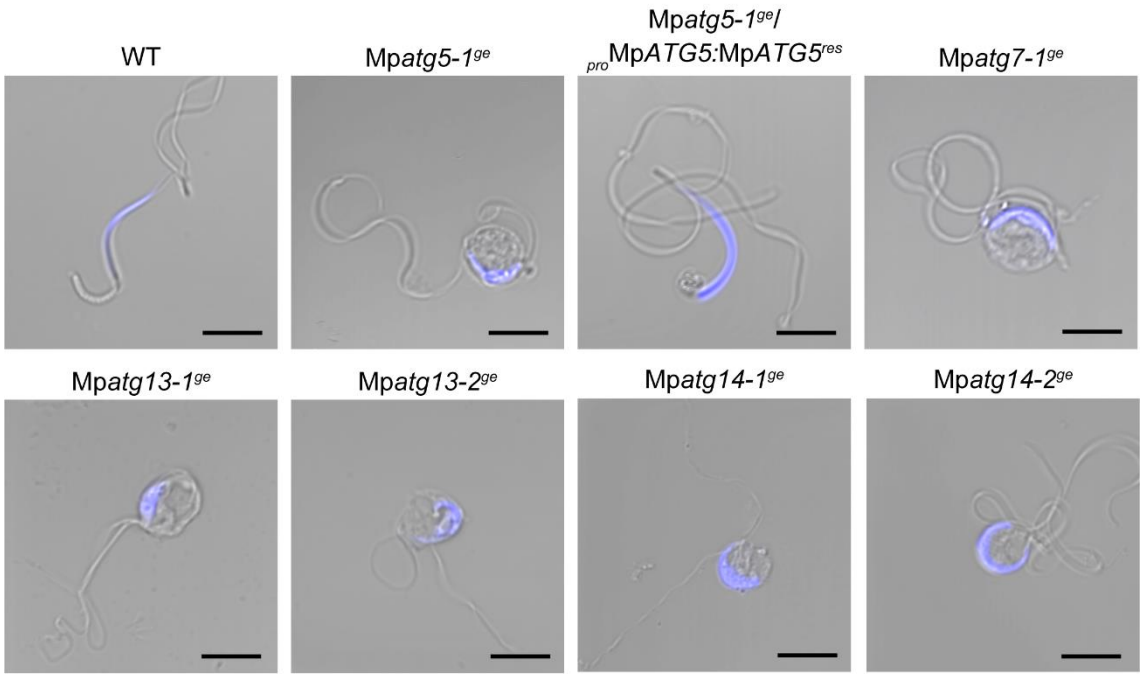

Figure 32. Spermatozoids of Mp*atg* mutants

Spermatozoids released from antheridia of the wild type (WT) and Mp*atg* mutants stained by Hoechst. The blue color indicates the fluorescence from Hoechst. Bars = 5 μm.

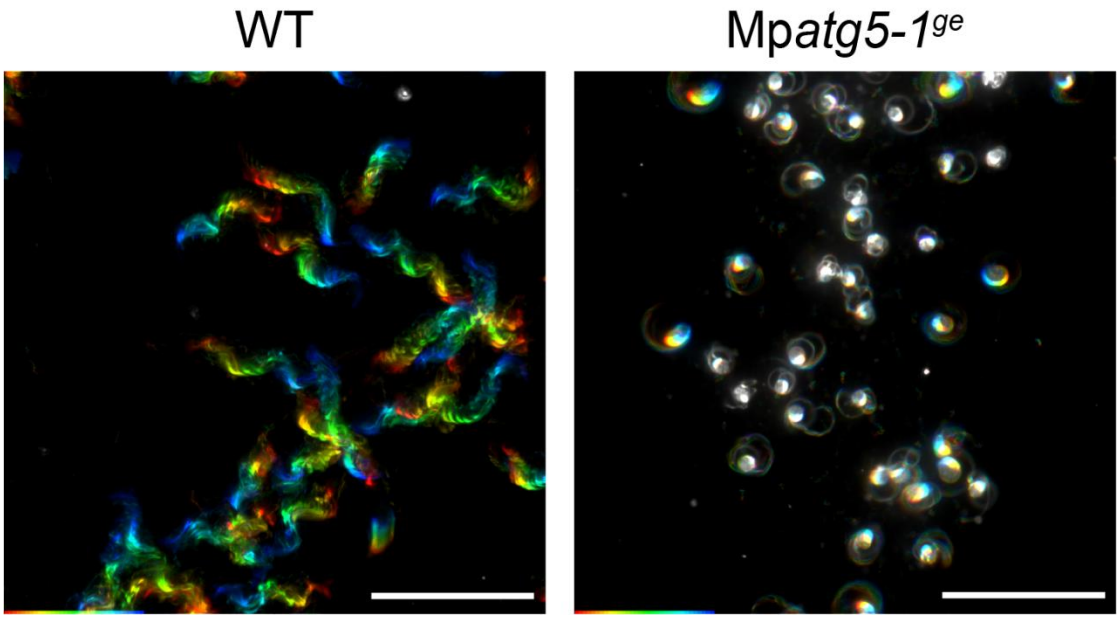

Figure 33. Motility of spermatozoids of the Mp*atg5-1*^{g} mutant

One-second trajectories of spermatozoid movement of the wild type (WT) and Mp*atg5-1*^{ge}. 33 images, which are differently colored along the time course, were overlaid. Bars = 50 μm.

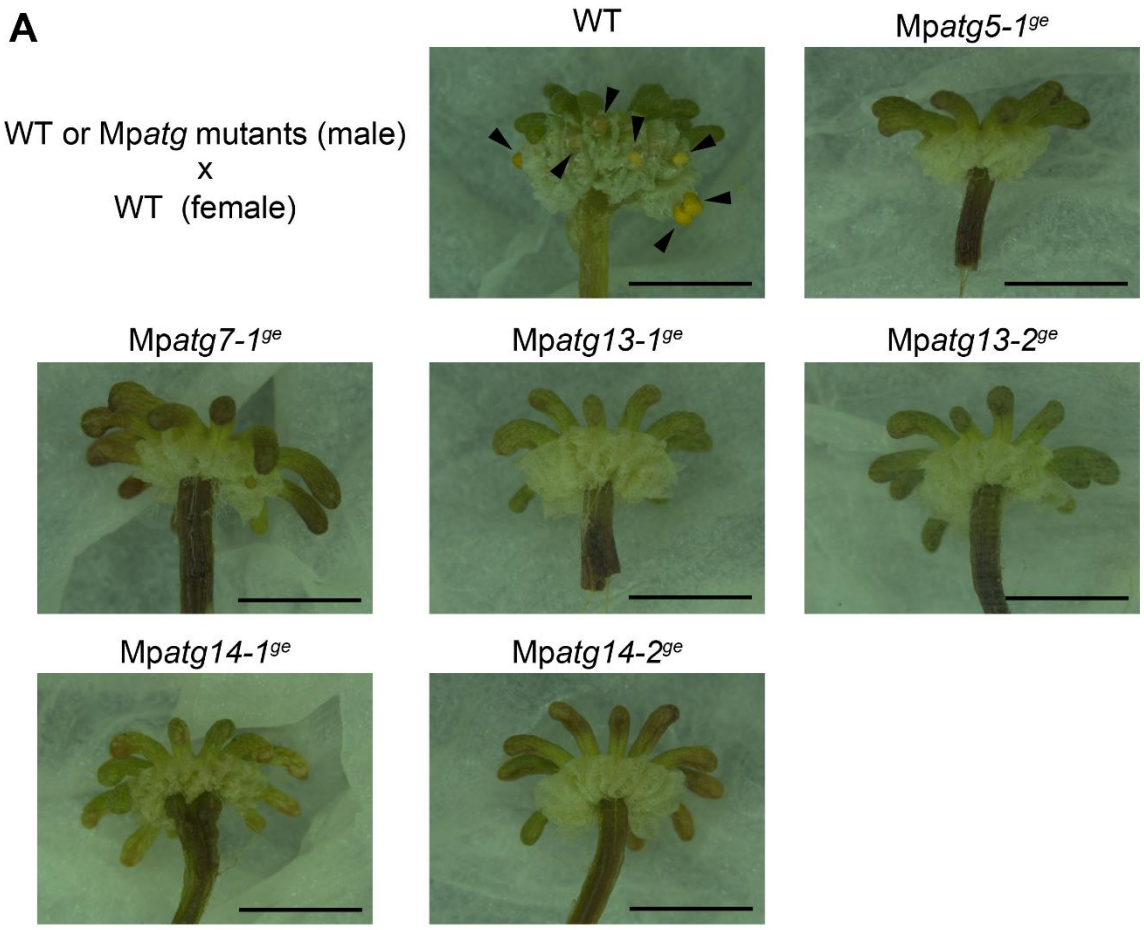

B

Genotype	Fertility (%)	
WT	100	n = 8
Mp*atg5-1*^{ge}	0	n = 6
Mp*atg7-1*^{ge}	0	n = 6
Mp*atg13-1*^{ge}	0	n = 5
Mp*atg13-2*^{ge}	0	n = 8
Mp*atg14-1*^{ge}	0	n = 8
Mp*atg14-2*^{ge}	0	n = 8

Figure 34. Fertility of Mp*atg* spermatozoids

(**A**) Crossing of the wild type (WT) or Mp*atg* mutants (male) with WT (female) were

performed, and three to five weeks after crossing archegoniophores were observed. Arrowheads indicate yellow sporangia. Bars = 0.5 cm. (**B**) The percentage of archegoniophores with yellow sporangia. n: the number of archegoniophores used for crossing.

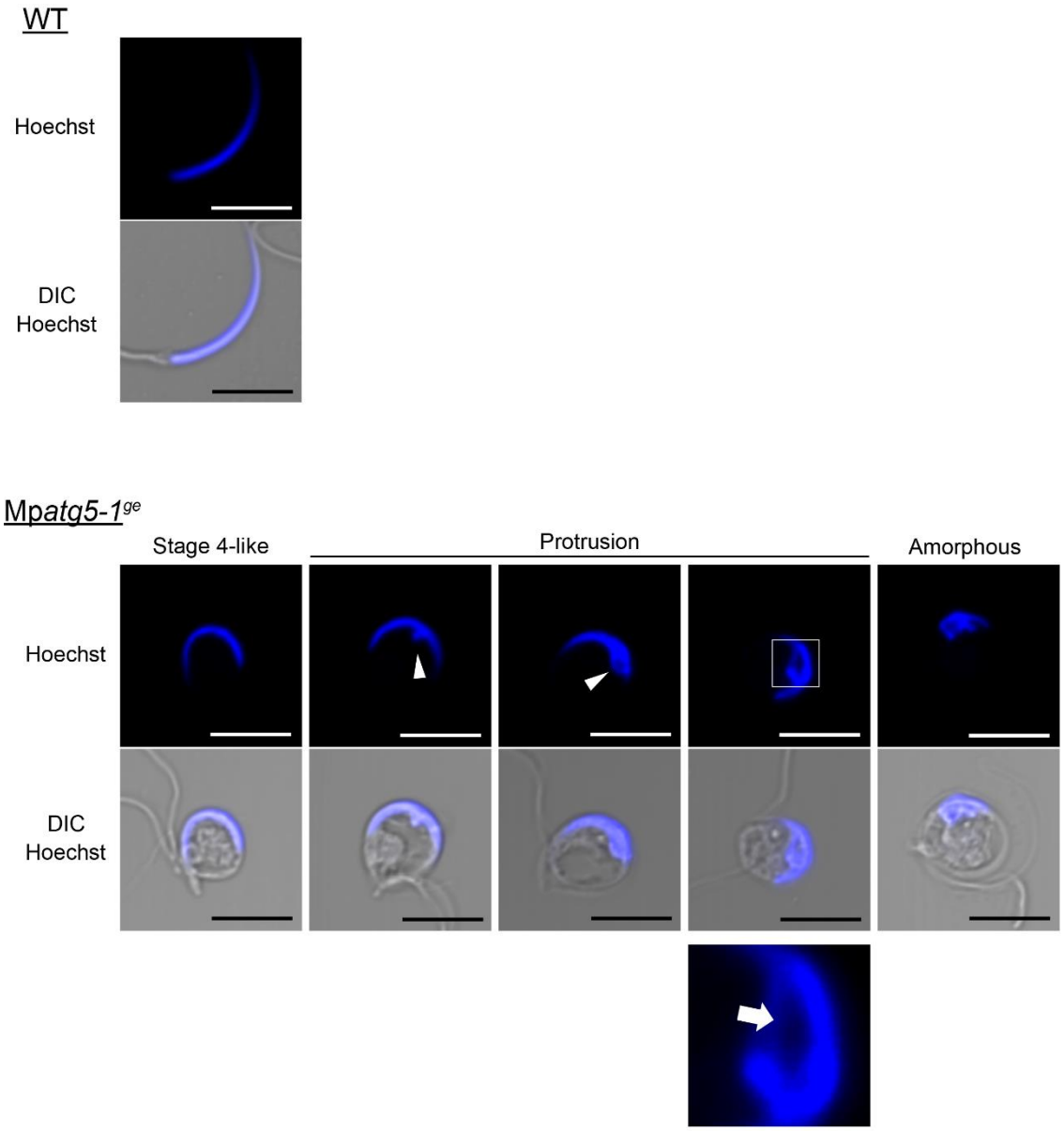

Figure 35. The nucleus in the spermatozoid of Mp*atg5-1*^{ge}

Spermatozoids released from antheridia of the wild type (WT) or Mp*atg5-1*^{ge} stained by Hoechst. Arrowheads and an arrow indicate protrusions of the nucleus and a hollow in nuclei respectively. The blue color indicates nuclei visualized by Hoechst. The lower panel is a magnified image of the boxed region. Bars = 5 μm.

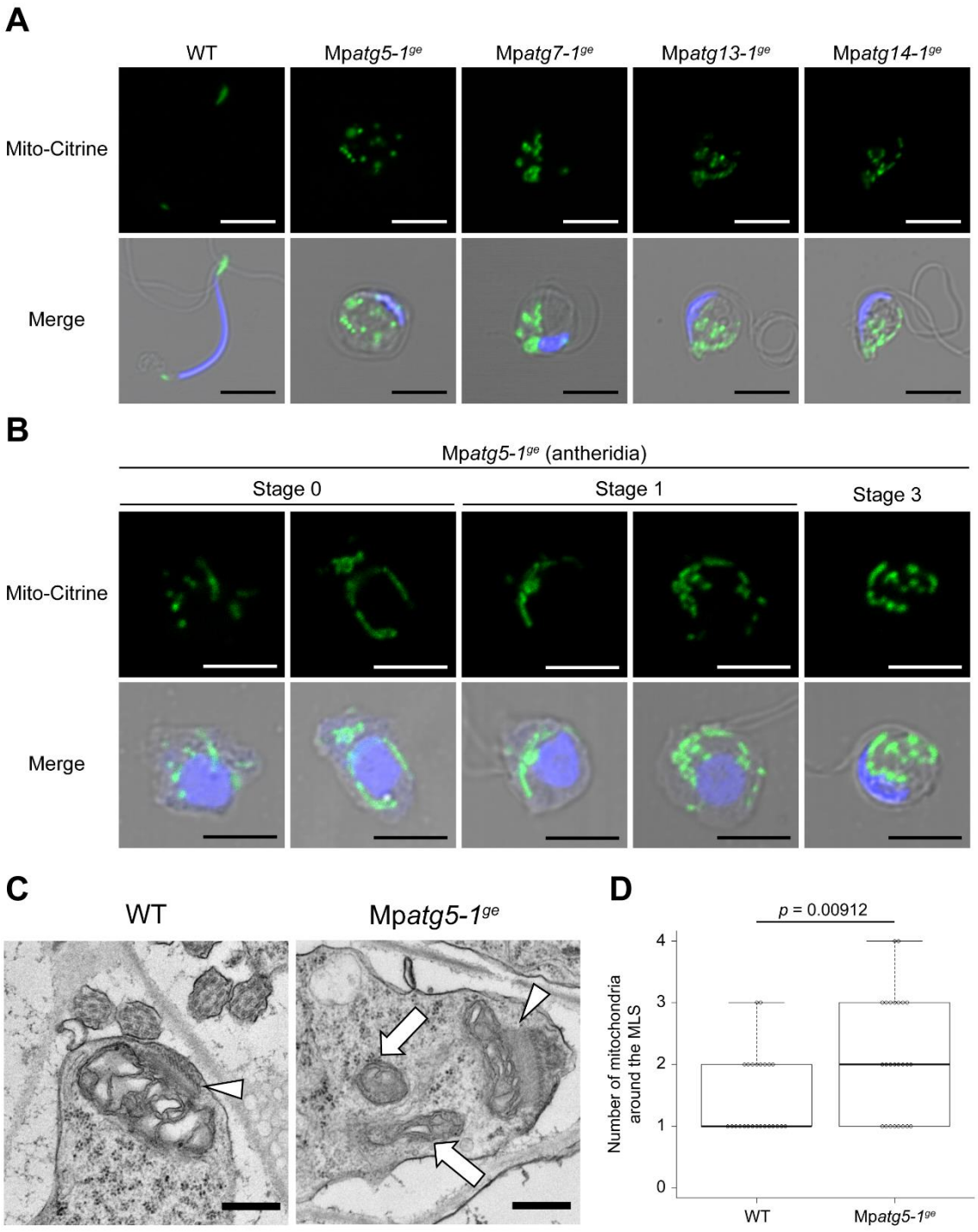

Figure 36. Mitochondria in spermatozoids and spermatids of Mp*atg* mutants

(**A**) Mitochondria in spermatozoids of the wild type (WT) and Mp*atg* mutants. (**B**) Mitochondria in cell wall-digested antheridial cells of Mp*atg5-1*^{ge}. The green and blue

colors indicate the fluorescence from Citrine and Hoechst, respectively. Bars = 5 μm. (**C, D**) TEM observation of mitochondria in spermatids. (**C**) TEM images of wild-type (WT) and Mp*atg5-1*^{ge} spermatids. Arrows indicate mitochondria that are not attached to the MLS (arrowheads). Bars = 200 nm. (**D**) Quantification of the number of mitochondria around the MLS in WT and Mp*atg5-1*^{ge} spermatids. n = 25 images. The boxes and solid lines in the boxes indicate the first quartile and third quartile, and median values, respectively. The whiskers indicate 1.5× interquartile ranges. Statistical differences were analyzed by Welch's t test.

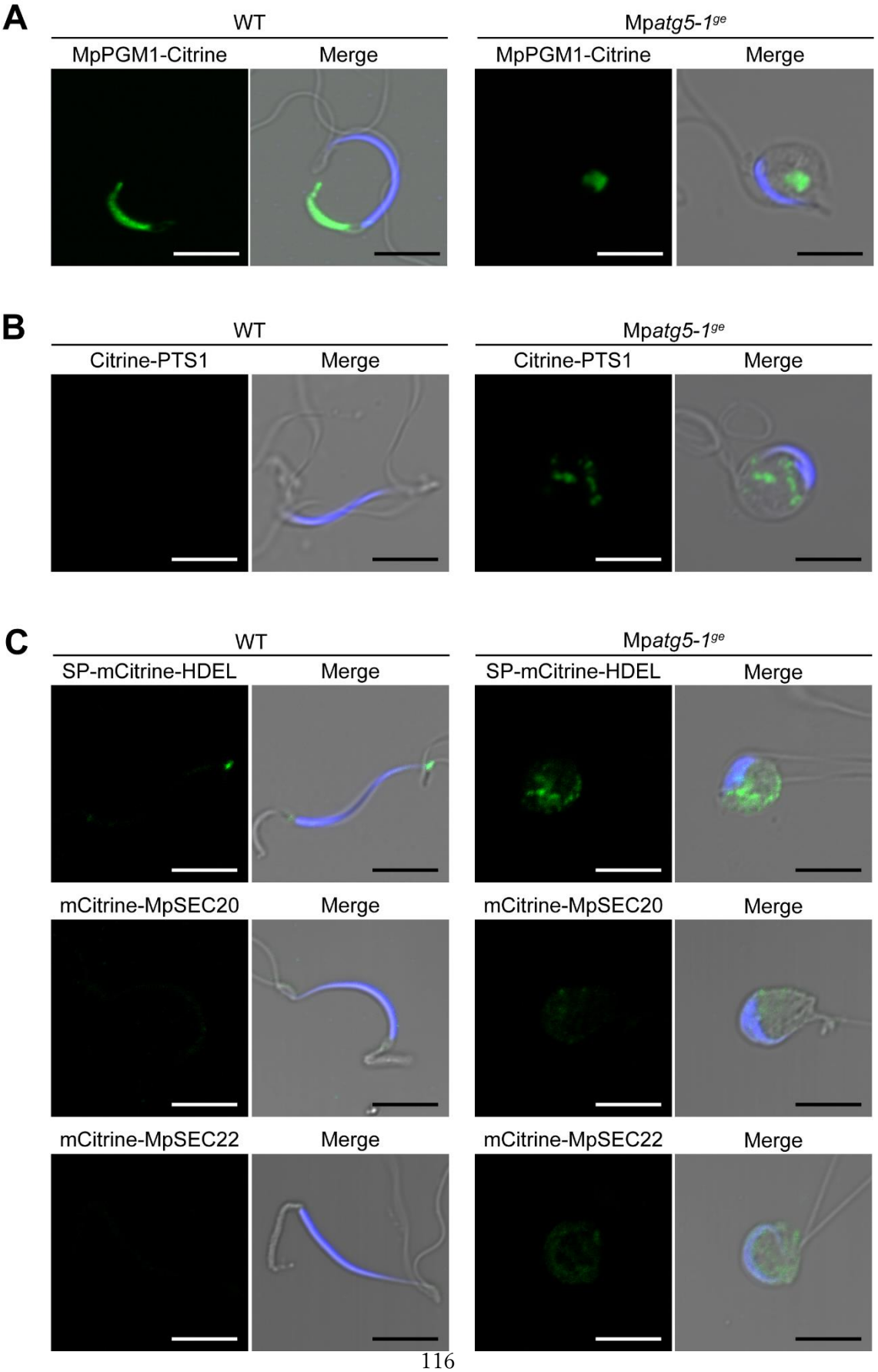
A
WT
Mpatg5-1ge
MpPGM1-Citrine
Merge
MpPGM1-Citrine
Merge
B
WT
Mpatg5-1ge
Citrine-PTS1
Merge
Citrine-PTS1
Merge
C
WT
Mpatg5-1ge
SP-mCitrine-HDEL
Merge
SP-mCitrine-HDEL
Merge
mCitrine-MpSEC20
Merge
mCitrine-MpSEC20
Merge
mCitrine-MpSEC22
Merge
mCitrine-MpSEC22
Merge

Figure 37. Organelles in spermatozoids of Mp*atg5-1*^{ge}

The plastid (**A**), peroxsiomes (**B**), and the ER (**C**) in spermatozoids of the wild type (WT) and Mp*atg5-1*^{ge} were observed. The green and blue colors indicate the fluorescence from Citrine or mCitrine and Hoechst, respectively. Bars = 5 μm.

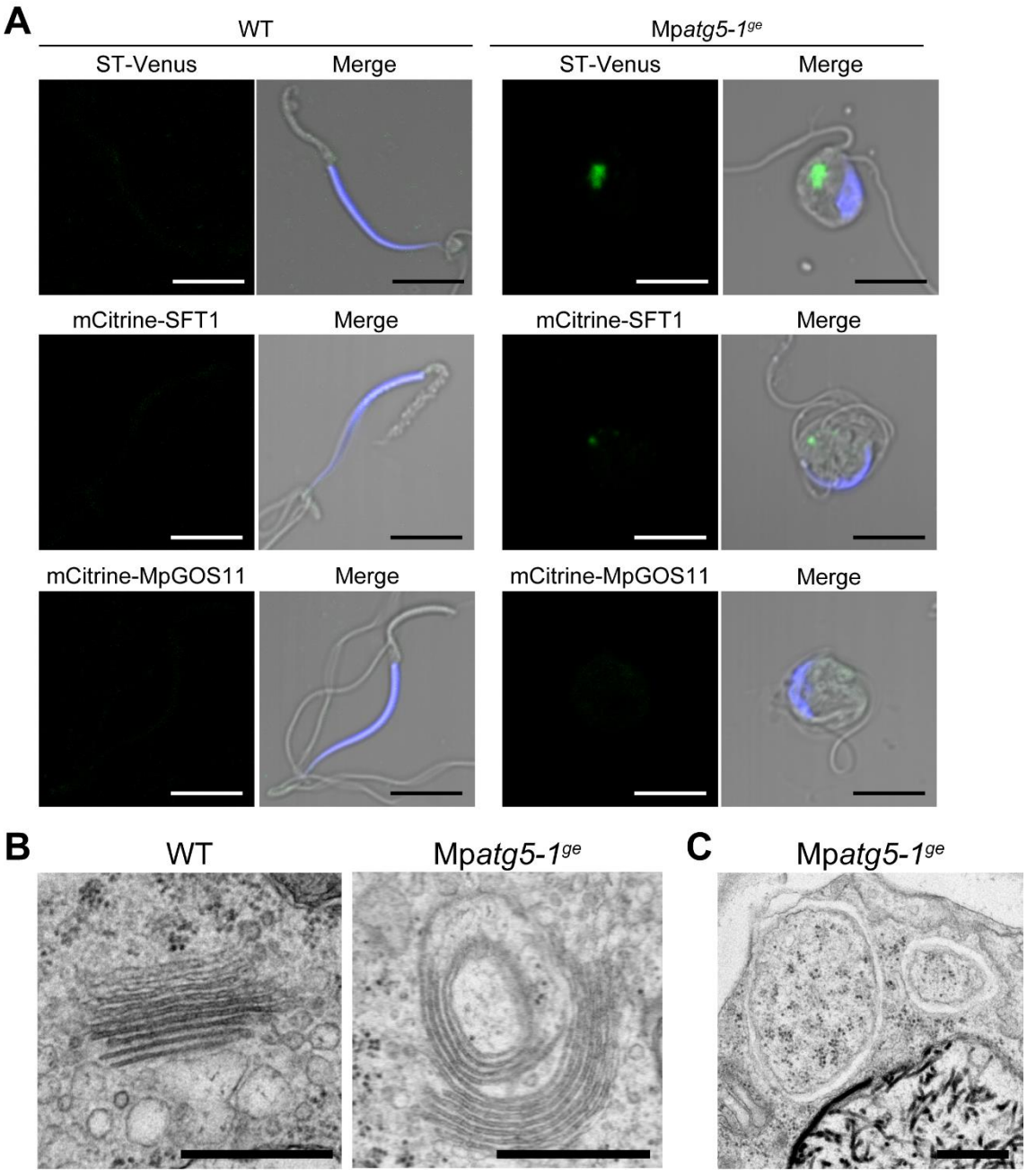

Figure 38. The Golgi apparatus in spermatids and the spermatozoids of Mp*atg5-1*^{ge}

(**A**) The Golgi apparatus in spermatozoids in the wild type (WT) and Mp*atg5-1*^{ge} visualized with ST-Venus (upper panels), mCitrine-SFT1 (middle panels), and mCitrine-MpGPS11 (lower panels). The green and blue colors indicate the fluorescence from Venus

or mCitrine and Hoechst, respectively. Bars = 5 μm. (**B**) TEM images of the Golgi apparatus in wild-type (WT) and Mp*atg5-1*^{ge} spermatids. Bars = 500 nm. (**C**) Double-membraned structures in a spermatid of Mp*atg5-1*^{ge}. Bar = 500 nm.

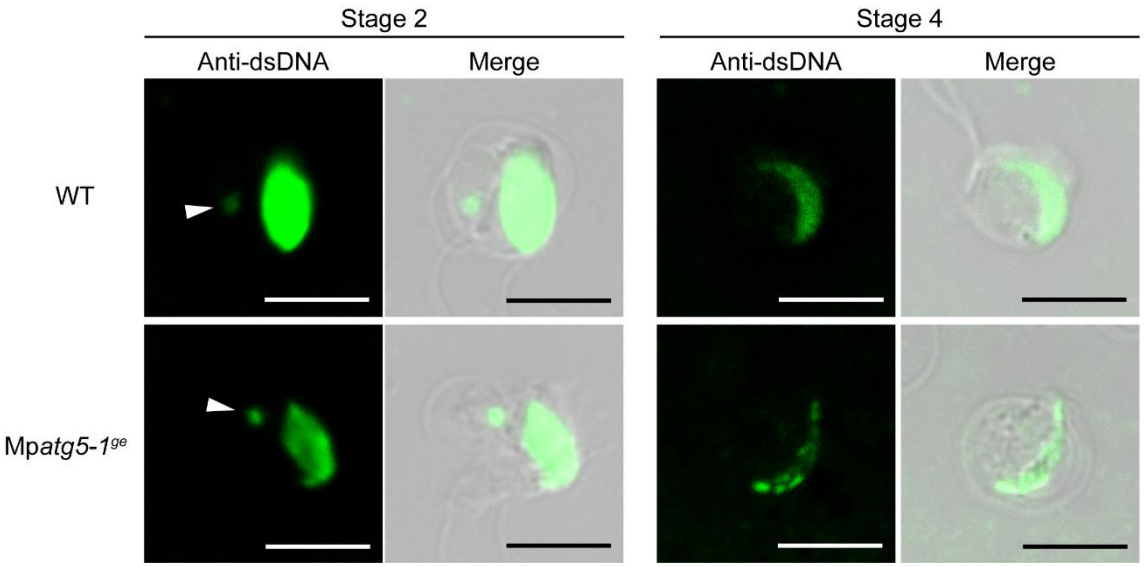

Figure 39. Plastid DNA in Mp*atg5-1*^{ge}

Plastid DNA was detected using the anti-dsDNA antibody. Arrows indicate plastid DNA. The green color indicates the fluorescence from Alexa Fluor 488 plus. Bars = 5 μm.

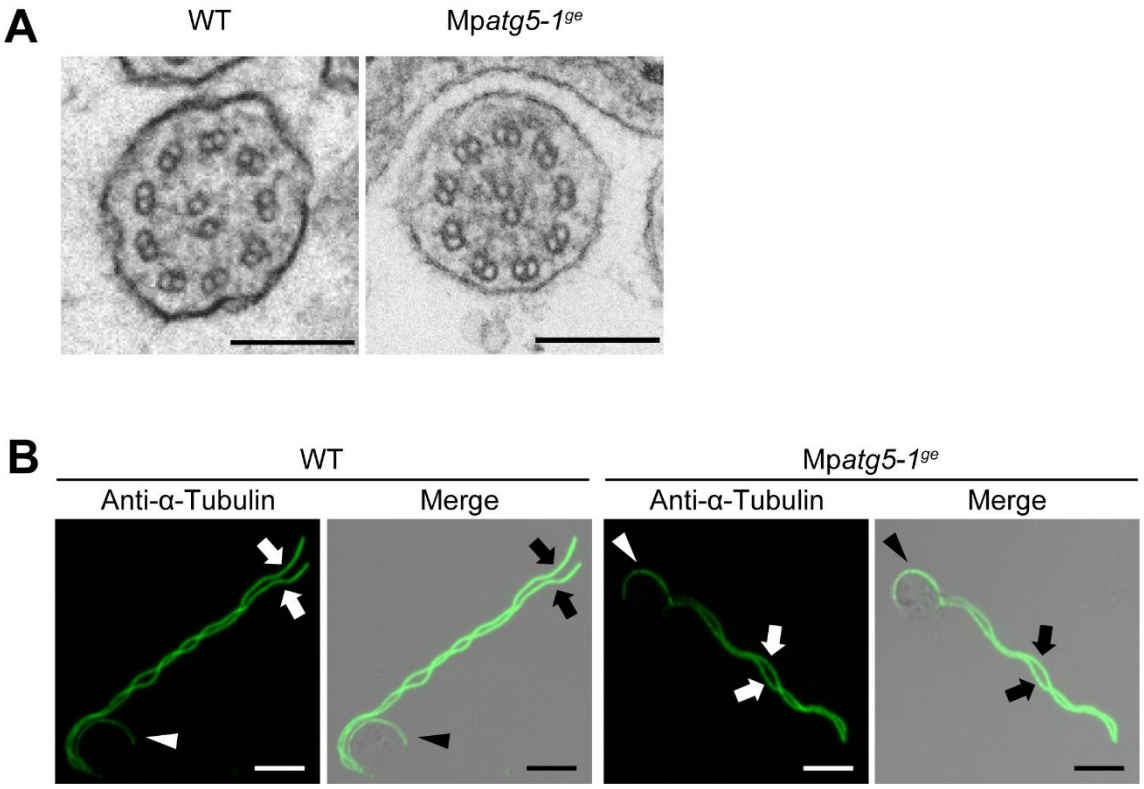

Figure 40. Microtubule structures in the spermatid of Mp*atg5-1*^{ge}

(**A**) The structure of flagella in the spermatid of the wild type (WT) and Mp*atg5-1*^{ge}. Bars = 200 nm. (**B**) Structures comtaining microtubules in the wild-type (WT) and Mp*atg5-1*^{ge} spermatid. Arrowheads and arrows indicate the spline and flagella, respectively. The green color indicates the fluorescence from Alexa Fluor 488. Bars = 5 μm.

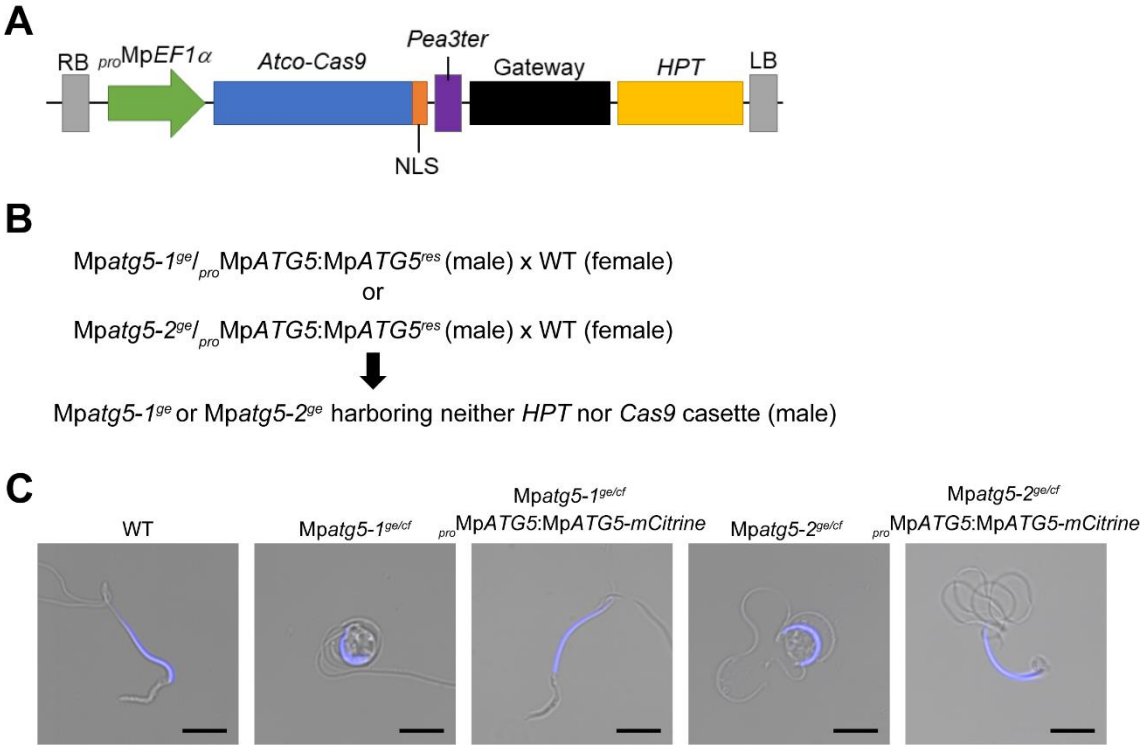

Figure 41. Generation of the Mp*atg5* mutant harboring no T-DNA cassette

(**A**) T-DNA inserted into Mp*atg5-1*^{ge} or Mp*atg5-2*^{ge} (Sugano et al. 2018). (**B**) Scheme of generation of the Mp*atg5* mutant without the T-DNA cassette. (**C**) Spermatozoids of Mp*atg5-1*$^{ge/cf}$ and Mp*atg5-2*$^{ge/cf}$. The blue color indicates the fluorescence from Hoechst. Bars = 5 μm.

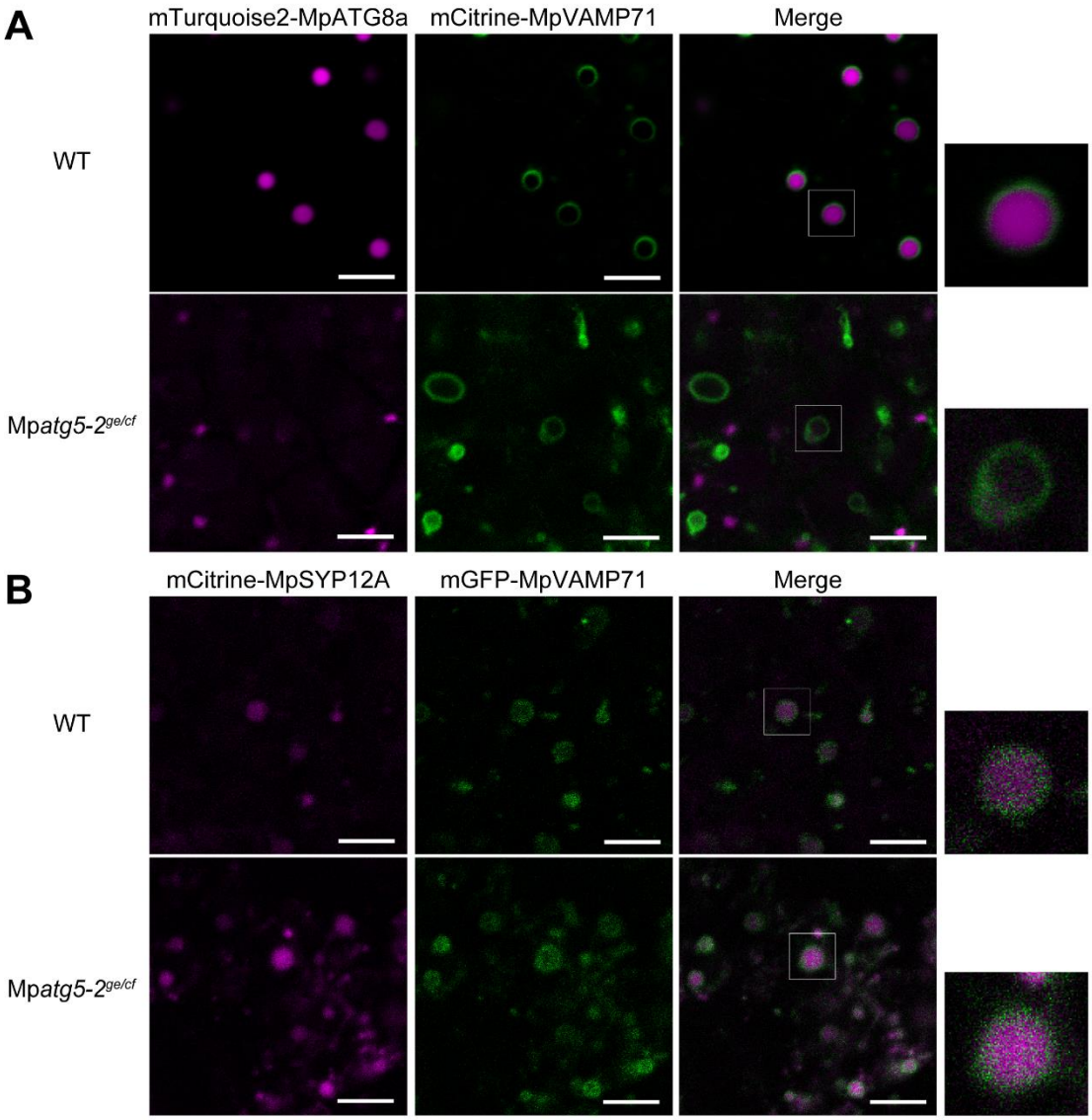

Figure 42. Subcellular localization of MpATG8a and MpSYP12A in antheridial cells

Subcellular localization of mTurquoise2-MpATG8a (**A**) and mCitrine-MpSYP12A (**B**) in hand-sectioned antheridia of the wild type (WT) and Mp*atg5-2*$^{ge/cf}$. The right panels are magnified images of the boxed regions. Bars = 5 μm. (**A**) The magenta and green colors indicate the fluorescence from mTurquoise2 and Citrine, respectively. (**B**) The magenta and green colors indicate the fluorescence from mCitrine and mGFP, respectively.

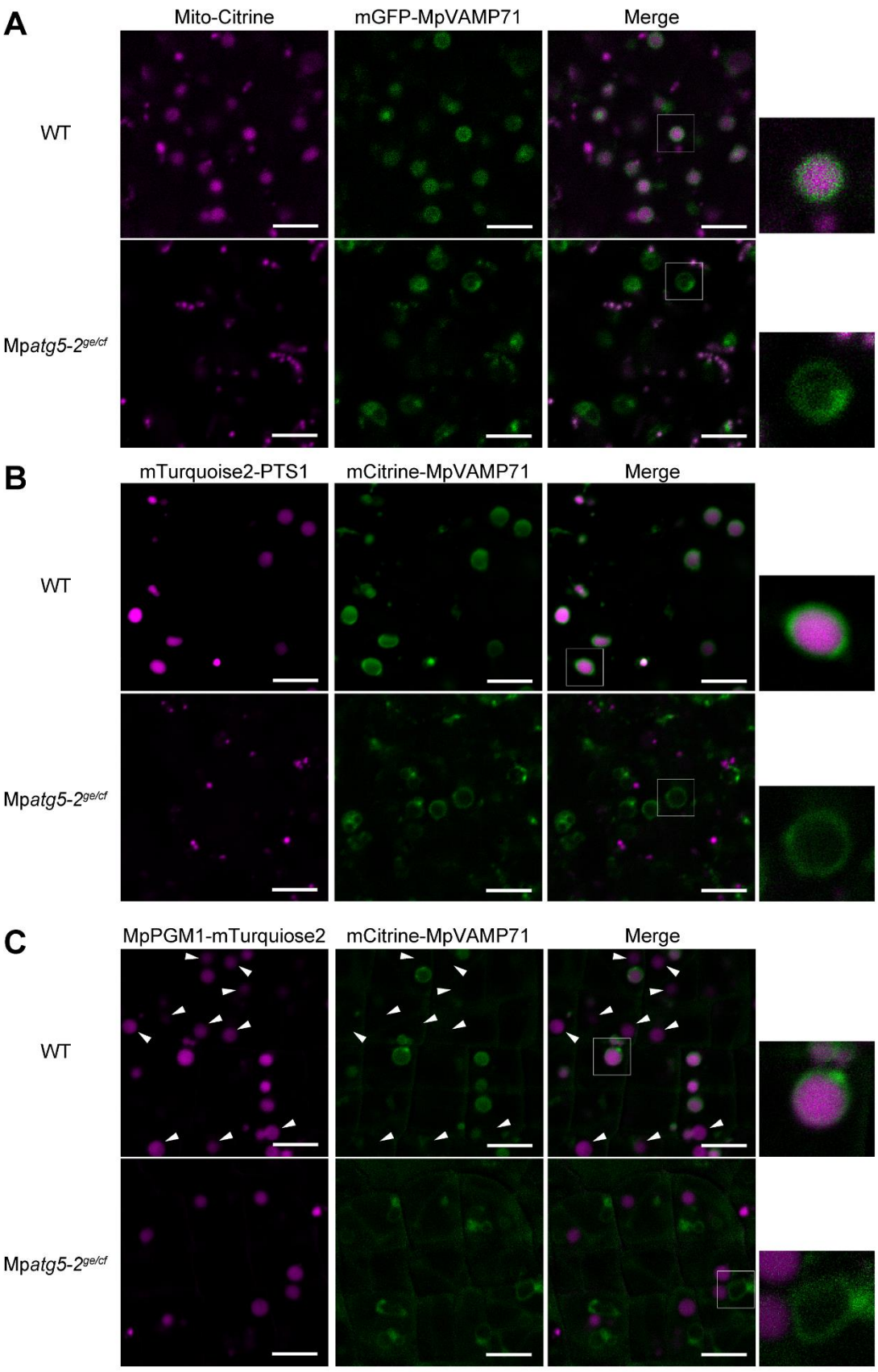
A
Mito-Citrine
mGFP-MpVAMP71
Merge
WT
Mpatg5-2ge/cf
B
mTurquoise2-PTS1
mCitrine-MpVAMP71
Merge
WT
Mpatg5-2ge/cf
C
MpPGM1-mTurquiose2
mCitrine-MpVAMP71
Merge
WT
Mpatg5-2ge/cf

Figure 43. Subcellular localization of the mitochondria marker, the peroxisome marker, and the plastid marker in antheridial cells

Subcellular localization of Mito-Citrine (**A**), mTurquoise2-PTS1 (**B**), and MpPGM1-mTurquoise2 (**C**) in hand-sectioned antheridia of the wild type (WT) and Mp*atg5-2*$^{ge/cf}$. The right panels are magnified images of the boxed regions. Bars = 5 μm. (**A**) The magenta and green colors indicate the fluorescence from Citrine and mGFP, respectively. Mito-Citrine was expressed under the Mp*SYP2* promoter for moderate expression. (**B and C**) The magenta and green colors indicate the fluorescence from mTurquoise2 and mCitrine, respectively. Arrowheads indicate plastids.

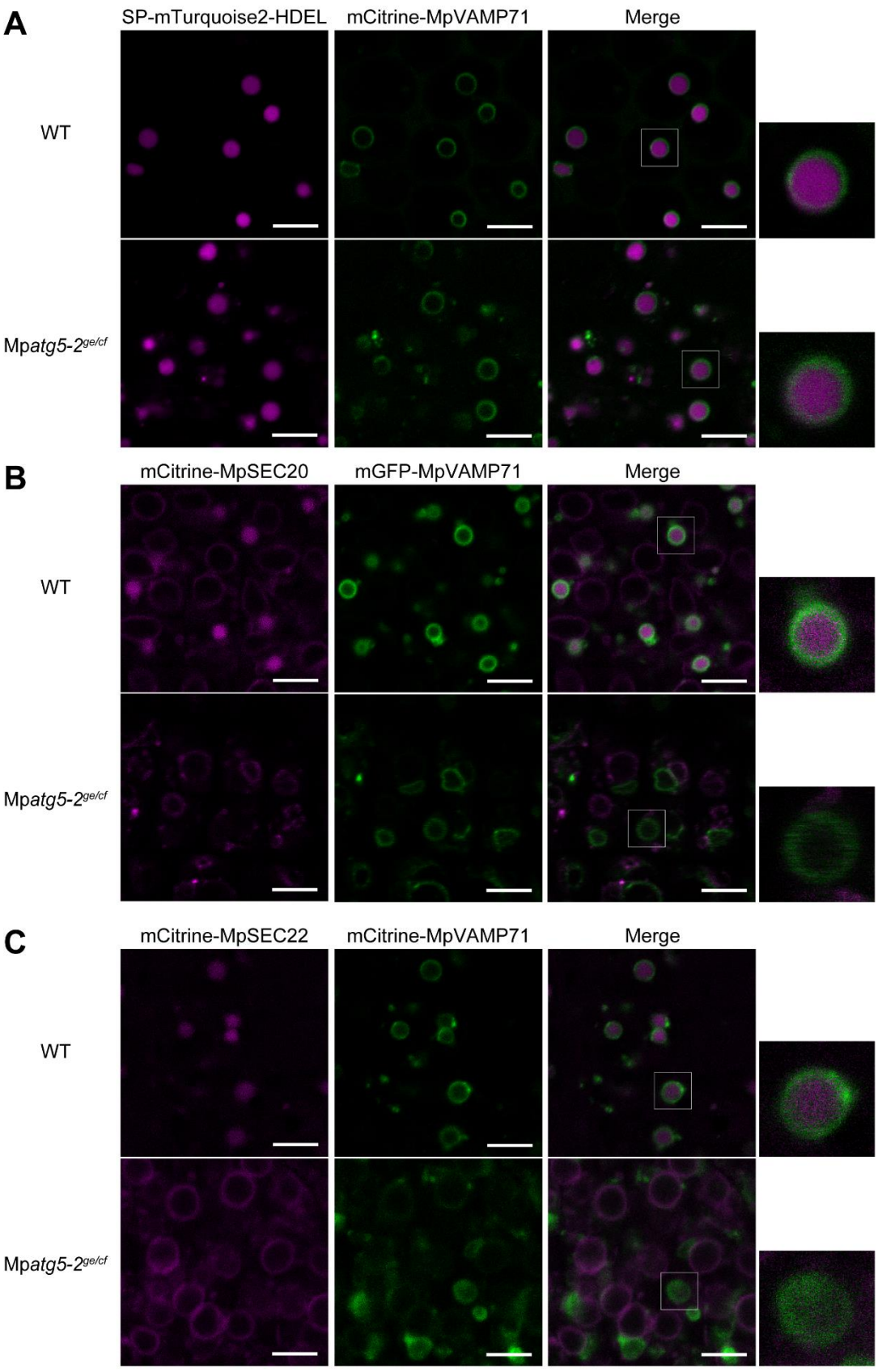
A
SP-mTurquoise2-HDEL
mCitrine-MpVAMP71
Merge
WT
Mpatg5-2ge/cf
B
mCitrine-MpSEC20
mGFP-MpVAMP71
Merge
WT
Mpatg5-2ge/cf
C
mCitrine-MpSEC22
mCitrine-MpVAMP71
Merge
WT
Mpatg5-2ge/cf

Figure 44. Subcellular localization of the ER markers in antheridial cells

Subcellular localization of SP-mTurquoise2-HDEL (**A**), mCitrine-MpSEC20 (**B**), and mCitrine-MpSEC22 (**C**) in hand-sectioned antheridia of the wild type (WT) and Mp*atg5-2*$^{ge/cf}$. The right panels are magnified images of the boxed regions. Bars = 5 μm. (**A**) The magenta and green colors indicate the fluorescence from mTurquoise2 and mCitrine, respectively. (**B and C**) The magenta and green colors indicate the fluorescence from mCitrine and mGFP, respectively.

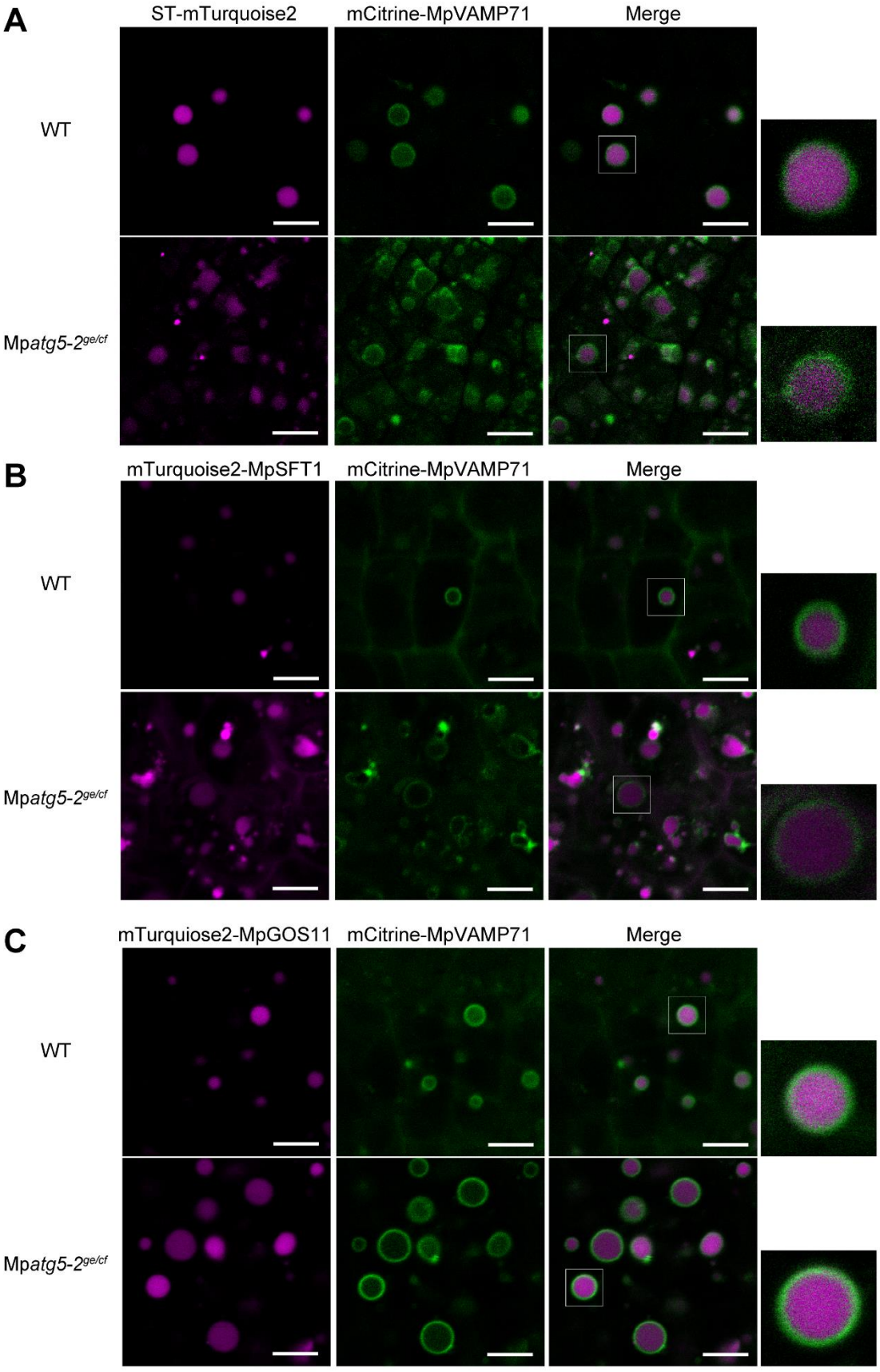
A
ST-mTurquoise2
mCitrine-MpVAMP71
Merge
WT
Mpatg5-2ge/cf
B
mTurquoise2-MpSFT1
mCitrine-MpVAMP71
Merge
WT
Mpatg5-2ge/cf
C
mTurquiose2-MpGOS11
mCitrine-MpVAMP71
Merge
WT
Mpatg5-2ge/cf

Figure 45. Subcellular localization of the Golgi marker in antheridial cells

Subcellular localization of ST-mTurquoise2 (**A**), mTurquoise2-MpSFT1 (**B**), or mTurquoise2-MpGOS1 (**C**) in hand-sectioned antheridia of the wild type (WT) and Mp*atg5-2*$^{ge/cf}$. The magenta and green colors indicate the fluorescence from mTurquoise2 and mCitrine, respectively. The right panels are magnified images of the boxed regions. Bars = 5 μm.

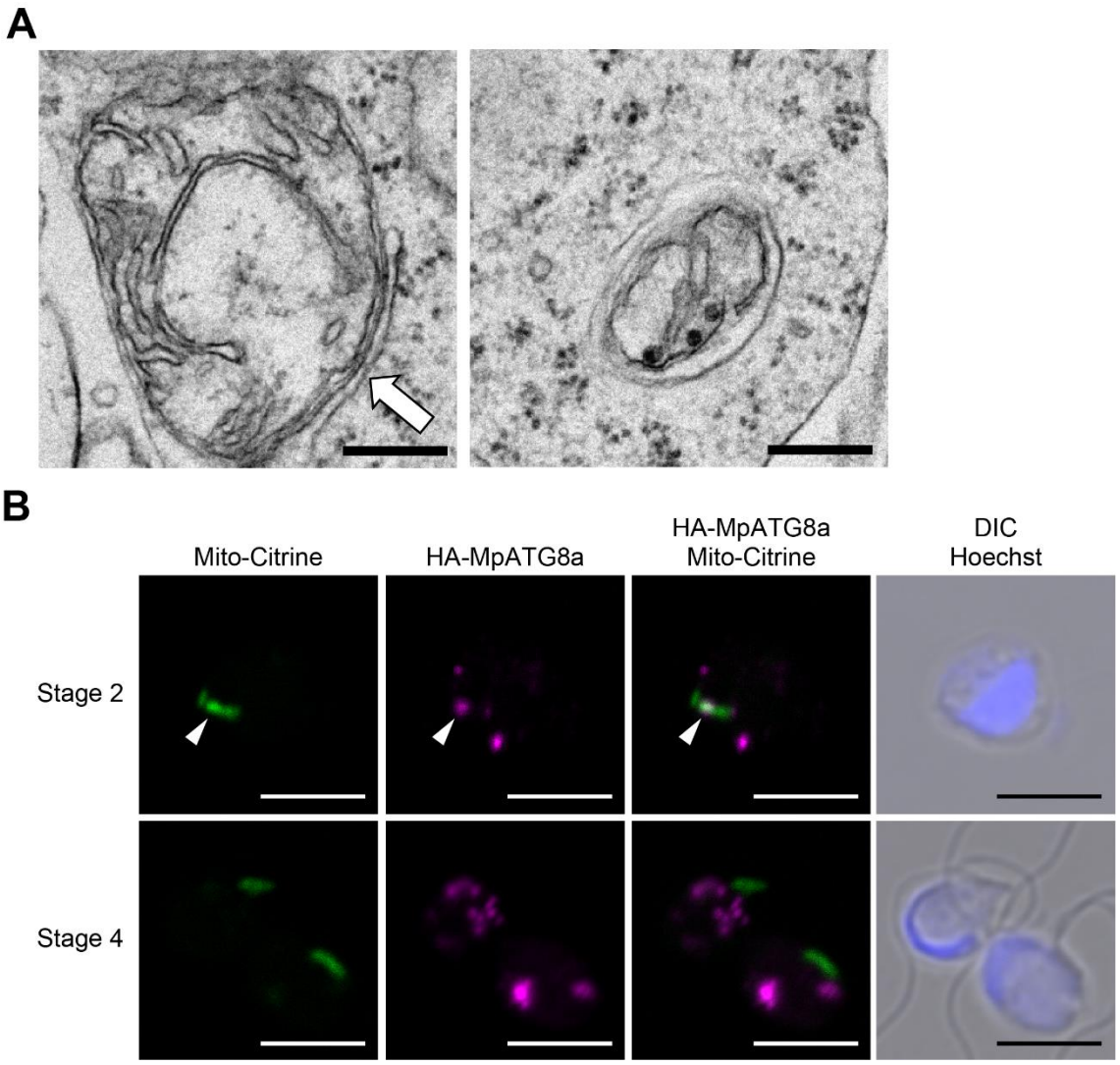

Figure 46. Distinct degradation mechanisms of mitochondria from other organelles during spermiogenesis

(**A**) TEM observation of mitochondria in wild-type spermatids. The arrow indicates the isolation membrane. (**B**) Subcellular localization of HA-MpATG8a in cell wall-digested antheridium cells. The green, magenta, and blue colors indicate the fluorescence from Citrine, Alexa Fluor 546, and Hoechst, respectively. Arrowheads indicate HA-MpATG8a on mitochondria. Bars = 5 μm.

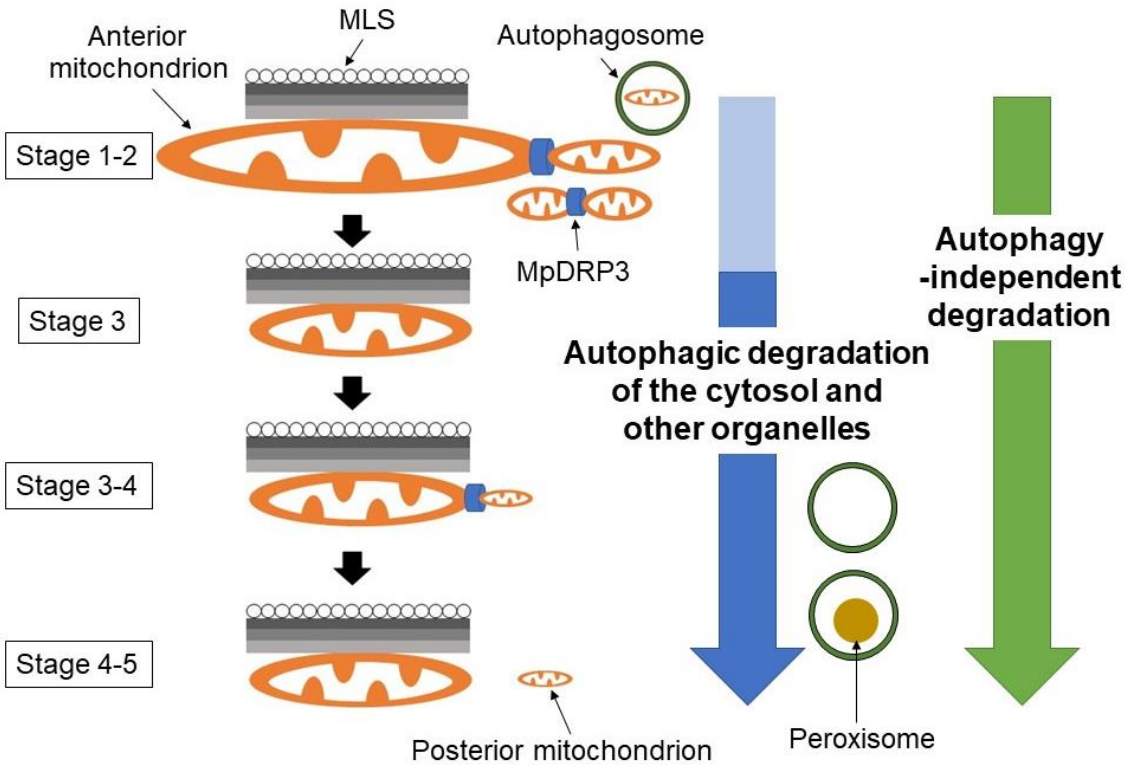

Figure 47. Schemes of cytoplasm removal during spermiogenesis in *M. polymorpha*

The schematic model of organelle reorganization during spermiogenesis in *M. polymorpha*. At Stage 1 to 2, mitochondria undergo frequent fission mediated by MpDRP3, and fragmented mitochondria are degraded by autophagy. At Stage 3, only one anterior mitochondrion is remained in the spermatid. At Stage 3 to 4, the anterior mitochondrion divides to form the posterior mitochondrion. Whereas degradation of mitochondria occurs during Stage 1 to 2, most of other cytoplasmic components such as peroxisomes are degraded by autophagy after Stage 3. Autophagy-independent degradation including endocytic degradation also occurs during spermiogenesis.

GENERAL DISCUSSION

The process in sexual reproduction has been diversified during evolution of eukaryotes. In the lineage of Viridiplantae, sperms are independently evolved from the metazoan lineage, and morphology and organelle composition of spermatozoids are distinct from those in metazoan spermatozoa (Renzaglia and Garbary 2001; Mori et al. 2015). However, it remains largely unknown how the unique charateristics of plant spermatozoids are developed. My detailed observation and molecular analyses demonstrated that each of organelles and organelle proteins is degraded in the vacuole in a distinctive manner. This degradation system is different from the cytoplasm removal during metazoan spermiogenesis, which is consistent with independent evolution of male reproductive processes between plants and animals. However, it remains unknown whether other plant species also employ a similar degradation system to *M. polymorpha*, which should be examined in future studies. Chara, Nitella, other byrophytes, and some lycophytes harbor spermatozoids similar to that in *M. polymorpha* in their shapes (Renzaglia and Garbary 2001), which could reflect a similar degradation system occuring in these species. However, Chara and Nitella spermatozoids harbor more mitochondria and plastids at the anterior and posterior regions of spermatozoids than bryophyte spermatozoids (Turner 1968; Duncan et al. 1997), suggesting that the mechanisms for selecting degraded organelles could be distinct in these species from that in *M. polymorpha* at least partly. Intriguingly, in the monilophyte *Marsilea vestita*, a sizable cytoplasmic remnant of the spermatozoid, which includes small mitochondria and amyloplasts, is shed while spermatozoids swim and/or when spermatozoids enter the megaspore (Myles and Bell 1975; Myles and Hepler 1977). Thus, the cytoplasm removal system during spermiogenesis could be diversified during evolution of streptophytes.

In this study, I observed organelle dynamics during spermiogenesis in *M. polymorpha*. However, the relationship between the unique organelle composition and the function of spermatozoids still remains unclear. Morphology of mitochondria is diverged among eukaryotic lineages: one at the anterior and the other at the posterior of the cell body in bryophyte spermatozoids, a helical sheath at the middle piece of spermatozoa in mammals, and two elongated mitochondria along the axoneme in *D. melanogaster* (Tokuyasu et al. 1972; Renzaglia and Garbary 2001; Ho and Wey 2007). Although Noguchi et al. (2011) reported a unique role of mitochondria reorganization in elongation of spermatids in *D. melanogaster*, the biological significance of mitochondrial morphology in sperm remains largely unknown. In this study, I succeeded in generating spermatozoids lacking the posterior mitochondrion by expressing a dominant negative form of MpDRP3. Further characterization of the function of these spermatozoids will reveal physiological roles of two mitochondria in bryophytes. Furthermore, comparative analyses of mitochondrial functions between *M. polymorpha* and other eukaryotic organisms including metazoa and other land plants would lead us to understand what physiological functions the diverged morphologies of mitochondria in sperm reflect.

Although morphological aspects of spermiogenesis have been studied since the first discovery of motile male gametes in land plants (Renzaglia and Garbary 2001), molecular mechanisms of spermatozoid formation are largely unknown due to the lack of molecular cell biological tools usable in basal land plants. *M. polymorpha* would be a suitable system for analyses of development and functions of spermatozoids because molecular genetic tools including organelle markers are established (this study; Ishizaki et al. 2016). Furthermore, understanding mechanisms of dynamic and complex reorganization of organelles during spermiogenesis would provide invaluable information to understand

organelle dynamics in other developmental processes. I believe that this study will be an important step of the study of mechanisms and biological significance of organelle reorganization during plant development.

REFERENCES

Arimura, S.I. (2018) Fission and fusion of plant mitochondria, and genome maintenance. *Plant Physiol.* 176: 152-161.

Arimura, S.I. and Tsutsumi, N. (2002) A dynamin-like protein (ADL2b), rather than FtsZ, is involved in *Arabidopsis* mitochondrial division. *Proc. Natl. Acad. Sci. USA* 99: 5727-5731.

Baba, M., Takeshige, K., Baba, N. and Ohsumi, Y. (1994) Ultrastructural analysis of the autophagic process in yeast: detection of autophagosomes and their characterization. *J. Cell Biol.* 124: 903-913.

Bowman, J.L., Araki, T., Arteaga-Vazquez, M.A., Berger, F., Dolan, L., Haseloff, J., et al. (2016) The naming of names: guidelines for gene nomenclature in Marchantia. *Plant Cell Physiol*. 57: 257-261.

Brauns, A.K., Heine, M., Tödter, K., Baumgart-Vogt, E., Lüers, G.H. and Schumacher, U. (2019) A defect in the peroxisomal biogenesis in germ cells induces a spermatogenic arrest at the round spermatid stage in mice. *Sci. Rep.* 9: 9553.

Brownfield, L., Yi, J., Jiang, H., Minina, E.A., Twell, D. and Köhler, C. (2015) Organelles maintain spindle position in plant meiosis. *Nat. Commun.* 6: 6492.

Chapman, J., Ng, Y.S. and Nicholls, T.J. (2020) The maintenance of mitochondrial DNA integrity and dynamics by mitochondrial membranes. *Life* 10: 164.

Caspar, T., Huber, S.C. and Somerville, C. (1985) Alterations in growth, photosynthesis, and respiration in a starchless mutant of *Arabidopsis thaliana* (L.) deficient in chloroplast phosphoglucomutase activity. *Plant Physiol.* 79: 11-17.

Chung, T., Phillips, A.R. and Vierstra, R.D. (2010) ATG8 lipidation and ATG8-mediated autophagy in Arabidopsis require ATG12 expressed from the differentially controlled

ATG12A AND *ATG12B* loci. *Plant J.* 62: 483-493.

D'Ippolito, R.A., Minamino, N., Rivera-Casas, C., Cheema, M.S., Bai, D.L., Kasinsky, H.E., et al. (2019) Protamines from liverwort are produced by post-translational cleavage and C-terminal di-aminopropanelation of several male germ-specific H1 histones. *J. Biol. Chem.* 294: 16364-16373.

Dacks, J.B. and Field, M.C. (2007) Evolution of the eukaryotic membrane-trafficking system: origin, tempo and mode. *J. Cell Sci.* 120: 2977-2985.

Dickman, M., Williams, B., Li, Y., de Figueiredo, P. and Wolpert, T. (2017) Reassessing apoptosis in plants. *Nat. Plants* 3: 773-779.

Dietert, S.E. (1966) Fine structure of the formation and fate of the residual bodies of mouse spermatozoa with evidence for the participation of lysosomes. *J. Morphol.* 120: 317-346.

Dobzinski, N., Chuartzman, S.G., Kama, R., Schuldiner, M. and Gerst, J.E. (2015) Starvation-dependent regulation of Golgi quality control links the TOR signaling and vacuolar protein sorting pathways. *Cell Rep.* 12: 1876-1886.

Doelling, J.H., Walker, J.M., Friedman, E.M., Thompson, A.R. and Vierstra, R.D. (2002) The APG8/12-activating enzyme APG7 is required for proper nutrient recycling and senescence in *Arabidopsis thaliana*. *J. Biol. Chem.* 277: 33105-33114.

Duncan, T.M., Renzaglia, K.S. and Garbary, D.J. (1997) Ultrastrueture and phylogeny of the spermatozoid of *Chara vulgaris* (*Charophyceae*). *Pl. Syst. Evol.* 204: 125-140.

Fabian, L. and Brill, J.A. (2012) Drosophila spermiogenesis: Big things come from little packages. *Spermatogenesis* 2: 197-212.

Figueroa, C., Kawada, M.E., Véliz, L.P., Hidalgo, U., Barros, C., González, S., et al. (2000) Peroxisomal proteins in rat gametes. *Cell Biochem. Biophys.* 32: 259-268.

Fujimoto, M., Arimura, S.I., Mano, S., Kondo, M., Saito, C., Ueda, T., et al. (2009) Arabidopsis dynamin-related proteins DRP3A and DRP3B are functionally redundant in mitochondrial fission, but have distinct roles in peroxisomal fission. *Plant J.* 58: 388-400.

Gatica, D., Lahiri, V. and Klionsky, D.J. (2018) Cargo recognition and degradation by selective autophagy. *Nat. Cell Biol.* 20: 233-242.

Giacomello, M., Pyakurel, A., Glytsou, C. and Scorrano, L. (2020) The cell biology of mitochondrial membrane dynamics. *Nat. Rev. Mol. Cell Biol.* 21: 204-224.

Gomez, E., Buckingham, D.W., Lanzafame, F., Irvine, D.S. and Aitken, R.J. (1996) Development of an image analysis system to monitor the retention of residual cytoplasm by human spermatozoa: correlation with biochemical markers of the cytoplasmic space, oxidative stress, and sperm function. *J. Androl.* 17: 276-287.

Goswami, R., Asnacios, A., Hamant, O. and Chabouté, M.E. (2020) Is the plant nucleus a mechanical rheostat? *Curr. Opin. Plant Biol.* 57: 155-163.

Hanada, T., Noda, N.N., Satomi, Y., Ichimura, Y., Fujioka, Y., Takao, T., et al. (2007) The Atg12-Atg5 conjugate has a novel E3-like activity for protein lipidation in autophagy. *J. Biol. Chem.* 282: 37298-37302.

Hanaoka, H., Noda, T., Sirano, Y., Kato, T., Hayashi, H., Shibata, D., et al. (2002) Leaf senescence and starvation-induced chlorosis are accelerated by the disruption of an Arabidopsis autophagy gene. *Plant Physiol.* 129: 1181-1193.

Hara-Nishimura, I. and Hatsugai, N. (2011) The role of vacuole in plant cell death. *Cell Death Differ.* 18: 1298-1304.

Higo, A., Kawashima, T., Borg, M., Zhao, M., Lopez-Vidriero, I., Sakayama, H., et al. (2018) Transcription factor DUO1 generated by neo-functionalization is associated

with evolution of sperm differentiation in plants. *Nat. Commun.* 9: 5283.

Higo, A., Niwa, M., Yamato, K.T., Yamada, L., Sawada, H., Sakamoto, T., et al. (2016) Transcriptional framework of male gametogenesis in the liverwort *Marchantia polymorpha* L. *Plant Cell Physiol.* 57: 325-338.

Hisanaga, T., Okahashi, K., Yamaoka, S., Kajiwara, T., Nishihama, R., Shimamura, M., et al. (2019a) A *cis*-acting bidirectional transcription switch controls sexual dimorphism in the liverwort. *EMBO J.* 38: e100240.

Hisanaga, T., Yamaoka, S., Kawashima, T., Higo, A., Nakajima, K., Araki, T., et al. (2019b) Building new insights in plant gametogenesis from an evolutionary perspective. *Nat. Plants* 5: 663-669.

Ho, H.C. and Wey, S. (2007) Three dimensional rendering of the mitochondrial sheath morphogenesis during mouse spermiogenesis. *Microsc. Res. Tech.* 70: 719-723.

Hosokawa, N., Sasaki, T., Iemura, S.I., Natsume, T., Hara, T. and Mizushima, N. (2009) Atg101, a novel mammalian autophagy protein interacting with Atg13. *Autophagy* 5: 973-979.

Huang, Q., Liu, Y., Zhang, S., Yap, Y.T., Li, W., Zhang, D., et al. (2020) Autophagy core protein ATG5 is required for elongating spermatid development, sperm individualization and normal fertility in male mice. *Autophagy* 1-15.

Huang, J., Wang, H., Chen, Y., Wang, X. and Zhang, H. (2012) Residual body removal during spermatogenesis in *C. elegans* requires genes that mediate cell corpse clearance. *Development* 139: 4613-4622.

Huang, R., Xu, Y., Wan, W., Shou, X., Qian, J., You, Z., et al. (2015) Deacetylation of nuclear LC3 drives autophagy initiation under starvation. *Mol. Cell* 57: 456-466.

Huang, X., Zheng, C., Liu, F., Yang, C., Zheng, P., Lu, X., et al. (2019) Genetic analyses

of the Arabidopsis ATG1 kinase complex reveal both kinase-dependent and independent autophagic routes during fixed-carbon starvation. *Plant Cell* 31: 2973-2995.

Ingerman, E., Perkins, E.M., Marino, M., Mears, J.A., McCaffery, J.M., Hinshaw, J.E., et al. (2005) Dnm1 forms spirals that are structurally tailored to fit mitochondria. *J. Cell Biol.* 170: 1021-1027.

Inoue, Y., Suzuki, T., Hattori, M., Yoshimoto, K., Ohsumi, Y. and Moriyasu, Y. (2006) *AtATG* genes, homologs of yeast autophagy genes, are involved in constitutive autophagy in *Arabidopsis* root tip cells. *Plant Cell Physiol.* 47:1641-1652.

Inouye, I. and Hori, T. (1991) High-speed video analysis of the flagellar beat and swimming patterns of algae: possible evolutionary trends in green algae. *Protoplasma* 164: 54-69.

Ishizaki, K., Chiyoda, S., Yamato, K.T. and Kohchi, T. (2008) Agrobacterium-mediated transformation of the haploid liverwort *Marchantia polymorpha* L., an emerging model for plant biology. *Plant Cell Physiol.* 49: 1084-1091.

Ishizaki, K. Nishihama, R., Ueda, M., Inoue, K., Ishida, S., Nishimura, Y., et al. (2015) Development of gateway binary vector series with four different selection markers for the liverwort *Marchantia polymorpha*. *PLoS One* 10: e0138876.

Ishizaki, K., Nishihama, R., Yamato, K.T. and Kohchi, T. (2016) Molecular genetic tools and techniques for *Marchantia polymorpha* research. *Plant Cell Physiol.* 57: 262-270.

Izumi, M., Hidema, J., Wada, S., Kondo, E., Kurusu, T., Kuchitsu, K., et al. (2015) Establishment of monitoring methods for autophagy in rice reveals autophagic recycling of chloroplasts and root plastids during energy limitation. *Plant Physiol.* 167: 1307-1320.

Izumi, M., Nakamura, S. and Li, N. (2019) Autophagic turnover of chloroplasts: its roles and regulatory mechanisms in response to sugar starvation. *Front. Plant Sci.* 10: 280.

Izumi, Y. and Ono, K. (1999) Changes in plastid DNA content during the life cycle of the hornwort *Anthoceros punctatus* L. *Cytologia* 64: 37-44.

Johansen, T. and Lamark, T. (2020) Selective autophagy: ATG8 family proteins, LIR motifs and cargo receptors. *J. Mol. Biol.* 432: 80-103.

Kabeya, Y., Mizushima, N., Ueno, T., Yamamoto, A., Kirisako, T., Noda, T., et al. (2000) LC3, a mammalian homologue of yeast Apg8p, is localized in autophagosome membranes after processing. *EMBO J.* 19: 5720-5728.

Kanazawa, T., Era, A., Minamino, N., Shikano, Y., Fujimoto, M., Uemura, T., et al. (2016) SNARE molecules in *Marchantia polymorpha*: unique and conserved features of the membrane fusion machinery. *Plant Cell Physiol*. 57: 307-324.

Kanazawa, T., Morinaka, H., Ebine, K., Shimada, T.L., Ishida, S., Minamino, N., et al. (2020) The liverwort oil body is formed by redirection of the secretory pathway. *Nat. Commun.* 11: 6152.

Kang, S., Shin, K.D., Kim, J.H. and Chung, T. (2018) Autophagy-related (ATG) 11, ATG9 and the phosphatidylinositol 3-kinase control ATG2-mediated formation of autophagosomes in Arabidopsis. *Plant Cell Rep.* 37: 653-664.

Kanki, T., Wang, K., Cao, Y., Baba, M. and Klionsky, D.J. (2009) Atg32 is a mitochondrial protein that confers selectivity during mitophagy. *Dev. Cell* 17: 98-109.

Keating, J., Grundy, C.E., Elliott, M. and Robinson, J. (1997) Investigation of the association between the presence of cytoplasmic residues on the human sperm midpiece and defective sperm function. *J. Reprod. Fertil.* 110: 71-77.

Kim, J., Kamada, Y., Stromhaug, P.E., Guan, J., Hefner-Gravink, A., Baba, M., et al.

(2001) Cvt9/Gsa9 functions in sequestering selective cytosolic cargo destined for the vacuole. *J. Cell Biol.* 153: 381-396.

Kimata, Y., Higaki, T., Kurihara, D., Ando, N., Matsumoto, H., Higashiyama, T., et al. (2020) Mitochondrial dynamics and segregation during the asymmetric division of *Arabidopsis* zygotes. *Quant. Plant Biol.* 1: e3.

Kimata, Y., Kato, T., Higaki, T., Kurihara, D., Yamada, T., Segami, S., et al. (2019) Polar vacuolar distribution is essential for accurate asymmetric division of *Arabidopsis* zygotes. *Proc. Natl. Acad. Sci. USA* 116: 2338-2343.

Kirisako, T., Baba, M., Ishihara, N., Miyazawa, K., Ohsumi, M., Yoshimori, T., et al. (1999) Formation process of autophagosome is traced with Apg8/Aut7p in yeast. *J. Cell Biol.* 147: 435-446.

Klionsky, D.J., Cregg, J.M., Dunn, W.A., Jr., Emr, S.D., Sakai, Y., Sandoval, I.V., et al. (2003) A unified nomenclature for yeast autophagy-related genes. *Dev. Cell* 5: 539-545.

Koi, S., Hisanaga, T., Sato, K., Shimamura, M., Yamato, K.T., Ishizaki, K., et al. (2016) An evolutionarily conserved plant RKD factor controls germ cell differentiation. *Curr. Biol.* 26: 1775-1781.

Kreitner, G.L. (1977a) Influence of the multilayered structure on the morphogenesis of Marchantia spermatids. *Amer. J. Bot.* 64: 57-64.

Kreitner, G.L. (1977b) Transformation of the nucelus in Marchantia spermatids: morphogenesis. *Amer. J. Bot.* 64: 464-475.

Kubota, A., Ishizaki, K., Hosaka, M. and Kohchi, T. (2013) Efficient Agrobacterium-mediated transformation of the liverwort *Marchantia polymorpha* using regenerating thalli. *Biosci. Biotechnol. Biochem.* 77: 167-172.

Kuma, A., Hatano, M., Matsui, M., Yamamoto, A., Nakaya, H., Yoshimori, T., et al. (2004) The role of autophagy during the early neonatal starvation period. *Nature* 432: 1032-1036.

L'Hernault, S.W. (2006) Spermatogenesis. *WormBook* 1-14.

Letunic, I., Doerks, T. and Bork, P. (2015) SMART: recent updates, new developments and status in 2015. *Nucelic Acids Res.* 43: 257-260.

Letunic, I. and Bork, P. (2018) 20 years of the SMART protein domain annotation resource. *Nucelic Acids Res.* 46: 493-496.

Li, F., Chung, T. and Vierstra, R.D. (2014) AUTOPHAGY-RELATED11 plays a critical role in general autophagy- and senescence-induced mitophagy in *Arabidopsis*. *Plant Cell* 26: 788-807.

Liu, Y., Cui, H., Zhang, Q. and Sodmergen (2004) Divergent potentials for cytoplasmic inheritance within the genus Syringa. A new trait associated with speciogenesis. *Plant Physiol.* 136: 2762-2770.

Liu, F., Hu, W., Li, F., Marshall, R.S., Zarza, X., Munnik, T., et al. (2020) AUTOPHAGY-RELATED14 and Its Associated Phosphatidylinositol 3-Kinase Complex Promote Autophagy in Arabidopsis. *Plant Cell* 32: 3939-3960.

Liu, F., Hu, W. and Vierstra, R.D. (2018) The vacuolar protein sorting-38 subunit of the *Arabidopsis* phosphatidylinositol-3-kinase complex plays critical roles in autophagy, endosome sorting, and gravitropism. *Front. Plant Sci.* 9: 781.

Mano, S., Hayashi, M. and Nishimura, M. (1999) Light regulates alternative splicing of hydroxypyruvate reductase in pumpkin. *Plant J.* 17: 309-320.

Mano, S., Nishihama, R., Ishida, S., Hikino, K., Kondo, M., Nishimura, M., et al. (2018) Novel gateway binary vectors for rapid tripartite DNA assembly and promoter

analysis with various reporters and tags in the liverwort *Marchantia polymorpha*. *PLoS One* 13: e0204964.

Mao, K., Wang, K., Liu, X. and Klionsky, D.J. (2013) The scaffold protein Atg11 recruits fission machinery to drive selective mitochondria degradation by autophagy. *Dev. Cell* 26: 9-18.

Marshall, R.S. and Vierstra, R.D. (2018) Autophagy: the master of bulk and selective recycling. *Annu. Rev. Plant Biol.* 69: 173-208.

Masclaux-Daubresse, C., Chen,Q. and Havé, M. (2017) Regulation of nutrient recycling via autophagy. *Curr. Opin. Plant Biol.* 39: 8-17.

Matsushima, R., Tang, L.Y., Zhang, L., Yamada, H., Twell, D. Sakamoto, W. (2011) A conserved, Mg^{2+}-dependent exonuclease degrades organelle DNA during *Arabidopsis* pollen development. *Plant Cell* 23: 1608-1624.

Meier, I., Griffis, A.H., Groves, N.R. and Wagner, A. (2016) Regulation of nuclear shape and size in plants. *Curr. Opin. Cell Biol.* 40: 114-123.

Minamino, N., Kanazawa, T., Nishihama, R, Yamato, K.T., Ishizaki, K., Kohchi, T., et al. (2017) Dynamic reorganization of the endomembrane system during spermatogenesis in *Marchantia polymorpha*. *J. Plant Res.* 130: 433-441.

Miyamura, S., Matsunaga, S. and Hori, T. (2002) High-speed video microscopical analysis of the flagellar movement of *Marchantia polymorpha* sperm. *Bryol. Res.* 8: 79-83. (in Japanese)

Mizushima, N. and Komatsu, M. (2011) Autophagy: renovation of cells and tissues. *Cell* 147: 728-741.

Mizushima, N., Yamamoto, A., Hatano, M., Kobayashi, Y., Kabeya, Y., Suzuki, K., et al. (2001) Dissection of autophagosome formation using Apg5-deficient mouse

embryonic stem cells. *J. Cell Biol.* 152: 657-668.

Mizushima, N., Yoshimori, T. and Ohsumi, Y. (2011) The role of Atg proteins in autophagosome formation. *Annu. Rev. Cell Dev. Biol.* 27: 107-132.

Mochida, K., Oikawa, Y., Kimura, Y., Kirisako, H., Hirano, H., Ohsumi, Y., et al. (2015) Receptor-mediated selective autophagy degrades the endoplasmic reticulum and the nucleus. *Nature* 522: 359-362.

Montgomery, S.A., Tanizawa, Y., Galik, B., Wang, N., Ito, T., Mochizuki, T., et al. (2020) Chromatin organization in early land plants reveals an ancestral association between H3K27me3, transposons, and constitutive heterochromatin. *Curr. Biol.* 30: 573-588.

Mori, T., Kawai-Toyooka, H., Igawa, T. and Nozaki, H. (2015) Gamete dialogs in green lineages. *Mol. Plant* 8: 1442-1454.

Myles, D.G. and Bell, P.R. (1975) An ultrastructural study of the spermatozoid of the fern, *Marsilea vestita*. *J. Cell Sci.* 17: 633-645.

Myles, D.G. and Hepler, P.K. (1977) Spermiogenesisin the fern *Marsilea*: microtubules, nuclear shaping, and cytomorphogenesis. *J. Cell Sci.* 23: 57-83.

Nagaoka, N., Yamashita, A., Kurisu, R., Watari, Y., Ishizuna, F., Tsutsumi, N., et al. (2017) DRP3 and ELM1 are required for mitochondrial fission in the liverwort *Marchantia polymorpha*. *Sci. Rep.* 7: 4600.

Nakatogawa, H. (2020) Mechanisms governing autophagosome biogenesis. *Nat. Rev. Mol. Cell Biol.* 21: 439-458.

Naylor, K., Ingerman, E., Okreglak, V., Marino, M., Hinshaw, J.E. and Nunnari, J. (2006) Mdv1 interacts with assembled dnm1 to promote mitochondrial division. *J. Biol. Chem.* 281: 2177-2183.

Nishida, Y., Arakawa, S., Fujitani, K., Yamaguchi, H., Mizuta, T., Kanaseki, T., et al.

(2009) Discovery of Atg5/Atg7-independent alternative macroautophagy. *Nature* 461: 654-658.

Nishimura, Y., Misumi, O., Matsunaga, S., Higashiyama, T., Yokota, A. and Kuroiwa, T. (1999) The active digestion of uniparental chloroplast DNA in a single zygote of *Chlamydomonas reinhardtii* is revealed by using the optical tweezer. *Proc. Natl. Acad. Sci. USA* 96: 12577-12582.

Noguchi, T., Koizumi, M. and Hayashi, S. (2011) Sustained elongation of sperm tail promoted by local remodeling of giant mitochondria in *Drosophila*. *Curr. Biol.* 21: 805-814.

Norizuki, T., Minamino, N. and Ueda, T. (2020) Role of autophagy in male reproductive processes in land plants. *Front. Plant Sci.* 11: 756.

O'Donnell, L., Nicholls, P.K., O'Bryan, M.K., McLachlan, R.I. and Stanton, P.G. (2011) Spermiation: The process of sperm release. *Spermatogenesis* 1: 14-35.

Otsuga, D., Keegan, B.R., Brisch, E., Thatcher, J.W., Hermann, G.J., Bleazard, W., et al. (1998) The dynamin-related GTPase, Dnm1p, controls mitochondrial morphology in yeast. *J. Cell Biol.* 143: 333-349.

Paez Valencia, J., Goodman, K. and Otegui, M.S. (2016) Endocytosis and Endosomal Trafficking in Plants. *Annu. Rev. Plant Biol.* 67: 309-335.

Papandreou, M.E. and Tavernarakis, N. (2019) Nucleophagy: from homeostasis to disease. *Cell Death Differ.* 26: 630-639.

Periappuram, C., Steinhauer, L., Barton, D.L., Taylor, D.C., Chatson, B. and Zou, J. (2000) The plastidic phosphoglucomutase from Arabidopsis. A reversible enzyme reaction with an important role in metabolic control. *Plant Physiol.* 122: 1193-1199.

Pitnick, S., Hosken, D.J. and Birkhead, T.R. (2009) Sperm morphological diversity. In

Sperm Biology: An Evolutionary Perspective. Edited by Birkhead, T.R., Hosken, D.J. and Pitnick, S. pp. 69–149. Academic Press, USA.

Porra, R.J., Thompson, W.A. and Kriedemann, P.E. (1989) Determination of accurate extinction coefficients and simultaneous equations for assaying chlorophylls *a* and *b* extracted with four different solvents: verification of the concentration of chlorophyll standards by atomic absorption spectroscopy. *Biochim. Biophys. Acta* 975: 384–394.

Rambold, A.S., Kostelecky, B., Elia, N. and Lippincott-Schwartz, J. (2011) Tubular network formation protects mitochondria from autophagosomal degradation during nutrient starvation. *Proc. Natl. Acad. Sci. USA* 108: 10190-10195.

Rengan, A.K., Agarwal, A., van der Linde, M. and du Plessis, S.S. (2012) An investigation of excess residual cytoplasm in human spermatozoa and its distinction from the cytoplasmic droplet. *Reprod. Biol. Endocrinol.* 10: 92.

Renzaglia, K.S. and Duckett, J.G. (1987) Spermatogenesis in *Blasia pusilla*: from young antheridium through mature spermatozoid. *Bryologist* 90: 419-449.

Renzagila, K.S. and Garbary, D.J. (2001) Motile gametes of land plants: diversity, development, and evolution. *Crit. Rev. Plant Sci.* 20: 107-213.

Sanchez-Vera, V., Kenchappa, C.S., Landberg, K., Bressendorff, S., Schwarzbach, S., Martin, T., et al. (2017) Autophagy is required for gamete differentiation in the moss *Physcomitrella patens*. *Autophagy* 13: 1939-1951.

Sasaki, T., Sato, Y., Higashiyama, T. and Sasaki, N. (2017) Live imaging reveals the dynamics and regulation of mitochondrial nucleoids during the cell cycle in Fucci2-HeLa cells. *Sci. Rep.* 7: 11257.

Sengupta, D. and Linstedt, A.D. (2011) Control of organelle size: the Golgi complex. *Annu. Rev. Cell Dev. Biol.* 27: 57-77.

Shang, Y., Wang, H., Jia, P., Zhao, H., Liu, C., Liu, W., et al. (2016) Autophagy regulates spermatid differentiation via degradation of PDLIM1. *Autophagy* 12: 1575-1592.

Shemi, A., Ben-Dor, S. and Vardi, A. (2015) Elucidating the composition and conservation of the autophagy pathway in photosynthetic eukaryotes. *Autophagy* 11: 701-715.

Shimamura, M. (2015) Whole-mount immunofluorescence staining of plant cells and tissues. In Plant Microtechniques and Protocols Edited by Yeung, E. pp. 181–196 Springer, Switzerland.

Shimamura, M. (2016) *Marchantia polymorpha*: taxonomy, phylogeny and morphology of a model system. *Plant Cell Physiol.* 57: 230-256.

Shimamura, M., Fukushima, H., Yamaguchi, T. and Deguchi, H. (1999) Behavior of plastid and plastid DNA during spermiogenesis in *Dumortiera hirsute*. *Bryol. Res.* 7: 201-204.

Shintani, T. and Klionsky, D.J. (2004) Cargo proteins facilitate the formation of transport vesicles in the cytoplasm to vacuole targeting pathway. *J. Biol. Chem.* 279: 29889-29894.

Smith, B.V. and Lacy, D. (1959) Residual bodies of seminiferous tubules of the rat. *Nature* 184: 249-251.

Stephani, M. and Dagdas, Y. (2020) Plant selective autophagy-still an uncharted territory with a lot of hidden gems. *J. Mol. Biol.* 432: 63-79.

Sugano, S.S., Nishihama, R., Shirakawa, M., Takagi, J., Matsuda, Y., Ishida, S., et al. (2018) Efficient CRISPR/Cas9-based genome editing and its application to conditional genetic analysis in *Marchantia polymorpha*. *PLoS One* 13: e0205117.

Sugano, S.S., Shirakawa, M., Takagi, J., Matsuda, Y., Shimada, T., Hara-Nishimura, I., et

al. (2014) CRISPR/Cas9-mediated targeted mutagenesis in the liverwort *Marchantia polymorpha* L. *Plant Cell Physiol.* 55: 475-481.

Suttangkakul, A., Li, F., Chung, T. and Vierstra, R.D. (2011) The ATG1/ATG13 protein kinase complex is both a regulator and a target of autophagic recycling in *Arabidopsis*. *Plant Cell* 23: 3761-3779.

Takeshige, K., Baba, M., Tsuboi, S., Noda, T. and Ohsumi, Y. (1992) Autophagy in yeast demonstrated with proteinase-deficient mutants and conditions for its induction. *J. Cell Biol.* 119: 301-311.

Thompson, A. R., Doelling, J.H., Suttangkakul, A. and Vierstra, R.D. (2005) Autophagic nutrient recycling in Arabidopsis directed by the ATG8 and ATG12 conjugation pathways. *Plant Physiol.* 138: 2097-2110.

Thumm, M., Egner, R., Koch, B., Schlumpberger, M., Straub, M., Veenhuis, M., et al. (1994) Isolation of autophagocytosis mutants of *Saccharomyces cerevisiae*. *FEBS Lett.* 349: 275-280.

Tokuyasu, K.T., Peacock, W.J. and Hardy, R.W. (1972) Dynamics of spermiogenesis in *Drosophila melanogaster*. I. Individualization process. *Z. Zellforsch. Mikrosk. Anat.* 124: 479-506.

Tsukada, M. and Ohsumi, Y. (1993) Isolation and characterization of autophagy-defective mutants of *Saccharomyces cerevisiae*. *FEBS Lett.* 333: 169-174.

Turner, F.R. (1968) An ultrastructural study of plant spermiogenesis. Spermatogenesis in *Nitella*. *J. Cell Biol.* 37: 370-393.

Twig, G, Elorza, A, Molina, A.J., Mohamed, H., Wikstrom, J.D., Walzer, G., et al. (2008) Fission and selective fusion govern mitochondrial segregation and elimination by autophagy. *EMBO J.* 27: 433-446.

van Doorn, W.G., Beers, E.P., Dangl, J.L., Franklin-Tong, V.E., Gallois, P., Hara-Nishimura, I., et al. (2011) Morphological classification of plant cell deaths. *Cell Death Differ.* 18: 1241-1246.

Wang, F., Liu, P., Zhang, Q., Zhu, J., Chen, T., Arimura, S.I., et al. (2012) Phosphorylation and ubiquitination of dynamin-related proteins (AtDRP3A/3B) synergically regulate mitochondrial proliferation during mitosis. *Plant J.* 72: 43-56.

Wang, H., Wan, H., Li, X., Liu, W., Chen, Q., Wang, Y., et al. (2014) Atg7 is required for acrosome biogenesis during spermatogenesis in mice. *Cell Res.* 24: 852-869.

Yamaguchi, H., Arakawa, S., Kanaseki, T., Miyatsuka, T., Fujitani, Y., Watada, H., et al. (2016) Golgi membrane-associated degradation pathway in yeast and mammals. *EMBO J.* 35: 1991-2007.

Yamashita, S.I., Jin, X., Furukawa, K., Hamasaki, M., Nezu, A., Otera, H., et al. (2016) Mitochondrial division occurs concurrently with autophagosome formation but independently of Drp1 during mitophagy. *J. Cell Biol.* 215: 649-665.

Yoshimoto, K., Hanaoka, H., Sato, S., Kato, T., Tabata, S., Noda, T., et al. (2004) Processing of ATG8s, ubiquitin-like proteins, and their deconjugation by ATG4s are essential for plant autophagy. *Plant Cell* 16: 2967-2983.

Zhao, Y.G. and Zhang, H. (2019) Autophagosome maturation: An epic journey from the ER to lysosomes. *J. Cell Biol.* 218: 757-770.